Development of some Cu based p-type transparent conducting oxides through novel doping strategy and investigation of its electrical and optical properties

Thesis submitted to

JADAVPUR UNIVERSITY

For the degree of

Doctor of Philosophy (Science)

By

Prasanta Mandal

School of Materials Science and Nanotechnology

Faculty of Interdisciplinary Studies, Law & Management

Jadavpur University

Kolkata-700032

India

2023

Dedicated to my parents

Dedicated to my dearest wife

Certificate

This is to certified in this thesis entitled ***"Development of some Cu based p-type transparent conducting oxides through novel doping strategy and investigation of its electrical and optical properties"*** *submitted by* ***Mr. Prasanta Mandal****, who got registered his name on* ***14/01/2015****, registration number* ***D-7/ISLM/1/15*** *for the award of* ***Ph.D. (Science)*** *degree of* ***Jadavpur University****. This thesis is entirely based on his original work under the guidance of* ***Prof. Gopes Chandra Das*** *and* ***Prof. Kalyan Kumar Chattopadhyay****. His thesis, or any portion of it, has never before been presented for any academic award, comprising degrees/diplomas, anywhere.*

Gopes Chandra Das 10/01/2023

(Prof. Gopes Chandra Das)

Retired Professor

Dept. of Metallurgical and Material Engineering

Jadavpur University

Kolkata-700032, India

10.1.23

(Prof. Kalyan Kumar Chattopadhyay)

Professor and Head

Dept. of Physics

Jadavpur University

Kolkata-700032, India

Professor and Head
Department of Physics
Jadavpur University
Kolkata – 700 032

(Hd) Professor
Metallurgical & Material Engg. Dept.
Jadavpur University
Kolkata - 700032

"Declaration of originality"

I, ***Prasanta Mandal****, who become registered on* ***January 14, 2015****, hereby declare that this thesis entitled* ***"Development of some Cu based p-type transparent conducting oxides through novel doping strategy and investigation of its electrical and optical properties"*** *contains a literature review and original research completed for a doctoral thesis by the undersigned candidate.*

All data in this thesis were gathered and presented in conformity with accepted academic standards and ethical conduct. I certify that as required by such rules and conduct, I have properly cited and referred to any materials and findings that are not unique to this work.

I hereby also declare that I have examined this thesis in accordance with the "Policy on Anti Plagiarism, Jadavpur University, 2019", and that the iThenticate programme has determined that there is below 10 % level of similarity.

Signature of Candidate:

Date: Prasanta Mandal 10/01/2023

Certified by Supervisor(s):

1. Gopa Chandra Das 10/01/2023

(Prof.) Professor
Metallurgical & Material Engg. Dept.
Jadavpur University
Kolkata - 700032

2. 10.1.23

Professor and Head
Department of Physics
Jadavpur University
Kolkata – 700 032

Acknowledgments

I would like to take this opportunity to thank a lot of persons for their contributions with this submission of my Ph.D. thesis titled **"Development of some Cu based p-type transparent conducting oxides through novel doping strategy and investigation of its electrical and optical properties"**. The journey began in January 2015 and was carried out under the guidance of Prof. Kalyan Kr. Chattopadhyay at School of Materials Science & Nano Technology, Dept. of Physics in Jadavpur University and Prof. Gopes Chandra Das, Dept. of Metallurgical and Material Engineering in Jadavpur University.

I want to start by expressing my deep gratitude to Prof. Kalyan Kr. Chattopadhyay, who has been my co-supervisor for his assistance, counsel, encouragement, and for the chance he gave me to join his research team without whose enthusiastic assistance and useful guidance, I would not have been able to complete my work. I commend his scientific prowess and patient supervision. I express my sincere affection and respect for his observing abilities and philosophical insights not just in the realm of science, but also in a variety of real world applications.

I want to convey my sincere gratitude to my supervisor prof. Gopes Chandra Das for allowing me to conduct my research under his supervision. I will always be very appreciative of his careful and insightful scientific advice and also his continuous support for resourceful and independent thinking of research.

I am very grateful to the University Grants Commission (UGC), the Government of India under the 'University with potential for excellence scheme (UPE II) and the Department of Science and Technology (DST), the Government of India for their financial support during the course of my research work.

My parents deserve the utmost gratitude for their unyielding love and support throughout my life. I am really proud of my family since their support and prayers provided me the strength to keep going. I want to express my gratitude to my wife especially during the challenging moments for her love, support and patience.

I would like to express my gratitude to the School of Materials Science and Nanotechnology at Jadavpur University and its director Dr. Sourav Sarkar and also faculty member Dr. Chandan Kumar Ghosh for their assistance during my work. I also thank to the laboratory staff members of School of Materials Science and Nanotechnology and Dept. of physics for their genuine assistance and support in enabling me to conduct my experiments.

I want to convey my gratitude to all of my lab mates in the School of Materials Science and Nanotechnology for their assistance, encouragement and crucial contributions. I am especially thankful to my research collaborators Dr. Nilesh Mazumder, Dr. Rajarshi Roy, Dr. Subhajit Saha and Dr. Uttam Kumar Ghorai for their continuous cooperation and scientific needful discussions. I sincerely thank to Dr. N. Mazumder but I don't think that's enough to recognise his continuous effort of my research journey. I am also thankful to Dr. Nirmalya Sankar Das and Dr. Dipayan Sen for their various types of computational analysis and other discussions. They greatly influence my use of graphic arts in my manuscripts.

I gratefully acknowledge all of my senior and junior lab mates Dr. Biswajit Das, Dr. Soumen Maiti, Dr. Samrat Sarkar, Dr. Saswati Santra, Dr. Supratim Maity, Dr. Biplab Kr Chatterjee, Dr. Abu Jahid Akhtar, Dr. Rituparna Mukherjee, Mr. Bikram Kumar Das, Dr. Subhasish Thakur, Dr. Promita Howli, Mr. Nripen Besra, Mr. Saikat Sarkar, Dr. Tufan Paul, Mr. Kausik Sardar, Mr. Kausik Chandra, Dr. Karamjyoti Panigrahi, Mr. Anjan Das and Mr. Souvik Bhattacharjee for their valuable support and assistance during my research work. I would like to special thank Dr. Partha Hazra for their many scientific discussions and constant support during my part of research work. I also wish

to special thank M. Tech fellows Mr. Arnab Kabiraj and Ms. Kamalika Das for their assistance.

Finally, I wish to specifically thank my family for their unwavering love, support, and encouragement. Their endurance and selflessness served as a constant source of inspiration for me and will continue to do so throughout my life, inspiring me to go higher.

January 2023

Prasanta Mandal

School of Materials Science & Nanotechnology

Jadavpur University

Kolkata –700032

India

(Prasanta Mandal)

List of Tables

List of Figures

Figure 4.1: (a) X-ray powder diffraction patterns of the synthesized materials, exhibiting rhombohedral symmetry (PDF number 74-0983, space group $R\bar{3}m$, 166). (b) Rietveld refinement of $CuCr_{0.95}Mg_{0.05}O_{1.9}S_{0.1}$ sample considering the chemical formula $CuCr_{0.9701}O_{0.9867}S_{0.0061}Mg_{0.0302}$ in accordance with the result of energy dispersive X-ray spectrum. The black curve is the best fit from the Rietveld refinement using FULLPROF programme. The vertical lines indicate the positions of Bragg peaks and the blue curve represents the difference between the experimental and calculated intensities. (c) and (d) are schematics of side and top view respectively of the refined crystal

Figure 4.2: Band gap calculations of prepared powders from diffuse reflectance spectra using Kubelka-Munk function

Figure 4.3: (a) Temperature dependent DC conductivity for 80 – 300 K for $CuCr_{0.95}Mg_{0.05}O_2$ and $CuCr_{0.95}Mg_{0.05}O_{1.9}S_{0.1}$. AB, and DE are segments of the experimental data fitted assuming activated conduction and segment BC and EF showing the low temperature conductivity of $CuCr_{0.95}Mg_{0.05}O_2$ fitted considering variable range hopping mechanism (inset). (b) log – log representation of current – voltage for the prepared materials.

Figure 4.4: (a) Frequency dispersion of negative differential susceptance (3 V) and (b) admittance (0 V) of the pallets prepared with parallel capacitor geometry. Vertical lines in a and b are indicating the positions of f_r and A_{max} respectively of the corresponding materials. Inset of b is showing the dispersion of admittance of $CuCrO_2$ and $CuCrO_{1.9}S_{0.1}$ across same frequency range

Figure 5.1: X-ray diffraction $(\theta - 2\theta)$ profile of (a) CCO, (b) $\mathrm{CCO/Li_{Cr}^{\bullet\bullet}}$, (c) $\mathrm{CCO/S_O^{\times}}$ and (d) $\mathrm{CCO/(Li_{Cr}^{\bullet\bullet} + S_O^{\times})}$. The solid red lines express the best fit obtained for the experimental data (blue circles) from the Rietveld analysis using the FULLPROF programme. The short vertical green lines indicate the position of associated the Bragg peaks. The black curve represents the difference between the experimental and calculated profile intensities, which is displayed at the bottom of the graph. The schematics of side view of the refined supercells are obtained from DIAMOND. Gray, orange, red, yellow and green balls are representing copper (Cu), Lithium (Li) oxygen (O), sulfur (S) and chromium (Cr), respectively

Figure 5.2: (a) XPS survey spectra of CCO and $\mathrm{CCO/(Li_{Cr}^{\bullet\bullet} + S_O^{\times})}$. (b) Relative increase in Cu^{2+} content in $\mathrm{CCO/(Li_{Cr}^{\bullet\bullet} + S_O^{\times})}$ compared to CCO is delineated along with minor energy red shift of Cu

2*p* doublet upon co-doping. (c) HR spectra of Li 1s and S 2p. (d) XPS spectra of the VB region of CCO and $CCO/(Li_{Cr}^{\bullet\bullet} + S_O^{\times})$, which is deconvoluted considering major orbital contributions for elucidating VB dispersion

Figure 5.3: The plot of $[F(R_{inf})h\nu]^2$ versus $h\nu$ for obtaining optical band gap from diffuse reflectance spectra of all the materials. The x-intercept of extrapolated black dotted lines is signifying the associated optical energy gap.

Figure 5.4: (a) Frequency dependent of negative differential susceptance spectra with 2V external bias and (b) admittance spectra of $CuCr_{1-x}Li_xO_{2-y}S_y$.Vertical lines of (a) and (b) are implying the positions of f_r and A_{max} respectively and (c) Log – log representation of current–voltage profile of the corresponding materials

Figure 5.5: (a) Temperature dependence DC Arrhenius plots of $\ln(\sigma)$ vs. T^{-1} for $CCO/Li_{Cr}^{\bullet\bullet}$ and $CCO/(Li_{Cr}^{\bullet\bullet} + S_O^{\times})$ with the temperature between 185- 300 K. (b) The low temperature (4 - 30 K) conductivity plots of $\ln(\sigma T^{1/2})$ vs. $T^{-1/4}$ for $CCO/Li_{Cr}^{\bullet\bullet}$ and $CCO/(Li_{Cr}^{\bullet\bullet} + S_O^{\times})$, considering three-dimensional (3D) Mott's VRH mechanism.(c) and (d) DC Arrhenius plots of $\ln(\sigma)$ vs. T^{-1} for $CCO/(Li_{Cr}^{\bullet\bullet} + S_O^{\times})$ and $CCO/Li_{Cr}^{\bullet\bullet}$ with the temperature between 4 - 30 K (e) The crossover region with the temperature between 30 –180 K.

Figure 6.1: x-ray diffraction pattern (black circle) of $CuCr_{1-x}M_xO_{2-y}S_y$. The solid red line corresponds to the best fit profile obtained by Rietveld refinement and the blue line ($Y_{obs} - Y_{calc}$) is the intensity difference between calculations and experimental data. Vertical green lines indicate the position of associated Bragg lines

Figure 6.2: DR spectra of $CuCr_{1-x}M_xO_{2-y}S_y$ calculated by Kubelka-Munk function. The x-intercept of extrapolated dotted lines is indicating the associated optical gap

Figure 6.3: σ_{dc} vs. T for $CuCr_{1-x}M_xO_{2-y}S_y$

Figure 6.4: (a) Admittance spectra of $CuCr_{1-x}M_xO_{2-y}S_y$ (b) Log – log representation of current–voltage characteristics of the corresponding materials

Figure 7.1: (a) Evaluating the differences between the XRD patterns of microcrystalline and also nanocrystalline materials. The inset displays the advancement of milling methods for 4, 12, and

20 h. (b) The XRD pattern for the *MICRO* material. The intensity differences among experimental results with Rietveld analysis is shown by Y_{obs} - Y_{calc}, and also the solid red line refers to the pattern generated from of the Rietveld analysis. (c) Using EDX measurements, the elemental composition was determined for nanocrystalline $CuAlO_2$ (d) crystalline size variation with milling time for *NANO* samples

Figure 7.2: (a) HRTEM image of nanocrystalline $CuAlO_2$ for 20 h BM, (b) SAED pattern for 4 h BM, and (c) SAED pattern for 20 h BM

Figure 7.3: Morphology of (a) *MICRO*- $CuAlO_2$ (b) *NANO*-$CuAlO_2$:4 hour (c) $CuAlO_2$:12 hours (d) $CuAlO_2$:20 hour obtained from Scanning electron microscope

Figure 7.4: Diffuse-reflectance spectrum for all synthesized materials

Figure 7.5: (a) Temperature dependent (150-300 K) DC Arrhenius plots for *MICRO* and *NANO*-$CuAlO_2$ (20 h). The lower temperature region (80-145 K) plot fitted with Mott's VRH conduction mechanism (inset). (b) log – log Characteristics of I-V plot for all prepared materials

Figure 7.6: Frequency dependence admittance plot for *MICRO* and size variant (4 − 20 h) nanocrystalline $CuAlO_2$ at 2 V external biased

Figure 7.7: (a) Frequency dependence dielectric constant (ε') and (b) dielectric loss plot for *MICRO* and size variant (4−20 h) nanocrystalline $CuAlO_2$ at 2 V external biased

Figure 7.8: Frequency dependence ac conductivity plot for *MICRO* and size variant (4− 20 h) nanocrystalline $CuAlO_2$ at 2 V external biased

List of Publications

(A) International journal papers:

1. **"A scheme of simultaneous cationic–anionic substitution in $CuCrO_2$ for transparent and superior p-type transport";**
   Prasanta Mandal, Nilesh Mazumder, Subhajit Saha, Uttam Kumar Ghorai, Rajarshi Roy, Gopes Chandra Das and Kalyan Kumar Chattopadhyay
   ***Journal of Physics D: Applied Physics*, 49 (2016) 275109.**
2. **"Experimental observation of valence band dispersion and increased hole conductivity in $CuCr_{1-x}Li_xO_{2-y}S_y$" ;**
   Prasanta Mandal, Nilesh Mazumder, Subhajit Saha, Uttam Kumar Ghorai, Rajarshi Roy, Gopes Chandra Das and Kalyan Kumar Chattopadhyay
   ***Current Applied Physics*, 25 (2021) 90–96.**
3. **"Exploring the effect of hole localization on the charge–phonon dynamics of hole doped delafossite";**
   Nilesh Mazumder, **Prasanta Mandal**, Rajarshi Roy, Uttam Kumar Ghorai, Subhajit Saha and Kalyan Kumar Chattopadhyay
   ***Journal of Physics: Condensed Matter*, 29 (2017) 375701.**
4. **"Negative capacitance in $ZnO_{1-x}Ch_x$ (Ch = S, Se, Te): Role of localized charge recombination";**
   Nilesh Mazumder, **Prasanta Mandal**, Rajarshi Roy, Uttam Kumar Ghorai, Subhajit Saha, and Kalyan Kumar Chattopadhyay
   ***Journal of Applied Physics* 121, 135702 (2017).**

❖ This thesis is supported by published works (first author) and one unpublished work is **"Investigation of the transport and structural properties of nanocrystalline delafossite *p*-$CuAlO_2$";**
Prasanta Mandal, Nilesh Mazumder, Kamalika Das, Gopes Chandra Das and Kalyan Kumar Chattopadhyay. (Manuscript communicated)

(B) Paper published in the Conference Proceedings:

1. **En route to the conductivity bottleneck in p-type $CuCr_{1-x}M_xO_{2-y}$ Sy (M = Li, Mg)**
   Prasanta Mandal, N. Mazumder, A. J. Akhtar, R. Roy, and K. K. Chattopadhyay
   ***AIP Conference Proceedings* 1832, 110054 (2017).**

(C) Paper presentations in National and International Conferences:

1. **61st DAE Solid State Physics Symposium-2016, KITT University, Bhubaneswar, 26-30 December.** Presented a paper. "En route to the Conductivity Bottleneck in p-type Delafossites".
2. **Recent Advances in Materials Science-2017, Dept. of Industrial Chemistry, Ramkrishna Mission Vidyamandira, 28-29 March.** Presented a paper. "Spectroscopic and Microscopic Evidence of Charge ordering and Relaxor Behavior in Delafossite $CuCrO_2$".
3. **NCRDNN-2019, 29-31 January,** Organization by the School of Materials Science & Nanotechnology, Jadavpur University, Kolkata.

Contents

Abstract

An order of materials known as transparent conductive oxides (TCOs) combined excellent electrical conductivity with optical transparency. Due to these aspects the evolution regarding *p*-TCOs conveyed for a numerous application including "smart" windows to "multifunctional" transparent electronics for upcoming power-efficient optoelectronic gadgets. The commerce of abundant utilization is influence by *n*-TCOs and manufacture of a potentially useful fully functional transparent device is constrained by the absence of an appropriate *p*-type equivalent, which could be considered as a development in technology. Delafossite $CuCrO_2$ is an optimistic potential material to attain the suitable for large spectrum of *p*-TCOs possibilities. Nowadays, *p*-TCOs are being presented the supreme trade-off in between electrical as well as optical analysis. The famous scientist C. Friedel discovered the mineral for first time report in 1873 while analyzing from Siberia. The great mineralogist G. Delafosse was honored by having the mineral identified the significant name "delafossite" (1796-1878). The compounds are a part of ternary oxides having a popular chemical formula $A^{+1}B^{+3}O_2$, which comprise layer of linearly coordinated A cations stacking between edge-shared BO_6 octahedron. The monovalent ions (A^{+1}) are inclined and attached to the trivalent ions (B^{+3}) at the center of normal oxygen octahedral. In 1993, after NiO as a first report in *p*-TCOs there have been variant applications documented up until this point. Due to its high conductivity in $CuCrO_2$ doped with Mg has been identified as a suitable candidate for *p*-TCOs.

The purpose of this thesis is to the simultaneously both cationic-anionic doping strategy in *p*-$CuCrO_2$, improving their electrical transport, structural and optical response. Furthermore, we have examined the structural, optical as well as electrical transport characteristics of nanocrystalline *p*-$CuAlO_2$ ceramics. Chapter 1 begins with a common introduction of TCOs and includes the

historical content with their chemical and various physical characteristics describe in details to provide a technological structure for some of recently developed materials. Review of correlated literature on Copper based delafossite is consider along with some ground-breaking reports represent in chapter 2.

The basic operating procedures and broad summary about the crucial characterization tools that are utilized during the entire study discusses briefly in chapter 3. By doping cationic and anionic simultaneously are performed in prototype *p*-$CuCrO_2$ to maintain the transparency while improving electrical conductivity explains in chapter 4. Mg and S are applied as dopant elements at Cr and O-sites respectively with varying concentrations and it's confirmed by Rietveld analysis. It is obvious that all doped materials are in transparent region. In electrical measurements twice time enhance conductivity for co-doped materials with increase metallicity.

Chapter 5 introduce Li ion doping at Cr site and S ion doping at O site in the host *p*-$CuCrO_2$ to validate the resulting band dispersion experimentally over the contribution from shallow *S 3p* acceptors with maintaining transparency. To investigate how site dependent hole inducing affects the corresponding changes in physical and transport properties. Four fold increasing in electrical conductivity upon the cationic-anionic doping. Here a pair of conduction mechanism thermally activated above 180 K and 3D VRH conduction below 30 K is highlighted. Chapter 6 carries out and is compared to temperature dependence hole conductivity and identified for Li and S doping more likely way to cross the bottleneck threshold than Mg and S doping in *p*-$CuCrO_2$ and also enhance metallicity.

Chapter 7 investigated to the effect of reducing grain size impact of the transport and structural analysis of *p*-$CuAlO_2$ and is acquired via ball milling process with good transparency. Electrical analysis of micro and nano samples reveals that the hole conductivity for the nanocrystalline materials reduces by several orders.

Chapter 8 finally, concludes by summarizing the main culminations of this thesis and discussing potential areas for upcoming research.

Prasanta Mandal

(Prasanta Mandal)

January 2023

School of Materials Science & Nanotechnology

Jadavpur University

Kolkata –700032

India

1. Introduction

Chapter 1

1.1. A brief overview of TCOs:

A significant amount of research advances among the semiconductor physics over the last centuries. Due to its many real-world uses, several people have shown interest in the semiconductor materials. Consequently, material processing has also grown in importance as a research area. Many groundbreaking material as well as technology have becomes available now, each with unique qualities for variety applications. However, the greatest obstacle to the development of new technological improvements is frequently a lack of resources. Modern material scientists are especially interested in creating materials that preserve their desired qualities under extreme surroundings. The ultimate goal is material scientists to identify ways to raise productivity while decreasing the production cost.

Termed TCOs, these material most momentous areas of research interest have already establish abundant applications in devices that requiring for transparent contacts. The various class of materials used in these devices, which involve semiconductors, metal, plastic, ceramics and polymer have necessitated for TCOs. An order of TCOs material displaying with combination of high conductivity (~ 10^4 S cm^{-1}) including high transparency (>80%) in visual range, which acquired wide band gap nature. Due to their special features TCOs are the foundation for many significant applications in modern and emerging technology [1-4]. Typical examples of TCOs use as organic LED, solar cells, LCD, “low-e” windows and FPD [5-8]. TCOs are being applied sometimes as

active layers in transparent film transistors, gas sensors, UV LED and detectors also [9-13]. Moreover, TCO is frequently utilized mostly in area of opto-electronic gadgets for long range.

In 1907, Badeker [14] was first to report conducting TCO films of CdO and which prepared via thermal oxidation. Since that time, its financial cultivation of films TCO has indeed been acknowledged, and even the selection of potential samples has also broadened. Afterwards, it was found numerous binary oxides and which exhibits superior transparent conducting feature. Few of these examples include PbO_2, CdO, Ti_2O_3, SnO_2, Ga_2O_3, ZnO, Sb_2O_5 and In_2O_3 [15, 16]. Out of this most TCO widely used such as In_2O_3 doped with Sn and SnO_2 doped with F in the modern industries due to their good optical as well as electrical capabilities [17]. The relatively scarcity and highly expensive of indium have significantly disadvantage for ITO; while FTO is more affordable, its need high temperature for deposition, which is limit applicability in devices. One benefit of employing a binary oxide as TCOs that because of theirs film deposition is generally simpler to control in contrast to multi- component and ternary oxides. Since the materials with impurity doped execute native as well as impurity donors, whereas undoped binary only have a few number of uses. Many examples of ternary oxides such as $CdIn_2O_4$, Cd_2SnO_4, and $CdSnO_3$ are good candidates was developed in prior 1980 for TCOs [18, 19].

New materials for TCO are being extensively researched to be able to provide TCO films that are appropriate for specialized applications. In 1990s, TCO materials made of multicomponent compounds such as $ZnSnO_3$, Zn_2SnO_4, $GaInO_3$ and $MgIn_2O_4$ along with consisting of combination with ternary oxides [20-22]. The benefit of the multicomponent compounds is that of their physical, electrical, chemical and optical properties might be controlled with chemical compositions. Also $MgIn_2O_4$- $Zn_2In_2O_5$ multicomponent oxide was described as a novel TCO material via magnetron sputtering by Minami in 1999 [23]. Currently, the ultimate conductivity ($1.3x10^4$ Scm^{-1}) reported in ITO as thin film which was grown by PLD method [24]. Many of metals thin film such as Cu, Fe,

Ag, and Au, etc. has also reported with similar properties. The stability along with toughness thin films based upon wide gap conducting oxides, however; significantly outweigh those of metallic films.

However, TCO materials have the potential to be used as transparent contacts. It is commonly acknowledged that the astounding improvements in the production of Si-based devices that have reached their practical limit [25], and therefore a completely new strategy is necessary: Materials made of oxide are predicted to be a key component of such advancements [26-28]. TCOs present alluring possibilities for the development of high achievement transparent electronics, opening up a plethora of novel integration and technological opportunities [29], such as entirely electronic display panels, or energy creation due to photovoltaic cells covertly integrated in the windows of business buildings. There are good reasons to believe that in TCOs field will eventually move beyond its recent stage into transparent contacts predominating to innovative and fascinating concepts for electronic systems.

The TCOs conductivity might be varying greatly, ranging from metal to insulator. However, the majority of these TCOs exist within n-type, in which the electrical conduction is carried out by electrons. The creation of *p*-TCOs is required by reason of the fabrication entire transparent *pn* junctions. Transparent FET thin films have fabricated by using *n*-TCOs [30]. Understanding the fundamental characteristics of TCOs is necessary for the representation of TCOs by using *p* and *n*-type materials.

Anyhow, to get toward open electronic device concepts, we must comprehend the causes of TCOs electrical conductivity. Such that this may be enhanced, managed, and the invention of novel materials with specialized features. In this field, there has recently been significant advancement with findings that deviate from accepted viewpoints.

1.2. The valuable properties:

1.2.1. Electrical conductivity

To comprehend the conduction phenomena at play, numerous studies on the electrical characteristics of TCOs have been conducted. To following the relationship $\sigma = ne\mu$, the conductivity (σ) defined by S cm^{-1} of TCOs films is directly proportional carrier mobility (μ) and free carrier density (n) i.e. (“electrons” in *n*-TCOs and “holes” in *P*- TCOs), whereas *e* is elementary charge (1.6 $x10^{-19}$ C). As a result, it is clear that the films become conductive; they must either varying from stoichiometry or undergo intrinsic doping, like oxygen vacancies or extrinsic doping with external impurities. The doping might be accomplished across interstitial implantations, vacations as well as substitution and which depending upon the materials or the dopant type. This means the TCO described with that contribution due to situating of either an anion or a cation with the intention of doping. Systematic research has been done to examine the impact of several parameters, including substrate temperature, dopant concentration and film thickness etc.[31, 32] in TCO films for electrical characteristics.

The highest value conductivity of TCO films is primarily due to stoichiometric deviation. Donor sites associated to oxygen vacancies serve as the source of free electrons in TCO films. Such donor sites might be easily formed to chemical reduction. Among the greatest important elements carrier mobility key variable with effect of conductivity of TCO films. The mobility of carrier in polycrystalline TCO films depends on the process through which carrier scattering. In semiconducting films, there are many difference scattering mechanisms at play including piezoelectric, ionized impurity, grain boundary, optical phonon and electron-electron [33, 34].

Consequently, a compromise might be reached while designing doped in TCOs due to that free electrons density. Due to this restriction, a good TCO materials has to be low resistivity (preferably $\rho \sim 10^{-3}$ to 10^{-4} Ω·cm), a high carrier mobility (usually $\mu \sim 50$ to70 $cm^2V^{-1}s^{-1}$) and keeping below carrier concentration below 2×10^{21} cm^{-3} [35]. In TCOs, the scattering ionized impurities is appears the main theme limitation of its carrier mobility. Lee [36] described the relation among the mobility of electrons and concentrations in ITO films with deposited through magnetron sputtering (DC) under difference conditions. It must be highlighted that the scattering on grain boundary has significant that impact on ZnO with carrier concentrations is 2×10^{20} cm^{-3} compared to ITO concentrations [37]. Additionally, the impurity ionized scattering model described to ZnO, In_2O_3 and SnO_2 for TCO films [38]. Furthermore, it is important to understand that Sn-In_2O_3 act in accordance with the example scatters of the carrier and these scattering occurrences most likely define the intrinsic restriction of carrier mobility.

1.2.2. Optical transparency

TCOs films optical characteristics are greatly influenced by microstructure, deposition parameters, growth methods and impurities. The transmittance, absorptance as well as reflectance spectra across a wide range of UV-visible-IR spectrum are typically used to investigate TCO films. Their wide optical gaps ($E_g > 3$ eV) are direct cause of their transparency in the NIR and visible regime. The word "optical" energy gap should be understood to refer energy of photon which exhibits an absorption coefficient in absorption spectrum. In comparison, energy gaps which including “electronic” as well as "optical" are not consistently identical since few materials execute a lower electronic energy gap i.e. optically indirect or direct but not excitable. As a result, the materials exhibit very short band gap absorption. The materials consequently exhibit very little absorption at

the electronic energy gap. This is particularly clear in the instance of In_2O_3, which optical gap energy shows that 3.6 eV, despite having an electronic but has dipole forbidden gap energy just 2.8 eV [39]. The minimal electronic energy gap due to the massive in cations reduces antibonding state at the CBM. The significantly larger optical energy gaps due to transitions in between the electronic gap energy are forbidden across the symmetry and the allowed optical transition below at the VBM is almost 1 eV.

The two boundaries (near-IR & near-UV) that defined transmission window are directly correlated with the carrier concentration. For TCOs, the transmission window shifted to lower wavelength with raises the carrier concentration. Many examples [40-42] of these shifts in TCOs includes FTO, AZO (ZnO doped with Al), GZO and ITO with increased carrier concentrations (2.3-10 × $10^{20}cm^{-3}$). Furthermore, for AZO observed a high blue shifts to 0.5 eV [43].

The spectral dependency demonstrates that TCO is transparent and exhibits dielectric like behaviour above the limitation of smaller transparency but below the transparency bands higher wavelength limit (known as the plasma wavelength). Beyond the wavelength of the plasma, it treated as a metal and either absorbs or reflects of light. Due to the doping that results of shifting the plasma's wavelength, which causes the TCO's transparency to decrease. The TCOs requires a compromise for used in applications of photovoltaics with respect to spectral response. Thus, depending upon the material employed and its doping, the kind of oxide and its doping are generally optimized with TCOs to have a transparency range.

Optical measures are also frequently used to evaluate the film quality. In the lower quality of TCOs, the deep levels of emissions occurring with low transmittance are attributed to the various lattice defects. As a result, in ordering to achieve better transmittance, the defects in TCOs primarily those related to oxygen must be significantly decreased by the use of ideal growing conditions.

1.3. Evolution and Growth (TCOs):

A number of techniques that are commonly employed to deposit oxides based thin films. These several deposition techniques and conditions are greatly influenced by the optical as with electrical characteristics of ITO films.

Generalities about growth methods

The earliest TCOs layer advancements of a substrate such as silicon and glasses were inexpensive liquid chemistry methods, like as hydrothermal growth, sol-gel deposition and electrochemical deposits [44-46]. The first techniques for creating TCO layers of a substrate by spray pyrolysis and sputtering were created in 1970 to become better quality of layers and consequently, in control of the growth process [47]. A few years ago, more advanced methods have become available, like molecular beam epistaxy (MBE) and pulsed laser assisted deposition (PLD) [48, 49]. The extensive development trade of TCOs served as wide-ranging for the making of these current techniques demanding improved management of repeatability while enhancing the layer's crystallinity.

Recently, researchers have produced nanostructured layers which based on nanofibers, nanoparticles in response to either improvement in the electrical along with optical performance of TCO layers or the creation of new applications. The primary TCO films deposition and growth processes, highlighted by numerous instances pertaining to unique TCO films, in order to draw attention to the individual experimental and growth concerns that need to held into account.

Sputtering

Thin films TCO are frequently deposited using the sputtering procedure. There are numerous methods for sputtering that could be applied in several of temperature ranges, including DC sputtering, radio frequency, ion beam or magnetron sputtering. The industrial field has found both (DC & RF) to be particularly intriguing among the aforementioned approaches because they provide vast area sputtering systems, high rates deposition and reproducibility. Additionally, it has been reported that ITO films created by magnetron sputtering (DC) at ambient temperature are often amorphous and have a large electrical resistance [50]. However, certain substrates or applications, like as solar cells or electronic devices, need for a low temperature deposition due to larger temperatures risk damaging the structure of electronics devices directly [51].

E-beam and thermal evaporator

Metallic Sn and In powders are used in directly thermal evaporator and electron beam techniques to grow ITO films. Since indium (In) has a higher vapors pressure than tin (Sn), it will more readily evaporate, changing the composition of alloys. Furthermore, studied how different procedures for heat post-deposition conducts affected to the optical, electrical and microstructural characteristics of thin films (ITO) and that was made through an e- beam [52]. The samples were deposited upon Si-wafer along with glass substrate. Following deposition, the samples underwent a 30-minute annealing process in the air at temperatures range $(200\text{-}500)^0$C. They discovered that the material was amorphous at small temperatures, whereas the size of the crystallites noticeably increased with temperature. The typical grain size was observed to be around 10 - 25 nm for temperature at 300°C, but it rises to around 15 - 50 nm at higher temperatures. The literature also has recognized this connection with structure and temperature [53].

Spray pyrolysis

A chemical interaction of gases species appearing with a heated substrate occurs inside the spray pyrolysis process. The benefits of this method, which is now widely used to create electrodes, include the potential for accumulating over very huge surfaces, the deposit frame's comparatively modest price and the deposit's usage of a low temperature enabling the deposit on different substrates. The further benefit from scientific standpoint, that it makes possible to develop coatings with an excellent qualities on various substrate without any vacuum. Additionally, compared to the equipment, it's also thought to be rather affordable. The disadvantage regarding ITO films seems to be the scarcity of sources in thermally stable or volatile materials. Various investigations using this method to production of ZnO films over glass substrates have been conducted to examine how the change characteristics of the films with changing deposition parameters [54].

1.4. Applications:

To restate, in addition to having optical transparency within the chosen wavelength range, the materials (TCO) for evaluation should also be a feature of large conductivity along with order to achieve the electrode specifications and also being generally acceptable with active layer substance. In practical TCOs are applied as electrodes primarily within the case of solar cells or LEDs because they are energy-related and make a big impact on our lives.

LEDs

LEDs have attracted of numerous interest in the discipline of FPDs throughout the world. The uses of LEDs are significant, and the efficiency of LEDs is strongly influenced by the metal oxide

semiconducting materials. LEDs based upon GaN must provide excellent optical fluxes in particular to be utilized for generalized illumination and to open the door to lower energy usage. A large injection current required for this, ideally with large efficiency in power conversion. Several strategies, including substrate design, layers of p-contact and textured surfaces could be used separately to increase the effectiveness for extraction [55, 56]. In order to increase the extractive efficiency, TCOs are utilized a transparent electrodes in organic and GaN-LEDs.

TCOs improved lateral conductivity provides further benefits. As is reasonable to assume, the weak conductivity of *p*-GaN, which leads to the commonly named current-crowding process, may be a factor inside the performance decay of LEDs. The resulting temperature and progressively uneven current have a negative impact on the devices stability along with its operating voltage and emission effectiveness. A layer of Ni/Au was already widely studied as the transparent material in earlier phases of the production of GaN-LEDs; its transparency is less than 70% that count on the wavelength with thickness [57]. There is a thoroughly reviewed regarding ohmic-contact methods involving *p*-GaN for GaN- LEDs [58].

Relevant information on the ohmic properties of GZO, ITO and also AZO may be obtained in the corresponding references [59, 60]. As was already said, ITO seems to have transmittance ($\geq$ 90%), which is significantly greater than Ni/Au thin layer. The luminescence intensity and power generated of the ITO-LEDs are substantially enhanced as a result. ITO is needed the primary TCO material utilized in GaN-LEDs to date. To make it even better as there are absence of photon-blocking bonding wire in the way of photons that are retrieved from the surface of device, flip-chip design allows for a stronger LED output. The addition of TCOs buffer thin layers potentially raise the efficiency with which emitting devices execute with their functional duration.

Solar cells

The termed ‘photovoltaic effect’, It efficiently transforms incident light energy to electrical power, is utilized by ‘solar cells’. The separation of free carriers pair (electron-hole) produced by solar photons occurs at the interface between two substances with various conducting polarities. Since they produce sustainable, renewable energy that will lessen our reliance on fossil fuels, solar cells are an incredibly favorable renewable energy source.

TCOs are employed in solar cells for such a variety of purposes. Solar cells could be classified in bulk devices; junction based film devices and recently developed technology, such as organic cells, high-efficient junction cells and many mores. The earliest phase of photovoltaic devices has been referred to as modular made of semiconductor materials that are constructed by bulk wafer. Energy prices remain too expensive to make a meaningful impact on the industry for power generation. A large portion of the market is concentrated upon that technology with the lowest price per unit of power production. The two primary methods for lowering rate of solar electricity are improving cell efficiency with reducing cost. Thin film manufacturing devices are more affordable since they use lesser material than Si (bulk). Devices utilizing polymers including dyes materials, that comprise a diverse array of innovative designs, are another alternative strategy aimed at lowering energy prices [61]. Despite being less effective than semiconducting devices at the moment, such cells remain appealing because of their ease of use and inexpensive manufacturing costs.

TCOs are employed as electrode materials in numerous varieties of thin film cells, including CdTe, Si and CIGS. In order to successfully use TCO films in the applications solar cell, greater carrier mobilities are needed. Si-based film devices also benefit and are slighter expensive for the reasoning that they utilize less silicon than bulk wafer-based devices. TCO layers, which are employed the transparent electrodes for Si cells, are hence extremely important to device operation [62]. In

replacement of ITO, FTO films are frequently utilized for solar cells [63]. The most prevalent substrate is FTO, however expense SnO_2 glass substrates with wide surfaces are not yet employed. However, AZO has arrives a potential TCO compound in solar cells. The AZO composition is more transparent and conductible than conventional glass substrates. Furthermore, in a high humidity climate, AZO degrades significantly more quickly than FTO or ITO [64]. The configuration of glass substrate arrangement is typically used in the fabrication of solar cells (CdTe). The buffers generally frequently made of SnO_2 layers, but $ZnSnO_x$ films have also been suggested [65]. In contrast to film cells, dyes and are subsequently used in PV systems. Cost effectiveness is these devices key advantage, although organic PV cells energy conversion efficiencies are higher. Additionally, transparent anodes made of TCO components could be employed to OPV devices [66].

1.5. Objectives of the thesis:

The conductive properties of TCOs could be varying from metal to insulator, and can also be altered in many other ways. Furthermore, the majority of such TCOs have *n*-type, in which the electrical conduction is carried out by electrons. The production of *p*-TCOs is required for the manufacturing include all junctions in *p*-*n* systems which are transparent. The optimum conductivity of *p*-TCOs documented up to this point is still several orders of magnitude lower than *n*-TCOs that are widely accessible. Therefore, this hinders the growth of efficient devices in high-volume production. It was discovered revealed non-stoichiometric oxidation strong interaction inside this material has such a restriction on how that can boost the components conductivity. Therefore, it appears that the materials were modified intentionally the apparent method to improve its conductivity. When

defects are added to oxide semiconductors, its electrical as well as optical characteristics frequently undergo drastic alterations. It must be necessary to identify the correct dopant and the doped method, the goal is to obtain exceptional qualities. Numerous theoretical publications that suggest different doping agents and techniques to improve these compounds the electrical characteristics have been established. Delafossite $CuCrO_2$ is an optimistic potential material to attain the suitable for large spectrum of *p*-TCOs possibilities. Nowadays, *p*-TCOs are being presented the supreme trade-off in between electrical as well as optical analysis. Co-doping of *p*-TCOs is thus a crucial research field for such creation of photonics and spintronics technologies of greater quality. The discovery of *p*-TCO compounds remains in its early stages. The *p*-TCOs have the potential to create a broad range of novel devices, despite the verity that their conductivity remains lesser compared to *n*-type counterparts. The main purpose of this thesis is to the simultaneously both cationic-anionic doping scheme in *p*-$CuCrO_2$, improving their electrical transport, structural and optical response.

Bulk *p*-TCOs physical properties are very diverse than those of nano-structured TCOs. Ball milling as top-down process, produces considerably a various sizes range of delafossites composition than bulk *p*-TCO. Furthermore, we have examined the structural, optical as well as electrical transport characteristics of nanocrystalline *p*-$CuAlO_2$ ceramics.

The main research goals are highlighted inside this thesis:

- To create solid state heating-based copper delafossites with a crystalline phase that is visible and conducting utilizing a low-cost and precisely controllable method.
- To study the *p*-TCO, $CuCrO_2$ is chosen as host matrix and both cation and anion doping are performed simultaneously in order to improve the conductivity while maintaining the transparency.
- To introduce Li ion doped at Cr site and S ion doped at O site in the host *p*-$CuCrO_2$ to

investigate physical as well as chemical properties and validate the resulting band dispersion experimentally.

- To compared to temperature dependence hole conductivity and identified for Li and S doping more likely way to cross the bottleneck threshold than Mg and S doping in *P*-$CuCrO_2$.
- To generate size variation crystalline phase optically transparent along with Cu-based conductivity delafossite materials are utilizing a top-down technique.

- To study the transport, optical as well as structural features of nanocrystalline *P*-$CuAlO_2$ with size variation.

This thesis is separated into 8 well-documented chapters that are focused on the research ideas with applications. Chapter 1 starts with a common introduction of TCOs and includes the historical content with their detailed discussion of practical implications in contemporary life. Chapter 2 represents review of correlated literature on Copper based delafossite also their classifications are considered along with some ground-breaking reports. The detailed documentation of the experimental setups utilized in the thesis is provided in chapter 3. By doping cationic and anionic simultaneously are performed in prototype *p*-$CuCrO_2$ to maintain the transparency while improving electrical conductivity explains in chapters 4. Chapter 5 introduce Li ion doping at Cr site and S ion doping at O site in the host *p*-$CuCrO_2$ to validate the resulting band dispersion experimentally over the contribution from shallow *S 3p* acceptors with maintaining transparency. To investigate how site dependent hole inducing affects the corresponding changes in physical and transport properties. .Chapter 6 carries out and is compared to temperature dependence hole conductivity and identified for Li and S doping more likely way to cross the bottleneck threshold than Mg and S doping in *p*-

$CuCrO_2$ and also enhance metallicity. Chapter 7 investigated to the result of reducing grain size influence of transport with structural analysis of *p*-$CuAlO_2$ and is acquired via ball milling process with good transparency. In this section 8, the entire dissertation gets summarized, and also the researches future prospects are discussed. This information may assist future researchers working in this field by pointing them in the right direction.

1.6. References:

1. X. G. Yu, T. J. Marks and A. Facchetti, Nat. Mater. 15 (4), 383-396 (2016).

2. K. Ellmer, Nat. Photonics 6 (12), 808-816 (2012).

3. E. Fortunato, D. Ginley, H. Hosono and D. C. Paine, MRS Bull. 32 (3), 242-247 (2007).

4. R. M. P. Barquinha, L. Pereira and E. Fortunato, Transparent Oxide Electronics: From Materials to Devices, Wiley, 1st edition (2012).

5. T. Minami, Semicond. Sci. Technol. 20 (4), S35-S44 (2005).

6. C. G. Granqvist, Sol. Energy Mater. Sol. Cells 91 (17), 1529-1598 (2007).

7. G. Frank, E. Kauer and H. Kostlin, Thin Solid Films 77 (1-3), 107-117 (1981).

8. R. L. Hoffman, B. J. Norris and J. F. Wager, Appl. Phys. Lett. 82 (5), 733-735 (2003).

9. K. Nomura, H. Ohta, K. Ueda, T. Kamiya, M. Hirano and H. Hosono, Science 300 (5623), 1269-1272 (2003).

10. K. Nomura, H. Ohta, A. Takagi, T. Kamiya, M. Hirano and H. Hosono, Nature 432 (7016), 488-492 (2004).

11. E. Fortunato, P. Barquinha and R. Martins, Adv. Mater. 24 (22), 2945-2986 (2012).

12. H. Ohta and H. Hosono, Mater. Today 7 (6), 42-51 (2004).

13. Z. W. Pan, Z. R. Dai and Z. L. Wang, Science 291 (5510), 1947-1949 (2001).

14. K.Badeker, and Ann,Phys 22(1907) 749.

15. DS Ginley, C Bright. Transparent Conducting Oxides. MRS Bull. 2011; 25: 15–18.

16. T Minami. New n-Type Transparent Conducting Oxides. MRS Bull. 2011; 25: 38–44.17.

17. C G Granqvist and A Hultaker 2002 Thin Solid Films 411 1–5.

18. T.J.Coutts, X.Wu, W.P.Mulligan and J.M.Webb , J.Electron.Mater. 25(1996)935.

19. T.Minami, MRS Bulletin25 (2000)38.

20. H.Un'no, N.Hikuma, T.Omata, N.Ueda, T.Hashimoto and H.Kawazoe, Jpn.J.Appl.Phys.Part2, Lett 32(1992)l1260.

21. T.Minami, H.Sonohara, S.Takata, and H.Sato, Jpn.J.Appl.Phys., Part2, Lett.33(1994)L1963.

22. R.J.Cava, J.M.Phillips, J.Kwo, G.A.Thomas, R.B.van Dover, S.A.Carter, J.J.Karjewski, W.F.Peck,J.M.Marshall,and D.H.Rapkine, Appl.Phys.Lett 649(1994)2071.

23. T.Minami, S.Takata, T.Kakumu,and H.Sonohara, Thin Solid Films 270(1995)22.

24. H.Ohta, M.Orita,M.Hirano,H.Tanji, H.Kawazoe and H.Hosono Appl. Phys. Lett 77(2000)475.

25. T N Theis and P M Solomon 2010 Science 327 1600–1.

26. G Thomas 1997 Nature 389 907–8.

27. J F Wager 2003 Science 300 1245–6.

28. A P Ramirez 2007 Science 315 1377–8.

29. H Ohta and H Hosono 2004 Mater. Today 7 42–51.

30. K.Nomura, H.Ohta, A.Takagi, T.Kamiya, M.Hirano and H.Hosono, Nature 432(2004)488.

31. N.S.Murty, G.K.Bhagawat, and S.R.Jawalekar, Thin Solid Films 92(1982)347.

32. Y.Shigesato, and D.C.Paine, Appl.Phys.Lett.62(1993)1268.

33. J.Bardeen,and W.Shockley, Phys.Rev. 80(1950)72.

34. A.R.Huston, J.Appl.Phys. 32(1961)2287.

35. Dixon SC, Scanlon DO, Carmalt CJ, Parkin IP, Lifka H, Gierth R, J Mater Chem C. 2016; 4: 6946–6961.

36. H.-C. Lee, Appl. Surf. Sci. 252 (2006) 3428–3435.

37. K. Ellmer, R. Mientus, Thin Solid Films 516 (2008) 4620–4627.

38. J.R. Bellingham, W.A. Phillips, C.J. Adkins, J. Mater. Sci. Lett. 11 (1992) 263–265.

39. A. Walsh, J. L. F. Da Silva, S. H. Wei, C. Korber, A. Klein, L. F. J. Piper, A. DeMasi, K. E. Smith, G. Panaccione, P. Torelli, D. J. Payne, A. Bourlange and R. G. Egdell, Phys. Rev. Lett. 100 (16), 4 (2008).

40. I. Hamberg, C.G. Granqvist, J. Appl. Phys. 60 (1986) R123–R159.

41. M. Oshima, Y. Takemoto, K. Yoshino, Phys. Status Solidi C 6 (2009) 1124–1126.

42. B.-Z. Dong, H. Hu, G.-J. Fang, X.-Z. Zhao, D.-Y. Zheng, Y.-P. Sun, J. Appl. Phys. 103 (2008) 073711-7.

43. B.Z. Dong, G.J. Fang, J.F. Wang, W.J. Guan, X.Z. Zhao, J. Appl. Phys. 101 (2007) 033713-7.

44. J. S. Wellings, N. B. Chaure, S. N. Heavens, and I. M. Dharmadasa, Thin Solid Films, 516 (2008) 3893–3898.

45. T. Sahoo et al., Hydrothermal growth and characterization of ZnO thin film on sapphire (0001) substrate with p-GaN buffer layer, Thin Solid Films, 516 (2008) 8244–8247.

46. L. Znaidi, Sol–gel-deposited ZnO thin films: A review, Materials Science & Engineering B, 1–3 (2010) 18–30.

47. S. Takayanagi, T. Yanagitani, and M. Matsukawa, Journal of Crystal Growth, 363 (2013) 22-24.

48. S.-M. Park, T. Ikegami, K. Ebihara, and P.-K. Shin, Applied Surface Science, 253 (2006) 1522–1527.

49. Information on https://www.semanticscholar.org/paper/Basics-of-Molecular-Beam-Epitaxy-(-MBE-)-Rinaldi/c4b463caba1e85265210a62b5cb42b8dba4ce0fd.

50. V. Teixeira, H. N. Cui, L. J. Meng, E. Fortunato, and R. Martins, Thin Solid Films, 420–421

(2002) 70–75.

51. W. Liu and S. Cheng, J. Semicond., 32 (2011).

52. A. S. A. C. Diniz, Renewable Energy, 36 (2011) 1153–1165.

53. A. S. A. C. Diniz, C. J. Kiely, I. Elfalla, R. D. Pilkington, and A. E. Hill, Renewable Energy, 5, (1994).

54. A. Ashour, M. A. Kaid, N. Z. El-Sayed, and A. A. Ibrahim, Applied Surface Science, 252 (2006) 7844–7848.

55. M. Yamada, T. Mitani, Y. Narukawa, S. Shioji, I. Niki, S. Sonobe, K. Deguchi, M. Sano, T. Mukai, Japan. J. Appl. Phys. 2 41(2002) L1431–L1433.

56. S.I. Na, G.Y. Ha, D.S. Han, S.S. Kim, J.Y. Kim, J.H. Lim, D.J. Kim, K.I. Min, S.J. Park, IEEE Photonics Technol. Lett. 18 (2006) 1512–1514.

57. J.K. Sheu, Y.K. Su, G.C. Chi, M.J. Jou, C.M. Chang, C.C. Liu, W.C. Hung, Appl. Phys. Lett. 74 (1999) 2340–2342.

58. J. O Song, J.-S. Ha, T.-Y. Seong, IEEE Trans. Electron Devices 57 (1) (2010) 42–59.

59. X. Li, H.Y. Liu, S. Liu, X. Ni, M. Wu, V. Avrutin, N. Izyumskaya, Ü. Özgür, H. Morkoç, Phys. Stat. Solidi (a) 207 (2010) 1993–1996.

60. C.H. Kuo, C.L. Yeh, P.H. Chen, W.C. Lai, C.J. Tun, J.K. Sheu, G.C. Chi, Electrochem. Solid-State Lett. 11 (9) (2008) H269–H271.

61. Y. Hamakawa, Thin-Film Solar Cells: Next Generation Photovoltaics and its Applications, Springer, Berlin, 2004.

62. J. Műller, B. Rech, J. Springer, M. Vanecek, Sol. Energy 77 (2004) 917–930.

63. Q. Qiao, J. Beck, R. Lumpkin, J. Pretko, J.T. Mcleskey Jr., Sol. Energy Mater. Sol. Cells 90 (2006) 1034–1040.

64. F.J. Pern, R. Noufi, X. Li, C. DeHart, B. To, Presented at the 33rd IEEE Photovoltaic Specialists Conference San Diego,California, May 11–16, 2008.

65. X.Z. Wu, Sol. Energy 77 (6) (2004) 803–814.

66. J. Owen, M.S. Son, K.-H. Yoo, B.D. Ahn, S.Y. Lee, Appl. Phys. Lett. 90 (2007) 033512-3.

2. Literature survey

Chapter 2

2.1. Overview of p-TCOs:

The key characteristics and possible uses of semiconducting films comprise the most significant oxide-based semiconductors that have material specialists extremely interested. The most frequently referred to it as TCOs, which have employed extensively in the optoelectronics field and in research disciplines for such a long period. These films have good optical transparency with in visible light and large electric conductivity for ambient temperature. A deeper comprehension of the fundamental qualities of TCOs is necessary for this field's progress. The growth of novel TCOs with excellent transparency but instead strong electrical conductivity is encouraged by a number of factors. The construction of active devices employing TCOs has received minimal attention despite the fact that TCOs offer a broad range of possibilities [1, 2]. The reasons for this are the majority of the common and frequently utilized *n*-TCO, although the *p*-counterparts (*p*-TCOs), which become crucial in junction devices, have been shockingly lacking in films form for such a long period of time.

It's therefore the highest necessity to produce numerous many *p*-TCO variations having excellent physical as well as electrical features, at least similar to the current, extensively *n*-TCOs, for such a variety of technological applications. To create novel *p*-TCOs using different deposition processes, intensive effort has been expended within that field for the past few years. Numerous researches have also been executed to fully the comprehend of structural, optical and also electrical properties in *p*-TCOs. Since this is a new area of TCO appliances, a detailed evaluation of significant

advancements for *p*-TCO compounds with respect to the various positioning strategies and film characteristics is necessary. Nagarajan or Tate among others published concise and partial reviews on this area in the past [3, 4]. Additionally, Norton offered a comprehensive description of the creation and characteristics of oxide films, briefly mentioning the significance of *p*-TCOs [5].

Also few more publications about just the creation of films *p*-TCO have already been reported to since. By using magnetron sputtering, produced semi-transparent *p*-NiO films [6]. By simultaneously adding NH_3 with in gas phase and more Zn there in source ZnO, a *p*-ZnO film was observed [7]. By using standard RF-sputtering, Minami along his associates created a unique multiple component oxides made up of Ag_2O with In_2O_3 [8].

Since Kawazoe and others (1997) initially proposed a method for discovering oxides semiconductors exhibiting *p*-types conductivity and superior optical transmittance, significant advancements in *p*-TCOs have been documented [9]. Afterward, this team kept looking for novel materials to support their chemically design of films TCO. They chose $SrCu_2O_2$ like a promising material and contrasted films with and without K doping [10]. Although both films underwent post-annealing, they nevertheless displayed significant conductivity and poor carrier density. $CuBO_2$ has received an increasing amount of interest since the publication of Kawazoe. For instance, $CuScO_2$ synthesised through solid reaction produced good conductivity but displayed extremely low transparent as in visual region [11]. Later using PLD methods, alternative material $CuGaO_2$ was tested; this one produced great transparency and yet low conductivity [12]. The most significant of such a novel type of TCOs is the delafossites structure *p*-TCOs film with formula ABO_2 (A= Cu, Ag) and also its doping variants, which given the new area of dimension ‘transparent electronics’ (TEs). As a results the development of this particular *p*-TCOs, whole transparent *p*-*n* devices that

could serve as 'functional windows' are created [13, 14]. After that, the throughout last decades, synthesis of a considerable lot of *p*-TCO Cu-based compounds with a broad variety of electro-optical performances has been recorded. There are also reports of significant *p*-TCO non-delafossite films exhibiting excellent electro-optical characteristics including Cu_2SrO_2, LnCuOCh (Ln=La, Nd, Y, Gd, Sm, Pr and Ch=S, Se).

2.2. Chemical design of p-TCOs:

Because it is extremely difficult to create binary oxides having conductivity *p*-type, the majority of TCOs currently available in use can be *n*-type in origin. The initial challenge inside the chemical designing of *p*-TCO compounds is to minimize the localisation of positive holes on the edges of valence-band of the oxides i.e. that localisation originates from the metallic oxides ionic nature [9, 15]. Due to the fact that *O 2p* levels are so much lower lying than with valence orbit of the metal atoms, positive holes eventually create deep acceptor levels [16]. Therefore, when a positives hole is performed successfully, say through interstitial doping, it's going to be localised on such a single oxygen atom. Thus, such holes have low conductivity or low carrier mobility since they need sufficient potential to cross very high barriers in order to move around inside the crystalline lattice.

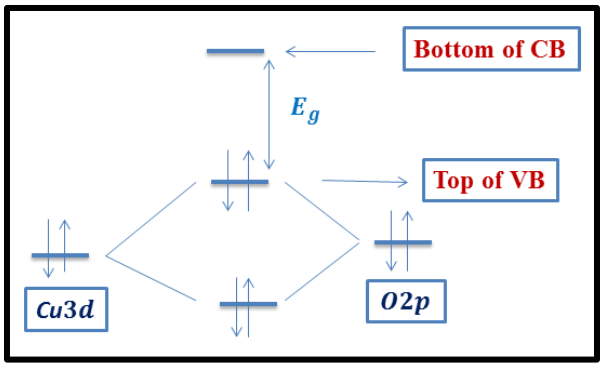

Figure 2.1: Schematic illustration of CMVB technique.

The addition of covalency to the metal-oxygen interaction to create an extending valence-band configuration is one potential remedy, known as chemical modulation of the valence band (CMVB). The key feature of the suggested method (Figure 2.1) for getting *p*-TCOs is that it has this feature. But still the selection of the significant cationic species to use with the CMVB approach is the subsequent prerequisite. Findings demonstrated also that needed cationic- species are Cu^{+} with a $3d^{10}$-closed shells as well as Ag^{+} with a $4d^{10}$-closed shells. Even though a few transitions metal-cations with such an extended d-shell might be able the satisfying energy needed, this is not what is anticipated for transparent compounds since these cations typically exhibit considerable coloration related in *d-d* transitions. As a result, attention was already directed to the cation atoms with closed electronic configuration ($d^{10}s^{0}$). As a consequence of pairs of electrons occupying both atomic orbitals, the anti-bonding level a valence-band edge becomes the level with the maximum occupancy.

2.3. Crystalline structure and properties:

Delafossite materials are ternary oxides, and their typical structure is 'ABO_2'. The 'A' cation within that structure is associated linearly with two O-atoms is occupied by such a superior metal cation that is usually as in +1 oxidized state. Significant A cations contain Cu, Ag, Pt and Pd. The interatomic separation between such A cations are typically relatively modest in most materials. With such a primary metal cation that has a +3 charged, this 'B' cations are situated in deformed edge shared octahedral (BO_6). In order to meet that condition, cations may be *p*-block metals elements like Al, In, Ga, Pb, Sn and Bi, transition metallic ions like Co, Fe, Cr and Au and also rare earth metals like Eu, Ce, La, Sc and Nd. For B_3AO, the oxygen atoms forms co-ordination of

pseudo-tetrahedral, which includes three B with one A cations. The alternating two layers comprise a delafossite structure, which may be observed as follows; an edge-sharing octahedral layer of BO_6 flattened in respect of c-axis and then a layer of plane A cations arranged in a triangle configuration. Delafossites composition and crystalline structure could arise either one of the following two polytype, based upon the way each layers is oriented during stacking. The hexagon 2H- types is created from the stacked a dual layers also with alternate A layer positioned 180 degrees from one another. This hexagonal symmetry belongs to *P63/mmc* space group. If the A layers are being staking with of the dual layers positioned the same direction in relation to one another, the formation of rhombohedral structure 3R-type, however displaced from one another in a three-layered sequences. Its space group for this rhombohedral crystalline structure is $R\bar{3}m$. The demonstrates two polytypes as well [Figure 2.2 (a & b)].

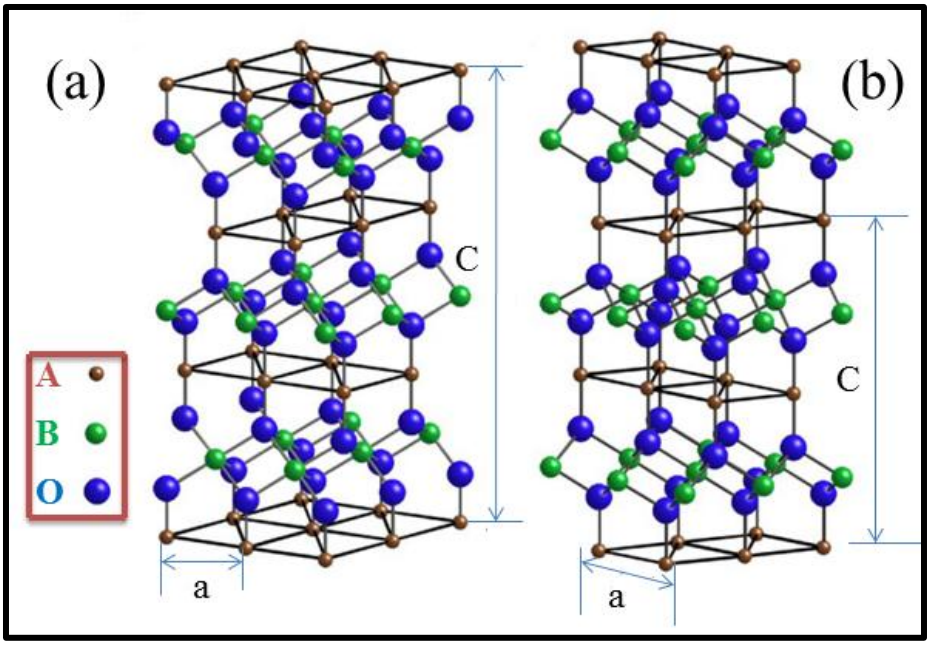

Figure 2.2: The delafossite crystalline structure.(a) 3R-polytype [$R\bar{3}m$] and (b) 2H-polytype [P63/mmc].

$CuCrO_2$ is a member of the delafossite compounds that stands apart from the others in terms of its exceptional qualities.

Energy storage

In addition, $CuCrO_2$ is regarded as an especially desirable electrode material utilizing the Li-ion battery. The primary explanation for $CuCrO_2$, reversible Li- storage gadgets comprises the bonds (Li-O) breakage & recovery during Li insertion or extraction. An employed carbon-coating to generate Li batteries anodes out of $CuCrO_2$ [17]. They discovered that its rise from (1.6 - 2.2 Li) in Li-storage capabilities for each units. The charging/discharging cycled, therefore, shows essentially little capacity losses.

Thermoelectric properties

$CuCrO_2$ compounds performed really well with thermoelectric (TE) materials because to their large thermal stabilities, phonon transport, adjustable electronic characteristics and also very well-established production processes [18-21]. The compounds that have high power ratings or beneficial thermoelectric characteristics were created using $CuCrO_2$ doped with Mg [22]. In addition to displaying a high relatively steady Seebeck-coefficient (SC) in such a range of temperatures, its component also is highly stable. Due to these benefits, $CuCrO_2$ doped with Mg compounds are well suited to be employed in transparent-TE devices, thin-film technologies that are miniature, including extremely accurate temperatures measuring instruments, among other applications.

Water splitting

From both (acidic or alkali) conditions, $CuCrO_2$ exhibits excellent stability. This compounds shows better photo-activity under perchloric acid. The $CuCrO_2$ compounds developed through using sol-gel techniques exhibits enhanced oxygen or protons reductions rates when compared to conventional water splitting substances [23]. Considering that this behaviour was observed without the use of charged extraction surfaces is even more significant, since it raises the possibility of water splitting advanced technologies.

Gas sensitivity

The fundamental component of such a superior ozone detector could be $CuCrO_2$, which has special gas-sensing capabilities. The resistance regarding to an ozone sensor comprising $CuCrO_2$ (Micro/Nano) crystals reduces in an ozone environment, but nearly recovers with its initial amount whenever the ozone gases is turned off. $CuCrO_2$ has an additional carrier density at the surfaces enhanced region while ozone gas still present, which is where the ozone sensitivities of materials come from. $CuCrO_2$, which was synthesized using sol-gel or hydrothermal techniques, responds to ozone gas well at ambient temperature and therefore is readily recyclable [24].

Electronic properties

$CuCrO_2$ could be utilised to create a diversity of transparent technologies with compatible *n*-TCO materials according to its superior opto-electronic capabilities. By using PLD techniques, a heterojunctions containing ZnO with Mg-CuCrO2 films was fabricated, which displays I-V properties [25]. In order to maximise capability of DS-solar cells (DSSC),

$CuCrO_2$ strong conductivity invents it an important component. DSSC with Mg-$CuCrO_2$ as the solid-state electrolytes (SSEs) has been discovered to display improved photocatalytic activity [26].

Ferromagnetic properties

$CuCrO_2$ displays superconducting capabilities, an intrinsic paramagnetic into anti-ferromagnetic transitions (23 K), with significant ferromagnetic characteristics at ambient temperature in $CuCrO_2$: Fe [27]. Therefore it is practical to investigate novel superconductors that the used trans-superconductivity obtained by $CuCrO_2$.

2.4. p-TCOs with delafossite structure:

2.4.1. Cu-based delafossites ($CuB^{III}O_2$)

$CuAlO_2$ is the primary and most significant component in *p*-TCOs. Almost 65 years have passed since the discovery with this compound [28]. Initially, the report of its conduction (*p*-type) was obtained in1984 [29], even though it was initially produced in transparent films with potential use such as p-TCO technologies [9]. In-depth research has also been done on these materials structural along with physical characteristics [30, 31]. Additionally, these group's p-TCO films include $CuInO_2$ and also $CuGaO_2$ [32, 33]. Numerous publications documented that which is electronic structure & crystalline properties of these compounds [34-36]. Dopant variations of a number of comparable varieties in p-TCO films, such as $CuCrO_2$ doped with Mg, $CuYO_2$ doped with Ca, $CuScO_2$ doped with Mg, $CuInO_2$ doped with Ca etc. [37-39]. Furthermore, this compounds crystalline information including theoretical simulation has also described in the variety of

publications [40, 41]. There have been reports of the creation of various extremely resistant novel delafossite compounds in solid form, including $CuZnO_2$: Sb, $CuFeO_2$: V, $CuMgO_2$: Sb, $CuMnO_2$: Sb, $CuCoO_2$: Sb etc. [42, 43]. Films made of $CuNiO_2$ doped with Sn have been found same team to have acceptable visual transparency as well as conductivity.

2.4.2. Ag-based delafossites ($AgB^{III}O_2$)

The majority of delafossite compounds with Cu-based used for *p*-semiconductors. It's really challenging to create comparable with Ag-delafossite compounds via a traditional solid-state approach. $AgInO_2$, an *n*-type compound, represented the first discovery of delafossite films, which is an Ag-based [44]. After being exposed to oxygen with pressure/fluorine, this was subsequently found the $AgInO_2$ with Mg doped powder evolved a *p*-type character including very weak conductivity [45]. The same team has created a number of related delafossite compounds, all of which are mainly available in solid form, such as $AgGaO_2$, $AgScO_2$ and $AgCrO_2$. There haven't been any findings of film productions among these compounds up to now, and each of these powders displayed extremely low conductivity. Additionally, $AgCoO_2$ a delafossite-based film with conductivity *p*-type, was the focus of the initial study [3]. The film demonstrated a respectable level of conductivity with transparency in visual range. The higher level of combining in between *Co* $3d^{10}$ with *O* $2p^6$ orbitals, which leads to more delocalised of holes, could be a reason with this film's superior conductivity to another Ag-delafossite compounds [46]. It was farther observed to exist in doped forms in various alternative Ag-delafossites, including $AgZnO_2$: Sb and $AgNiO_2$: Sb. Cu-delafossites have really been compared favourably to Ag-delafossites, with the previous category

being recommended to produce higher transparent conductivity due to they have a considerable carrier mobility [47].

2.5. Dopant $CuCrO_2$:

Undoped $CuCrO_2$ is extremely resistive *p*-type oxides material. Using $CuCrO_2$ conduction mechanism, the proper doping treatment is applied to reduce bond lengths (Cu-Cu) and therefore enhance the materials conductivity [48]. To date, Mg^{2+}, Ni^{2+}, and also other substitute ions were employed as dopants to enhance the carrier conductivity as well as optical transmission of $CuCrO_2$.

2.5.1. Mg^{2+} doped $CuCrO_2$

The first study on $CuCrO_2$ doped with Mg^{2+} was reported in [38]. They determined that $CuCrO_2$ had a highest Mg doped content of 5%. While $MgCr_2O_4$ phase [49] would emerge whenever the doped content is higher than 5%. The film was developed exhibiting conductivity (220 S/cm) at 5% doping concentrations of Mg, with a thickness (~250 nm), the typical transmittance was nearly 50% in visible regime. $CuCrO_2$ doped with Mg (5%) has a large Seebeck coefficient at 300 K, it has been reported. Okuda and co-workers [50] provided a thorough and comprehensive explanation of the link between the conductivity & Seebeck coefficient of polycrystalline $CuCrO_2$: Mg ($0<x<0.04$). As could be shown, there is a minimal familiarity among the variations in resistivity with Seebeck coefficient of $CuCrO_2$: Mg ($x>0.03$) and the impacts of temperatures on resistivity and also Seebeck coefficient remain steady or consistent. Considering also the reported [20] connection between dopant concentration along with lattice parameters. According to other sources, the theoretical justification for this defect-producing replacement of Mg^{2+} into Cr^{3+} was provided. Additionally,

Mg^{2+} substituting Cr^{3+} results in reduced energy generation of *p*-defects. It enhances carrier conductivity by making it simple to create the ionisation level inside the energy gap. According to earlier studies, the localised spins of Cr ions along with the carrier concentrations of the both influence of Seebeck coefficient; the one is more important at extreme temps, whereas the latter is more important at relatively lower temperature [51].

2.5.2. Ni^{2+} doped $CuCrO_2$

The prior article provided a thorough analysis of the effect that doped Ni^{2+} concentrations influences the electrical characteristics of $CuCrO_2$: Ni compounds [52]. They discovered that of such materials had the superior opto-electronic properties through conducting systematic analyses into their carrier density, transparency, electrical conductivity, and many other capabilities. Additionally, demonstrates that Ni^{2+} dopant concentration impacts the modification of physical characteristics. According to earlier theoretical and also experiments findings, Ni^{2+} dopant may produce crystal deformation in $CuCrO_2$: Ni, which will increase carrier scattering [53, 54]. Ni has an extremely strong solubility for $CuCrO_2$, which is one of the main benefits of employing as a dopant since it can efficiently enhance the carrier density. In contrast to Mg^{2+} dopant, which invariably causes the impurities phases in the film of $CuCrO_2$, whereas Ni^{2+} does not generate it. Ni-doped $CuCrO_2$ has a relatively high transparency with in visual range. Despite the fact that Ni dopant might be highly soluble, earlier results demonstrate that $CuCrO_2$ photo-electric feature was mostly noticeably enhanced whenever the Ni component percentage varies [55].

2.6. Synthesis method of delafossites:

Several synthesized techniques including both metals (Pd, Pt) with semiconductors (Cu, Ag) delafossites were disclosed mostly in initial studies. The group (VIII & IB) metal elements instabilities inside the delafossite crystal structure create many significant processing issues. This really is particularly true considering the exact stoichiometry controls needed to obtain repeatable observations of resistivity as well as carrier mobility among such compounds. The majority of delafossite materials could be produced through solid state processes when there is high pressure. Alternative reaction pathways are better suitable for several materials.

2.6.1. Low temperature method

The creation of highly crystallinity phases comprising the new metal oxides Ag_2O, PdO, and PtO is complicated by the lower operating temperature [56]. Numerous closed system or some other synthesis strategies with small temperature have been used to get about this obstacle. The wet-chemical procedures known as metathesis, hydrothermal, oxidising flux, cation exchange, high-pressure and some other chemical processes are all of significant relevance. The halide selected of a new metal is interacted with such a cation oxides precursor inside a covered silicate ampoule during metathetical processes to create crystalline phase of delafossites [57]. For synthesising, nothing additional pressure is needed. Equation (1) and (2) provide illustrations of metathetical processes for the creation of $CuFeO_2$ and $PdCoO_2$.

$CuCl + LiFeO_2 \rightarrow CuFeO_2 + LiCl$, (1) and $PdCl_2 + 2CoO \rightarrow PdCoO_2 + CoCl_2$ (2)

Oxides precursor undergoes hydrothermal processes in a solution of HCl or NaOH [58]. This types of reactions often take place at temperatures (500-700 °C) under external pressure and sealed with gold or platinum tubes. The act of producing $CuAlO_2$ and $AgInO_2$ at minimal pressures with temperatures has been accomplished using a freshly discovered hydrothermal synthesis process [59]. Cation exchange processes can be facilitated by oxidising flux methods of synthesis. The cation- exchange process is catalysed in this method using a point flux [60]. The sol-gel approach has also been used to synthesise small temperature organic solvent from a range of delafossite materials. $CuAlO_2$ also has been synthesised using other solutions synthesis techniques, including dip-coating with combinations of different Cu and Al sources [61].

2.6.2. Solid state method

Solid state route has also been successfully used to make a significant range of Cu-delafossite materials. Anyhow, it's also not practicable to make Ag, Pt or Pd-delafossite materials. $CuInO_2$ would be the lone exceptions, by which effective synthesize of delafossite phases can only be achieved through cation-exchange processes [62]. To be utilised as targets for such the PLD of $CuInO_2$ delafossite films, it's also possible to generate the ceramics materials of $Cu_2In_2O_5$ [63]. This is required to quenching with extreme temps (1000–1400°C) in order to stable metal Cu cations. For instance, the phase structures of $CuAlO_2$ ceramics appears at temps and along the interface across ($Cu+Al_2O_3$) mostly on reduction hand and among ($Cu_2O+CuAl_2O_4$) mostly on oxidation hand [64]. Several materials, including $CuAlO_2$, could be converted into single phase through quench under atmosphere. Alternative delafossite materials, like $CuGaO_2$, can be produced through powders format that use a large temperature controlled in atmospheric furnace being capable of

quenching [65]. A significant levels of crystallinity is generally shown through solid state generated powders or ceramics. Using this method, polycrystalline materials containing conventional densities could be generated theoretically around (60 or 90%).

2.6.3. Thin film method

It is essential that it be possible to implant the final compounds like a film on such a platform from that of an applied perspective, even if it is crucial to stabilise the delafossite crystalline phases in production. The film deposition substrates often need to be sintering samples. The several types of delafossite compounds that emerge have now been deposited using a number of deposition thin films processes. RF-sputtering, PLD and also CVD are a few examples of deposition of film methods frequently being used to synthesizing delafossite films. It has been possible to produce thin films include $CuInO_2$, $CuGaO_2$, $CuAlO_2$ and $AgInO_2$. $CuAlO_2$ films were created by CVD techniques using metal-organic reagents. The use of quartz substrates at temperature (745^0C) was necessary for this low- pressure depositing procedure [66]. One could simply understand the huge range in temps or vacuum pressures used from the previous description of the various film deposition procedures. Whenever contemplating the manufacturing of transparent technologies, substrate temps could pose a problem because extreme temps may create interaction across devices surfaces [67].

2.7. TCOs with non-delafossites:

2.7.1. Cu_2SrO_2

Although $SrCu_2O_2$ lacks of delafossite structure, it may be considered of as the continuation of Cu-delafossite. The identical dumbbell (O-Cu-O) zig-zag pattern chains that make up $SrCu_2O_2$ crystallized in such a tetragonal phase, which separate by SrO_6 octahedral sites. As a result, it is anticipated that dimension reduction likewise produces a significant energy gap in relation to Cu_2O, identical to that found in Cu delafossite. The both (doped/undoped) $SrCu_2O_2$ film produced through PLD techniques [10]. By applying photoelectron, DFT computations and also optical spectra, the electronic features of $SrCu_2O_2$ have also been studied [68, 69]. According to optical observations, $SrCu_2O_2$ is really a direct gaps semiconductor [68]. Contrarily, delafossite materials typically exhibit an indirect energy gap with in spectrum of visual light. Numerous opto-electronic technologies, including laser diodes or LEDs, would benefit greatly from a direct energy gap material. Additionally, $SrCu_2O_2$ films could be formed with minimal temperatures below at 400^0C, which reduces the amount of chemical process. $SrCu_2O_2$ has since attracted a lot of observation when utilised like an effective *p*-semiconductor in combination other widely accessible *n*-oxides semiconductor to generate heterojunctions *p*-*n* diodes, which shows $SrCu_2O_2$ could be employed like a *p*-TCO compounds in optically active devices [67, 68].

2.7.2. Spinel oxides

The fundamental goal in chemical designing is to alter the tops of VB by combining closed orbitals shells $Cu3d^{10}$ and $O2p^6$ to prevent oxygen ions from localising holes. This approach further raises the possibility that its behaviour with transition metals (Co, Ir and Rh) with such a d^6 conformation inside an octahedra oxygen coordinating potentially identical to $Cu3d^{10}$. This idea led to the discovery of a novel type of *p*-TCO (non-d^{10}), ZnM_2O_4 (M = Rh, Ir and Co) [70]. $ZnRh_2O_4$ films demonstrated *p*-TCOs performance in the first documented instance without purposeful doping [71]. The amorous $ZnRh_2O_4$ films have thus been shown to maintain their *p*-character while utilised in such a *p*-*n* diode depending on amorous *n*-$InGaZnO_4$ [70]. The edge-sharing nets (RhO_6), that are lesser impacted mostly by structural defects but are much more symmetric than the spinel phase and could be the source of *p*-conductivity inside the steady in such a network that is amorphous state. Following the invention of $ZnRh_2O_4$, the development of *p*-polycrystalline or epitaxial films including and $ZnIr_2O_4$, $ZnRhO_4$ and $ZnCoO_4$, prepared by PLD [72]. A re-consideration of opto-electronic elements for $ZnRh_2O_4$ owing to better films, hence, the necessities for these films identify and fix these core problems [73]. The most investigated ZnM_2O_4 is likely $ZnCo_2O_4$ spinels with very much focus aroused because of its potential applicability including photocatalysis and also supercapacitors [74]. Amorphous *p*-*n* diodes and also FETs have recently been considered utilising *p*-$ZnCo_2O_4$, demonstrating that material's possibilities as oxides-electronic devices [75].

2.7.3. Layered oxychalcogenides

The Cu-based ternary oxides *p*-TCOs exhibits still now lower carrier density and also mobility. Consequently, the CMVB were additionally expanded employing *p*-orbitals of chalcogen elements (S, Se, or Te) in place of oxygen ions. Considering that a much more dispersed at VBM was predicted theoretically, a strong hybridization between both Ch *p* and Cu *3d* orbitals, as a result of the improving covalency in between Ch and Cu atoms. In line with this idea, the initial compounds to be classified like *p*-TCOs were layered oxysulfide (LaCuOS) [76]. Whereas numerous earlier studies have revealed on the crystalline structure but also hole conduction of that kind of compounds [77]. LaCuOS crystalline structure is made of layers LaO with CuS are alternatively stacked across of c-axis [78]. By substituting La^{3+} with divalent (Mg^{2+}or Sr^{2+}) corresponding to the renowned hole-doped perovskite compounds, the conductivity could be adjusted across a broad range [79]. It's now been established that LaCuOS: Sr (doped 3% Sr), carrier densities but also conductivities could be improved. The measured carrier concentrations exceptionally large among many of *p*-TCOs throughout this finding [80]. It is significant to observe that the conductivity analysis indicates that doped film exhibits a degenerately semiconductive conduction response, and that as a result, offers significant possibility for creation of highly efficient *p*-TCOs to compete with its *n*-type equivalents. A wide optical gap conductor with all these additional qualities LaCuOS seems to have direct gap allowed (PL spectra) analysis also revealed this, which has potential use as an active area for opto-electronic equipment [81]. In addition, the significant optical gap material LnOCuCh could be significantly adjusted by altering the chemical contents in Ch places [82]. It is possible for the chemical tendency of the direct gap energy to

merely be understanding from reduction in energy levels. Furthermore, researchers has established polycrystalline solid or epitaxially films of LaCuOSe, which showed that the energy gap of such materials change nearly linear [83]. However, due to shorter energy gap in LaCuOSe and also the absorbance caused by in carrier states, this material produces lower transparency in visual region and is hence unsuited like a *p*-TCOs.

2.7.4. Binary and non-oxides

According to findings, multi-component oxide (In_2O_3-Ag_2O) films of this kind exhibit *p*-conduction and also have limited transmission in visible spectrum [8]. Ag_2O seems to be *p*-TCOs with a lower energy gap than In_2O_3, which are really renowned *n*-TCOs [84]. Moreover, a combination of both of these compounds exhibited conductivity of *p*-type. The increased hole conductivity of films could be caused by excessive oxygen ions inside the film, which is created by atmospheric heating, however the precise stoichiometric ratio hasn't yet been determined.

The hole conductivity of transparent binary oxide compounds such as NiO and also doped- ZnO. In practice, NiO film was actually the first *p*-TCO to be described [6], and it exhibited moderate conductivity with transparency in visible range. According to reports, the optical gap of such single NiO crystal measured in range (3.5-4.2 eV) [85]. The report suggested that increased hole conductivity of the compounds is caused both by the Ni vacancy and excessive oxygen at interstitial regions [86]. Rocksalt-like polycrystalline (*p*-NiO) has such a cubic symmetry and multiple groups thoroughly determined electronic structure including crystalline properties [87,

88]. However, it was uncertain if the transport carrier of NiO comprised conduction that is thermally activated (TAC), which is frequently observed in non-degenerate oxide semiconductors. Additionally, hydrated *p*- NiO is employed in a number of connected applications as such an effective electrochromic (EC) compounds [89, 90].

A further and crucial component of *p*-TCO technologies comprises with films of *p*-ZnO. Because both forms of ZnO could be utilised to create homo-junctions, a crucial feature under this area, the introduction of *p*-ZnO represents a significant development in transparent electronics (TEs) [91]. Co-doping donor or acceptor dopants as (Ga or N) in ZnO may produce *p*-ZnO, according to a recent calculation based upon first principles (DFT) [92]. To achieve the highest conductivity for *p*-ZnO, the simultaneously donor or acceptor doped into ZnO crystal at such an acceptor concentration that was two times of donor concentrations. However, other studies noted challenges and even an absence of consistency when employing the co-doping approach with *p*-ZnO [93, 94]. Furthermore, studied the evolution in the area of films *p*-ZnO and briefly discussed their significance and present situations [95]. The production film of p-ZnO is thoroughly explained and the associated sources herein. The possibilities for future applicability in this field of studies are enormous.

According to studies, non-oxide *p*-TCOs including BaCuSF with $BaCu_2S_2$ and can also be developed [96, 97]. α- $BaCu_2S_2$ films have been created, and that crystallise with relatively small temps in such an orthorhombic phase but also comparatively small energy gap including transmittance in visual spectrum [98]. The creation of pure and BaCuSF doped with K pellets and also films were subsequently found by the similar group. The area transparent electronics (TEs) nevertheless considers these materials to be important scientifically even while they cannot be categorised of *p*-TCO.

2.8. References:

1. Seager, CH, McIntyre DC, Warren WL, Tuttle BA. Appl Phys Lett 1996; 68: 2660-2662.

2. Prince MWJ, Gross-Holtz KO, Muller G, *et al*. Appl Phys Lett 1996; 68: 3650- 3652.

3. J. Tate, M.K. Jayaraj, A.D. Draeseke, T. Ulbrich, A.W. Sleight, K.A. Vanaja, R. Nagarajan, J.F. Wager, R.L. Hoffman, Thin Solid Films 411 (2002) 119.

4. R. Nagarajan, N. Duan, M.K. Jayaraj, J. Li, K.A. Vanaja, A. Yokochi, A. Draeseke, J. Tate, A.W. Sleight, Int. J. Inorg. Mater. 3 (2001) 265.

5. D.P. Norton, Mater. Sci. Eng. R. 43 (2004) 139.

6. H. Sato, T. Minami, S. Takata and T. Yamada, Thin Solid Film 236, 27 (1993).

7. K. Minegishi, Y. Koiwai, Y. Kikuchi, K. Yano and A. Shimizu, J. Appl. Phys. 36, L1453 (1997).

8. T. Minami, K. Shimokawa and T. Miyata, J. Vac. Sci. Technol. A 16(3), 1218 (1997).

9. H. Kawazoe, M. Yasukawa, H. Hyodo, M. Kurita, H. Yanagi and H. Hosono, Nature 389, 939 (1997).

10. A. Kudo, H. Yanagi, H. Hosono and H. Kawazoe, Appl. Phys. Lett. 73, 220 (1998).

11. N. Duan, A. W. Sleigh, M. K. Jayaraj and J. Tate, Appl. Phys. Lett. 77, 1325 (2000).

12. K. Ueda, T. Hase, H. Yanagi, H. Kawazoe, H. Hosono, H. Ohta, M. Orita and M. Hirano, J. Appl. Phys. 89, 1790 (2001).

13. D. Trivich, E. Y. Wang, R. J. Komp, and A. S. Kakar, 13th IEEE Photovoltaic Specialist Conf. Proc. (1978), p. 174.

14. D. Trivich, L. Fish, and R.J. Iwanowski, 16th IEEE PhotovoltaicSpecialist Conf. Proc. IEEE, New York (1982), p. 1072.

15. H Kawazoe, H Yanagi, K Ueda, H Hosono. MRS Bull 2000; pp. 28.

16. D DeVault. J Chem Educ 1944; 21: 526-534.

17. J. Shu, X. Zhu, T. Yi, Electrochim. Acta. 54 (2009) 2795–2799.

18. E. Guilmeau, A. Maignan, C. Martin, J. Electron. Mater. 38 (2009) 1104–1108.

19. K. Hayashi, K.I. Sato, K. Nozaki, T. Kajitani, Jan. J. Appl. Phys. 57 (2008) 59–63.

20. Y. Ono, K. Satoh, T. Nozaki, T. Kajitani, Jpn. J. Appl. Phys. 46 (2007) 1071–1075.

21. T. Okuda, N. Jufuku, S. Hidaka, N. Terada, Magnetic, Phys. Rev. B. 72 (2005) 144403.

22. I Sinnarasa, Y Thimont , L Presmanes , et al. [J]. Nanomaterials, 2017, 7(11):357.

23. A.K. Díaz-García, T. Lana-Villarreal, R. Gómez J. Mater. Chem. A. 3 (2015) 19683–19687.

24. S. Zhou, X. Fang, Z. Deng, D. Li, W. Dong, Sensors Actuators B. 143 (2009) 119–123.

25. T.W. Chiu, K. Tonooka, N. Kikuchi, Thin Solid Films. 516 (2008) 5941–5947.

26. M. Asemi, M. Ghanaatshoar, J. Mater. Sci. 52 (2017) 489–503.

27. C. Taddee, T. Kamwanna, V. Amornkitbamrung, Appl. Surf. Sci. (2016) 237–242.

28. H. Hahn, C. Lorent, Z. Anorg. Allg. Chem. 279 (1955) 281.

29. F.A. Benko, F.P. Koffyberg, J. Phys. Chem. Solids 45 (1984) 57.

30. T. Ishiguro, A. Kitazawa, N. Mizutani, M. Kato, J. Solid State Chem. 40 (1981) 170.

31. T. Ishiguro, N. Ishizawa, N. Mizutani, M. Kato, J. Solid State Chem. 41 (1982) 132.

32. H. Yanagi, T. Hase, S. Ibuki, K. Ueda, H. Hosono, Appl. Phys. Lett. 78 (2001) 1583.

33. H. Yanagi, K. Ueda, H. Ohta, M. Orita, M. Hirano, H. Hosono, Solid State Commun. 121 (2001) 15.

34. B.V. Kohler, M. Jansen, Z. Anorg. Allg. Chem. 543 (1986) 73.

35. M. Shimode, M. Sasaki, K. Mukaida, J. Solid State Chem. 151 (2000) 16.

36. J. Robertson, P.W. Peacock, M.D. Towler, R. Needs, Thin Solid Films 411 (2002) 96.

37. N. Duan, A.W. Sleight, M.K. Jayaraj, J. Tate, Appl. Phys. Lett. 77 (2000) 1325.

38. R. Nagarajan, A.D. Draeseke, A.W. Sleight, J. Tate, J. Appl. Phys. 89 (2001) 8022.

39. M.K. Jayaraj, A.D. Draeseke, J. Tate, A.W. Sleight, Thin Solid Films 397 (2001) 244.

40. L.F. Mattheiss, Phys. Rev. B 48 (1993) 18300.

41. O. Crottaz, F. Kubel, H. Schmid, J. Solid State Chem. 122 (1996) 247.

42. R. Nagarajan, N. Duan, M.K. Jayaraj, J. Li, K.A. Vanaja, A. Yokochi, A. Draeseke, J. Tate, A.W. Sleight, Int. J.Inorg. Mater. 3 (2001) 265.

43. R. Nagarajan, S. Uma, M.K. Jayaraj, J. Tate, A.W. Sleight, Solid State Sci. 4 (2002) 787.

44. T. Otabe, K. Ueda, A. Kudoh, H. Hosono, H. Kawazoe, Appl. Phys. Lett. 72 (1998) 1036.

45. R. Nagarajan, N. Duan, M.K. Jayaraj, J. Li, K.A. Vanaja, A. Yokochi, A. Draeseke, J. Tate, A.W. Sleight, Int. J.Inorg. Mater. 3 (2001) 265.

46. J.-S. Kang, J.H. Kwak, Y.J. Shin, S.W. Han, K.H. Kim, B.I. Min, Phys. Rev. B 61 (2000), 10682.

47. H.C. Kandpal, R. Seshadri, Solid State Sci. 4 (2002) 1045.

48. D. Li, X. D. Fang, Z. H. Deng, S. Zhou, R. H. Tao, W. W. Dong, Appl. Phys., 2007, 40, 4910–4915.

49. A Meagen . N. A Marquardt, D. P. Cann Ashmore, Thin Solid Films. 496.1(2006):146.

50. T. Okuda, K. Nakanishi, S. Miyasaka, and Y. Tokura, Phys. Rev. B 63, 113104 2001.

51. T. Okuda, T. Onoe, Y. Beppu, N. Terada, T. Doi. Magn. Mater., 2007, 310, 890–892.

52. Yi-Han Lin, Bing-Shen Yu, Chien-Ming Lei, Yongsheng Fu, et al. Thin Solid Films (2018) 705–710.

53. W.W. Liu, C.X. Lu, X.L. Wang, K. Liang, B.K. Tay, Journal of Materials Chemistry A3 (2015).

54. Z. Li, D. Ding, Q. Liu, C. Ning, X. Wang, Nanoscale Res. Lett. 9 (2014) 118.

55. Se-Yun Kim, Joon-Hyung Lee, Jeong-Joo Kim, Young-Woo Heo, Ceramics 558 International 44 (2018) 17743–17748.

56. R.D. Shannon, D.B. Rogers, C.T. Prewitt, Inorg. Chem. 10 (1971) 713.

57. J.B. Wiley, E.G. Gillan, R.B. Kaner, Mater. Res. Bull. 28 (1999) 893.

58. D.Y. Shahriari, A. Barnabe`, T.O. Mason, K.R. Poeppelmeier, Inorg.Chem. 40 (2001) 5734.

59. B.J. Ingram, G.B. Gonzalez, T.O. Mason, D. Shahriari, A. Barnabe`, D.Ko, K. Poppelmeier, Chem. Mater. 16 (2004) 5616.

60. J.E. Clayton, D.P. Cann, N. Ashmore, Thin Solid Films 411 (2002) 140.

61. K. Tonooka, K. Shimokawa, O. Nishimura, Thin Solid Films 411 (2002) 129.

62. M. Shimode, M. Sasaki, K. Mukaida, J. Solid State Chem. 151 (2000) 16.

63. C.W. Teplin, T. Kayadanova, D.L. Young, J.D. Perkins, D.S. Ginley, A.Ode, D.W. Readey, Appl. Phys. Lett. 85 (2004) 3789.

64. K.T. Jacob, C.B. Alcock, J. Am. Ceram. Soc. 58 (1975) 192.

65. R.B. Gall, N.A. Ashmore, M.A. Marquardt, X. Tan, D.P. Cann, J. AlloysCompd. 391 (2005) 262.

66. H. Gong, Y. Wang, Y. Luo, Appl. Phys. Lett. 76 (2000) 3959.

67. A. Kudo, H. Yanagi, K. Ueda, H. Hosono, H. Kawazoe, Y. Yano, Appl.Phys. Lett. 75 (1999) 2851.

68. H Ohta , M Orita , M Hirano , I Yagi , K Ueda and H Hosono 2002 J. Appl. Phys. 91 3074–8.

69. J P Hu , D J Payne , R G Egdell , N M Harrison and V R Dhanak 2007 Chem. Phys. Lett. 450 39–43.

70. Narushima S, Mizoguchi H, Shimizu K, Ueda K, Ohta H, Hirano M, Kamiya T and Hosono H 2003 Adv. Mater. 15 1409–13.

71. H Mizoguchi , M Hirano , S Fujitsu , T Takeuchi , K Ueda and H Hosono 2002 Appl. Phys. Lett. 80 1207–9.

72. M Dekkers, G Rijnders and D H A Blank 2007 Appl. Phys. Lett. 90 3.

73. M N Amini , H Dixit , R Saniz , D Lamoen and B Partoens 2014 Phys. Chem. Chem. Phys. 16 2588–96.

74. S B Wang , Z X Ding and X C Wang 2015 Chem. Commun. 51 1517–9.

75. P Schlupp , F L Schein , H von Wenckstern and M Grundmann 2015 Adv. Electron. Mater. 1 5.

76. K Ueda , S Inoue , S Hirose , H Kawazoe and H Hosono 2000 Appl. Phys. Lett. 77 2701–3.

77. K Ishikawa , S Kinoshita , Y Suzuki , S Matsuura , T Nakanishi , M Aizawa and Y Suzuki 1991 J. Electrochem. Soc. 138 1166–70.

78. M Palazzi 1981 C. R. Acad. Sci., Paris 292 789–91.

79. M Imada , A Fujimori and Y Tokura 1998 Rev. Mod. Phys. 70 1039–263.

80. H Hiramatsu , K Ueda , H Ohta , M Orita , M Hirano and H Hosono 2002 Appl. Phys. Lett. 81 598–600.

81. H Hosono 2007 Thin Solid Films 515 6000–14.

82. Y Goto , M Tanaki , Y Okusa , T Shibuya , K Yasuoka , M Matoba and Y Kamihara 2014 Appl. Phys. Lett. 105 022104.

83. K Ueda and H Hosono 2002 J. Appl. Phys. 91 4768–70.

84. E. Fortiu, F.L. Weichman, Phys. Status Solidi A 5 (1964) 515.

85. D. Adler, J. Feinleib, Phys. Rev. B 2 (1970) 3112.

86. E. Antolini, J. Mater. Sci. 27 (1992) 3335.

87. G.A. Slack, J. Appl. Phys. 31 (1960) 1571.

88. M.R. Norman, Phys. Rev. Lett. 64 (1990) 1162.

89. J.S.E.M. Svensson, C.G. Granqvist, Appl. Phys. Lett. 49 (1986) 1566.

90. S. Yamada, T. Yoshioka, M. Miyashita, K. Urabe, M. Kitao, J. Appl. Phys. 63 (1988) 2116.

91. G. Thomas, Nature 389 (1997) 907.

92. T. Yamamoto, H.K. Yoshida, Jpn. J. Appl. Phys. 38 (1999) L166.

93. K. Tamura, T. Makino, A. Tsukazaki, M. Sumiya, S. Fuke, T. Furumochi, M. Lippmaa, C.H. Chia, Y. Segawa,H. Koinuma, M. Kawasaki, Solid State Commun. 127 (2003) 265.

94. K. Nakahara, H. Takasu, P. Fons, A. Yamada, K. Iwata, K. Matsubara, R. Hunger, S. Niki, Appl. Phys. Lett. 79 (2001) 4139.

95. R. Triboulet, J. Perrie`re, Prog. Cryst. Growth Charact. Mater. 47 (2003) 65.

96. W.J. Wu, Y.Z. Huang, F. Wu, C. Dong, H. Chen, Z.X. Zhao, Mater. Res. Bull. 29 (1994) 505.

97. H. Yanagi, S. Park, A.D. Draeseke, D.A. Keszler, J. Tate, J. Solid State Chem. 175 (2003) 34.

98. J.E. Iglesias, K.E. Pachali, H. Stoinfink, J. Solid State Chem. 9 (1974) 6.

3. Experimental techniques

Chapter 3

3.1. Synthesis apparatus:

3.1.1. Box furnace

The materials was synthesised in a furnace that operated at the high temperature. The furnace utilising a front loaded pattern and could reach temperatures of up to 1200^0C. The temperature regulator furnace could be regulated heating rate to within 0.20^0C of accuracy. Typically, an aluminium boat was utilized to aid load the materials. A platinum sensor was applied to regulate the temperature, and Silicon carbide rods were linked in parallel to ensure consistent heating. The image of furnace is displayed in figure 3.1.

Figure 3.1: Box furnace

3.1.2. Planetary ball mill

In order to generate nanoparticles, mechanical milling (MM) is really known top-down method that has gained prominence, particularly in contexts where industrialized nanomaterials are prepared. This is because the method is straightforward, versatile, scalable, and inexpensive. The milling methodology is employed in this procedure to apply intense mechanical shearing forces that grind down solid materials, which is typically in micro dimensions to the nanosize. Because of the movements of the vials inside the system, planetary ball- milling (Fristch pulverisette 7) got their name shown in figure 3.2. Individual vials are revolved within their own directions in opposition towards the primary revolving disk while these vials get mounted to the rotating disk that revolves around on the axis. The heavy frictions as well as impact forces are utilized to mill the materials down into smaller sizes as the entire system rotates (at a speed of 300 rpm).

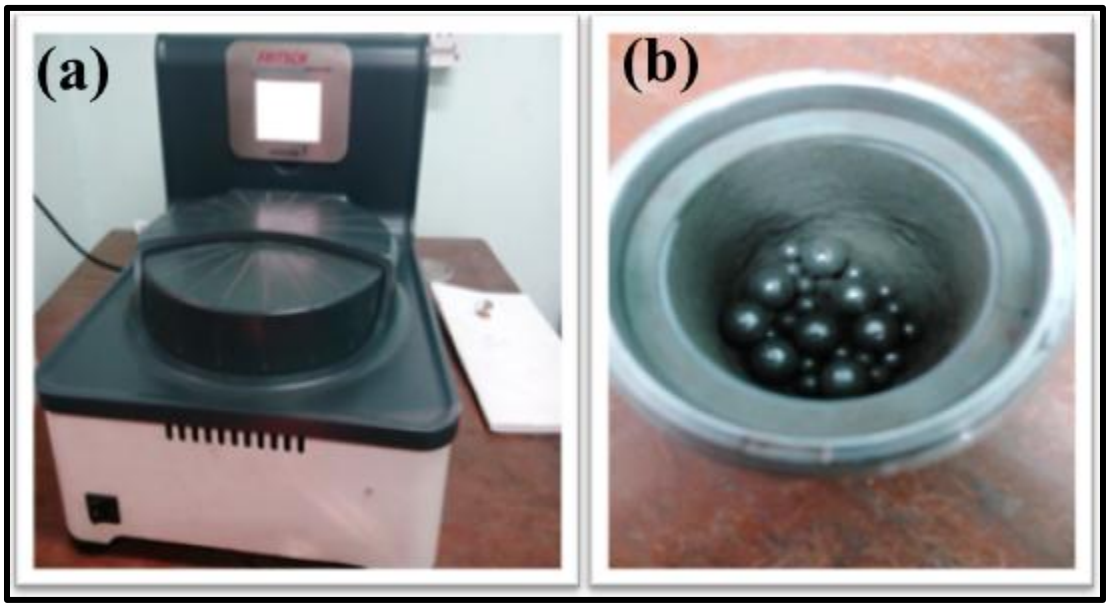

Figure 3.2: Planetary ball mill

3.1.3. Pelletizer

The hydraulic pressure provided by a pelletizer (figure 3.3) to generate the prepared pellets with a pressure (1 GPa). The dice that was utilized a 12 mm diameter. These pellets are additionally employed to investigate the electrical analysis. For each generation of pellet, the pressure was maintained for one minute. Polyvinyl alcohol was utilised to create the pellets more compact. To get removal the PVA or make the pellets more compact, the pellets was subsequently once more annealed at temperature (1000^0C). These pellets thickness was determined by using the slide callipers.

Figure 3.3: Pelletizer

3.1.3.1. Pellets preparation

When 20 ml Deionized (DI) water and PVA (0.5 g) powder (Merck) were heated to 100 ^{0}C, PVOH was produced. In order to create a pellet with a 12 mm in diameter, 0.5 g of the material was combined via PVA and then pressed it into pelletizer. Then, for only a maximum of four hours, these pellets are heated to temperature of 1000 ^{0}C in order to allow the PVA to evaporate. After that, each pellet is cooled by air and then copper wire is used to make contacts of the pellets with a conductive silver paste (Alfa Aesar ™ 4407518). The image of pellet preparation is provided figure in 3.4.

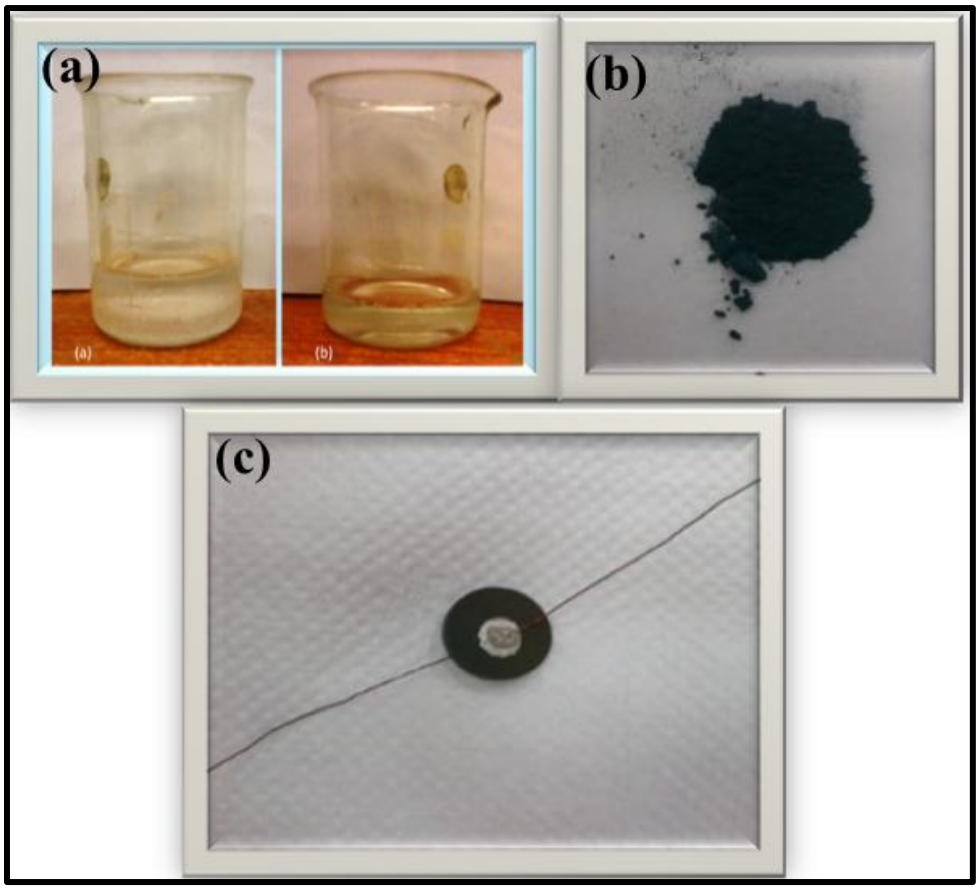

Figure 3.4: (a) PVA with DI water (b) Sample (c) pellet

3.2. X-ray diffractometer (XRD):

The prepared materials are subjected to X-ray diffraction (XRD) survey in way to extract the crystallography data. By using the Bruker D8 Advanced apparatus, polycrystalline compounds are subjected to both quantitative as well as qualitative phase evaluations. In which an array of crystal planes with a specified 2θ values might be found inside the XRD analysis. The scanning speed is set to 1 s/step, and also the scanning pattern is selectable in steps of 2θ that range (20°-80°) including an intervals of 0.02°/step. Ge (022) monochromator created Cu K_α (λ = 1.54 Å) performed with 40 mA and 40 kV. The diffraction may be employed to examine the lattice space associated to a specific hkl plane applying Bragg's expression [1] with first ordered diffract:

$$2d_{hkl} \sin\theta = n\lambda \qquad (3.1)$$

Where d_{hkl} represents the inter-planar spacing, n denotes order of diffraction, λ and θ implies electron wavelength and glancing angle. The XRD is displayed in figure 3.5.

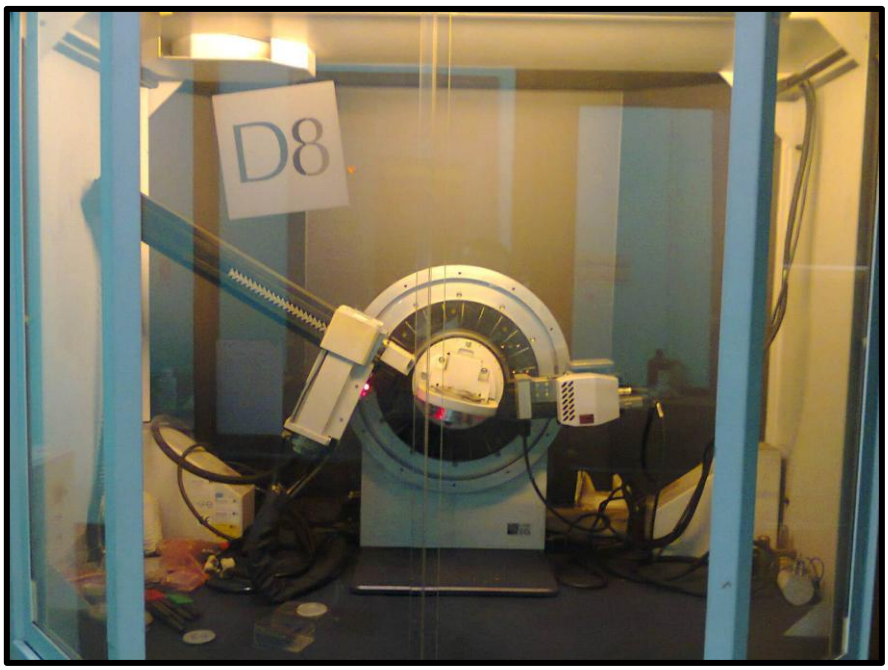

Figure 3.5: X-ray diffractometer

3.3. X-ray photoelectron spectrometer (XPS):

To examine the material clarity, oxidation states, including compositional parameters, X-ray photoelectron spectrometer (XPS, SPECS and Germany) was being used. The basic idea behind XPS is that a material is exposed to a beam of X-ray, resulting in photoelectron emission across the material. The figure 3.6 exhibits schematic view of such an electron emission procedure.

Figure 3.6: X-ray photoelectron spectrometer

Because the intensity of such an incoming x-ray is already known, the following expression can be employed to correlate the typical binding energy to the estimated kinetic energy (K.E) of the fundamental photoelectrons:

$$E_b = h\vartheta - E_k \qquad 3.2$$

Where $h\vartheta$ stands for incident X-ray energy and E_k for K.E of the photoelectrons [2]. XPS might be the most accurate method for classifying surface elements because different elements have distinct binding energy sets. Additionally, it is possible to measure the material elemental concentrations by the determining so-called binding energies under area of the curves. These minute variations in binding energies reveal specific details about just the materials relatively brief chemistry and also chemical states. During material analysis on SPECS, a monochromatic sources of light (MgK_α or AlK_α) X-ray working at 17 mA & 10 kV was exploited. The hemispheric energy analysers (HAS 3500) was also utilized. Photoelectrons were employed to stimulate the electrode current. The systems remaining pressure is higher than that of 10^{-9} mbar. The diameter (165 mm) and also 8-channel detectors promise good spectrum resolution with superb sensitivities. Because the amount of released photoelectrons changes with the K.E, it really is possible to quantify the K.E distribution of released photoelectrons and also record the spectra. In figure 3.6, the X-ray photoelectron spectra are depicted.

3.4. Morphological analysis:

3.4.1. Field emission scanning electron microscope (FESEM)

An essential method for obtaining an image of the samples surface is utilizing a field emission scanning electron microscopy (FESEM). With energies ranging so many 100 to 50 K eV, the release of electrons through field emission guns. The beam was focused and also accelerated up by various deflecting coils after it has been created from gun. At last, the materials surface is struck by the collimating, which then reacts with it. As a response, the material emits electrons and also photons. The transfer of energy between the both sample and also e-beam causes electromagnetic energy radiation to be emitted, secondary electrons to be emitted through inelastic-

Figure 3.7: Field emission scanning electron microscope (FESEM) with EDX

collisions, large energy electrons to also be reflected via electromagnetic scattering, and all of these incidents could be detected by a particular detector and transformed into such the signal containing material information like composition, surface morphology as well as additional qualities. The signals produced by FESEM include backscattered electrons, secondary electrons, distinctive X-rays, light (cathodoluminescence), transmission electrons and materials current. The material under investigation ought to be conducting with traditional images in FESEM since that eliminates static charges from accumulating up on its surface and therefore is consistent in vacuum. Prior to imaging, a very thick (gold or platinum) treatment is applied to non-conducting materials using sputtering or evaporating techniques. The FESEM device (HITACHI-S4800) was employed to determine both the thickness of the films and also the surface morphologies. The FESEM resolution is very near to 5 nm, and thus the magnification ranges from (30 to 300K) X. The device has two imaging modes that it can use, including secondary or backscattered electrons. The camera has a focal length (50mm) and using a 35mm lens reflex (CSI 3 and MP 35051). The final figure may reveal specifics about the consistency and thickness of materials. Figure 3.7 displays the instrument of FESEM.

3.5. Compositional analysis:

3.5.1. Energy dispersive X-ray (EDX)

This method is depends on particular peaks of X-ray that happen whenever a higher energy of electron gun comes into contact with the material. Every element emits particular X-rays, typically may be utilised to detect the elements existence in the area being examined. It’s really

possible to calculate relative concentrations of every element contained inside the material by comparing the respective intensities of such X-ray signals. Typically, it is impossible to recognize chemical elements having atomic numbers smaller than carbon (Z = 6). EDX (HITACHI-S4800) is employed to analyse the materials composition, which operating at 15,000 V. The device is able of being identified everything from Li (3) to U (92). It's linked to the FESEM (Hitachi S-4800). The EDX is presented in figure 3.7.

3.5.2. Transmission electron microscope (TEM)

A characterizing device is called the transmission electron microscope (TEM) is being utilized to comprehensively analyze the crystalline structure and also microstructure of samples using image processing or diffraction methods. Additionally, the transmission electron microscope (TEM) also has a imaging method called high-resolution (HR)-TEM, which may produce an image of the materials crystalline structure at atomic scale that are more specific and accurate. Through the various electron distributions through numerous holes created by electron gun, the material is illuminated by the lens. It may be said that in such lenses, objective lens creates the diffraction pattern over background focal plane that is the Fourier transformation of a wave function ($\psi(r).n$) at object surface [3]. The picture can then be focused just on fluorescent screen once the beam of collimated light has passed through into the material. Lastly, the CCD camera, directly exposure of a photography emulsion, or other such technology records the images digitally. The electrostatic field accelerates a beam of electron produced by that of electron gun. Typically, (150-250 kV) is employed to transmit a beam of electron in HRTEM. The material might be traversed by the beam in this method. Its initial image created mostly by objective lens becomes 25 times larger than the actual image, and it continues to be magnified by each succeeding lens to final image, which becomes 106 times longer than final image. The material experiences individual interactions from

each particle inside this electron beam. The strong atomic potential of such materials atomic-nuclei attracts the beam, which then channel along of atomic columns lattice as it moves across material. The Bragg diffraction with the interaction of electron waves across several atomic columns occurs simultaneously. It is possible to replicate microscope imaging more precisely by using the recognized principles of physics on the electron scattering or imaging. The two imaging methods of bright field and also dark field figures are frequently utilized in TEM. For bright field figures, where its diffracted electrons being controlled by such a diaphragm, an image can create through transmitting electrons without even any diffraction. Contrarily, the diffraction beam is applied for imaging inside this dark field figures mode.

The crystalline structure and also microstructure of the materials that were examined by using a transmission electron microscope (TEM: JEOL, JEM-2100). This device features three separate condensers, which may produce high probed current about any particular probed size, improving analytics or diffraction capability. This device has several pumping capabilities, namely dry or turbo pumps in laboratory circumstances. The utilized of rotary or oil-based pumps remains restricted. Although the equipment is supposed to have a resolution near 0.1 nm, typical observations demonstrate an average resolution (8-10 Å). This model magnification range of (50 -1500 K) X, and its acceleration voltage ranges from 80 to 200 kV. The dispersion of material was dropped onto such a copper mesh that had been coated with carbon, and also the solvent was then allowed to evaporate to create a TEM sample. The HRTEM image provided in figure 3.8.

Figure 3.8: Transmission electron microscope (TEM)

3.6. Optical analysis:

3.6.1. UV-visible spectroscopy (UV-VIS)

The spectrophotometer utilized in the UV-visible range is known as a UV-visible NIR-spectrophotometer. The spectrophotometer represents a technique for examining liquids, solids and gases by exploiting radiating energy within the far UV or near-UV, visible, or near infrared

region of an electromagnetic spectrum. Consequently, the electromagnetic radiations preset UV, Vis and also NIR wavelengths are employed. When using the apparatus, a light beam was pointed in through the material, and also the light wavelength arrived the detector is then measured. The intensity was associated with the number, concentrations of components and also average number, while the wavelength reveals important the details about chemical structural properties. The evaluation information may be presented using energy transmittance, reflectance or absorption in wavelength range (160 to 3500) mm. To obtain the reflectance spectroscopy and estimate the direct band gap, utilized a UV-Vis (Shimadzu UV- 3600) spectrophotometer. The obtained measurements for such an unknown compounds always are calibrated against the consequence of a well-known standard sample ($BaSO_4$). The UV-Vis spectroscopy demonstrates in figure 3.9.

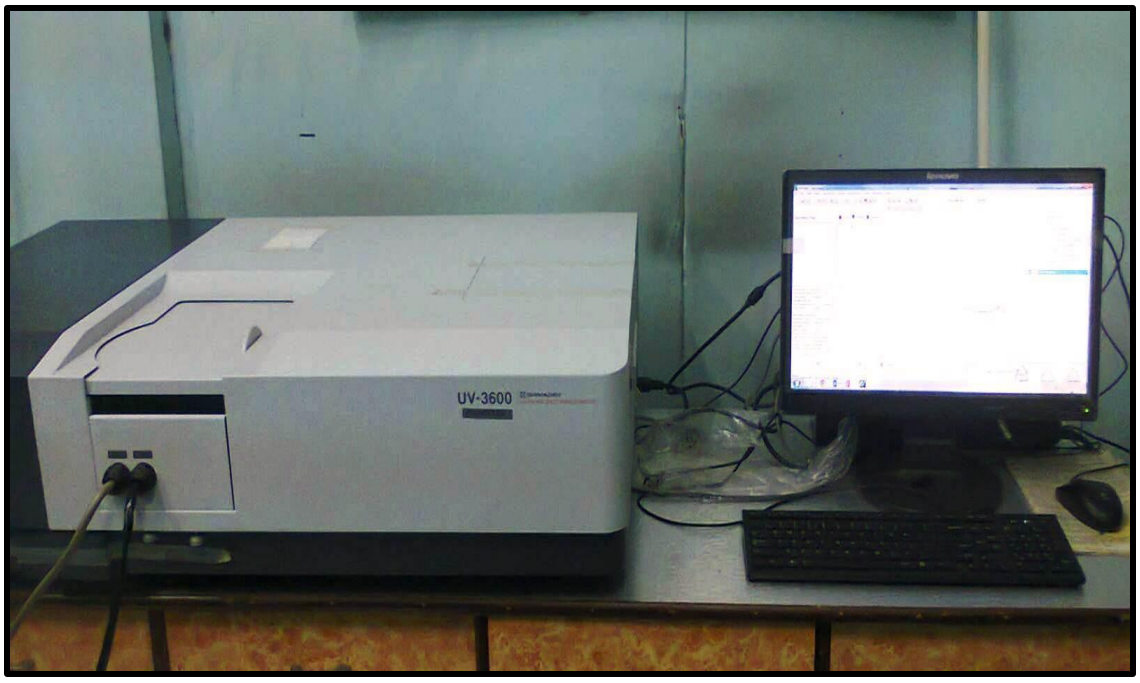

Figure 3.9: UV-visible spectroscopy (UV-VIS)

3.7. Electrical studies:

3.7.1. Impedance analyzers

The behaviour of samples under steady state condition including the external perturbation was investigated using this electrochemical technique. The imaginary and real component of current in response toward an oscillating voltage is typically explored across a broad range of frequency, and therefore is typically described in terms like an appropriate LCR (L: Inductor; C: Capacitor; R: Resistor) circuit. The methodology enables for the looking into the transport dynamics at the electrolyte or electrode interfaces.

A precision impedance (Agilent 4294A) analyzer was used in this investigation to measure the frequency dependence dielectric spectroscopy. The permitted DC voltage and also current ranges (±40 V & ±100 mA). The frequency could be sweeps across a broad range from 40 Hz to 110 MHz. The precision analyzer is presented in figure 3.10.

Figure 3.10: The impedance analyzer

3.7.2. LCR Meter

The LCR HIOKI (3522-50) Hi-TESTER is utilized to obtain the current-voltage (I - V) characteristics. In small-scale dielectric measurement tool, this is most frequently employed. The touch panel serves also as user interface for this impedance analyzer. With high resolution, the measuring frequency could be adjusted at 10^5 Hz. This instrument allows for simultaneous presentation of R, L and C on the screen in addition to impedance with phase angle. The LCR HIOKI meter is displayed in figure 3.11.

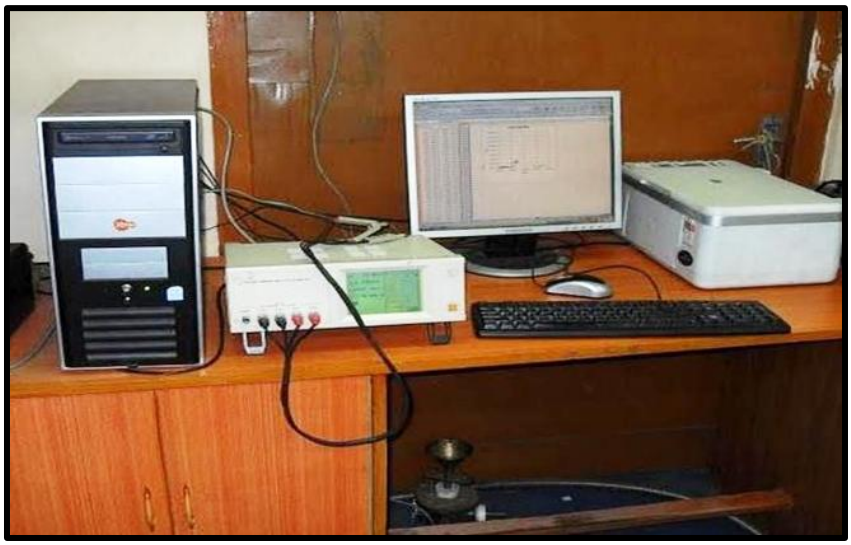

Figure 3.11: The LCR meter

3.7.3. Low temperature measurement devices

This gadget may be used as a measurement different electrical characteristic over a large temperature range (10-300K). The devices are composed of various components including vacuum pump, external compressor or pump, digital 4-digit pirani gauge, compressor along with cryostat, LCR HIOKI (3522-50) Hi-TESTER and also temperature controller. The experimental

arranged for measuring electrical characteristics at low temperature is depicted in figure 3.12. Before turning on the cryostat or compressor, an additional pump or compressor is installed for freezing outside the system. The outer pump or compressors perform the initial level of chilling, and also cryostat compressor performs the secondary level of chilling. Utilizing vacuum pump or pirani gauge, that measures internal pressure, the equipment should be thoroughly vacuum prior decreasing the temperature. To manage the temperature, the controller was utilized, which may be adjusted according to the needs of the measurement equipment.

Figure 3.12: Low temperature measurement devices

3.7.4. Hall analysis

To use a consistent magnetic field of 0.15 T, the Hall measuring system employs a four-probe arrangement (Van der Pauw) is displayed in figure 3.13. As it provides information on carrier density, resistivity, carrier mobility and also carriers type, the Hall effects evaluation method is frequently used to investigate semiconductor materials. A conductor can generate the electric field perpendicular to magnetic field or current direction, whenever the magnetic field can provide perpendicular toward the current direction. The produced voltage is referred to as Hall voltage and also the phenomenon is termed Hall Effect. Van der Pauw conformal maps provides as such theoretical basis for Hall measuring analysis for materials with irregular shapes. The specimen should have point contacts that are symmetrically placed surrounding its edge, being evenly thin, and not include any isolated holes. Hall Effect evaluations are straightforward to understand for materials that have been consistently doped. Using van der Paw geometries, it was possible to calculate hall coefficient of the carrier charges.

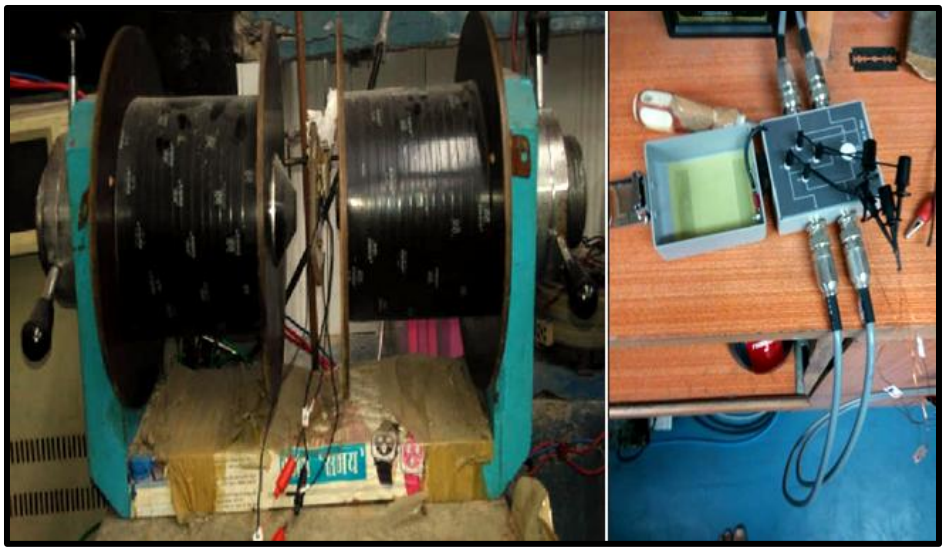

Figure 3.13: Hall analysis set-up

3.8. References:

1. E. Cook, R. Fong, J. Horrocks, D. Wilkinson, and R. Speller, Applied Radiation and Isotopes, 2007, 65, 959-967.

2. P. Van der Heide, X-Ray photoelectron spectroscopy: An Introduction to Principles and Practices, John Wiley & Sons, 2011.

3. Cowley, J. M (1995). *Diffraction physics*. Elsevier Science B. V. ISBN 978-0-444-82218-5.

4. Simultaneously cationic-anionic substitution in *p*-$CuCrO_2$ for transparent and superior transport

Chapter 4

4.1. Introduction:

The expansion of high-performance TCOs is inherent to many devices from solar cells [1] to transparent electronics (TEs) [2] as they are endowed with the co-existence of high electrical conductivity and transparency to visible light [3]. TCO materials in thin film form are particularly demanding for providing electrical contact without impeding the incoming flux of visual light to the devices, to transparent active components integrable in windows [4, 5]. Due to achieving two mutually exclusive characteristics of higher electrical conduction and optical transparency, broad energy gap oxides must be doped with significant amount of desired charge carriers. Unlike *n*-TCOs, *p*-TCOs have not been highly commercialized; barring many critical technological applications and creating the transport bottleneck [6-8]. The basic idea to the difficulty of engineering highly conductive *p*-TCOs is the localized nature of the valence band in most oxides resulting in flat band and associated large hole effective mass [9]. The area of *p*-TCOs have received most of its impulse more than a decade ago by the pioneering work of Kawazoe et al. [10] presenting $CuAlO_2$ with encouraging hole conductivity and also optical transparency in visible light. The base of mobile holes was explained considering significant hybridization of the oxygen orbitals with $3d^{10}$ configuration of the Cu^{1+} closed shell. This finding led to the outline of a designing rule for *p*-TCOs requiring the presence of Cu^{1+} for dispersion of valence band. Triggered by this study, a large amount of Cu-based materials were designed including delafossites ($CuCrO_2$, $SrCu_2O_2$) [11, 12] and Cu-based oxychalcogenides 13]. In very recent, the question remains open

whether alternative schemes could lead to *p*-TCOs with superior optoelectronic properties. Currently, Arca et al. have identified another potential *p*-TCO Cr_2O_3 exhibiting high figure of merit and transparency upon magnesium and nitrogen co-doping [14]. Furthermore, electronic structure and defect chemistry of $CuCrO_2$ has been studied extensively by G. W. Watson's group regarding the potential application of these important *p*-TCOs [15, 16]. One of such attempts has led us to the newly developed doping scheme at O-site by chalcogen elements with promising band dispersion and transport properties [17] along with subsequent follow ups by other research groups [18, 19].

When numerous applications of TCOs will undoubtedly come from thin films, much of the fundamental chemistry and physics may more easily be studied in the bulk form of the material. In this work, prototype *p*-TCO $CuCrO_2$ is taken as host matrix and also both cation and anion doping are performed simultaneously in order to improve the electrical conductivity while maintaining the transparency in visible range.

4.2. Experimental details:

4.2.1. Materials and methods

Bulk powder of $CuCrO_2$ is prepared from stoichiometric mixture of CuO and Cr_2O_3 (Sigma-Aldrich); MgO (Sigma-Aldrich) and CH_4N_2S (Merck) are used to dope Mg and S at Cr and O-site respectively for $CuCr_{1-x}Mg_xO_{1-y}S_y$ preparation. Precursors are thoroughly ground together and subsequently sintered at 1150°C for 15 h and quenched in air. The amount of sulphur taken was

thrice than that of required to compensate for the thermal evaporation from the matrix [17]. From here on, the samples would simply be labelled as $CuCrO_2$, $CuCrO_{1.9}S_{0.1}$, $CuCr_{0.95}Mg_{0.05}O_2$, $CuCr_{0.97}Mg_{0.03}O_{1.94}S_{0.06}$ and $CuCr_{0.95}Mg_{0.05}O_{1.9}S_{0.1}$ according to their cationic and anionic doping percentages.

4.2.2. Characterizations

The crystallographic phase confirmation of prepared powders is determined by X-ray diffraction (Bruker D8 Advance) with a Cu K_α X-ray source (λ=1.54 Å) at 40 kV, 40 mA. The scanning mode is selected in 2θ ranging from 20^0 to 80^0 with an interval of 0.02^0/step and the scanning rate is 1sec/step. Samples are spread on a quartz platform. Refinement of $CuCr_{0.95}Mg_{0.05}O_{1.9}S_{0.1}$ XRD pattern is performed by Rietveld method by using FULLPROF programme. The schematics of side and top view of refined crystal structure (2x2x2) are created by DIAMOND programme using structural parameters as obtained from Rietveld refinement. The bulk elemental composition percentage are analysed by energy dispersive X-ray spectroscopy [Hitachi S4800 FESEM (15 kV)]. The diffuse reflectance (DR) spectra are collected by Shimadzu 3600 spectrophotometer. Room temperature current-voltage profile and the temperature dependent (80-300k) DC electrical conductivity (σ_{dc}) measurements are carried out in two probe configuration using an LCR Hi-Tester (Hioki 3522-50) and liquid nitrogen assisted Keithley 4200 semiconductor characterisation system. The conduction at room temperature is confirmed to be *p*-type by Hall measurement (Van der Pauw method). Frequency dispersion (40 Hz – 110 MHz) of admittance properties of as prepared pellets is observed by Agilent 4294A precision impedance analyser with variable dc external bias.

4.3. Results and discussions:

4.3.1. Structural properties

The crystallographic phase, as determined by X-ray diffraction is the same for all five samples without detection of any additional impurity peaks (figure 4.1a) and only the delafossite phase with rhombohedral symmetry (PDF number 74-0983, space group $R\bar{3}m$ 166) is observed. Unit cell parameters (*a* and *c*) of all materials are obtained from Rietveld refinement and crystalline size (D) and strain (η) are calculated from Williamson-Hall plot; which are shown in table 4.1. It can be noted that in-plane lattice parameter (*a*) remains same upon sulphur doping while magnesium doping increases it. Moreover, *c* decreases for cationic, anionic and co-doping. As the Mg^{2+} radius (86 pm) is larger than Cr^{3+} (75.5 pm), *a* increases due to cationic substitution. The decrease in the *c*-axis can be attributed to the reorientation of bond lengths and bond angles of CrO_6 octahedra which were discussed in our previous work [14]. Bulk compositional percentage of $CuCr_{0.95}Mg_{0.05}O_{1.9}S_{0.1}$ is analysed by energy dispersive X-ray spectroscopy (EDX). Figure 4.1e reveals the global atomic percentages of Mg and S in the desired $CuCr_{0.95}Mg_{0.05}O_{1.9}S_{0.1}$ are (3.12 ± 0.95) and (0.25 ± 0.52) % for (36.56 ± 3.11) % Cr-site and (30.73 ± 12.52) % O-site respectively. Calculated XRD pattern of $CuCr_{0.95}Mg_{0.05}O_{1.9}S_{0.1}$ is presented with the superposition of experimental data for comparison (figure 4.1b). For the confirmation of simultaneous cationic-anionic doping, Wyckoff symmetry of S and Mg are initially considered to be identical with that of O and Cr respectively. However, the fractional coordinates of O-site displace slightly due to the incorporation of S as predicted by density functional theory. For refinement, a total of 48 parameters are refined (30 structural parameters and 18 profile parameters) and pseudo-voigt function is used as peak shape function. Final goodness of fitting ($\chi^2 = R_{wp}^2/R_{exp}^2$) converges to 4.32, reasonable considering various

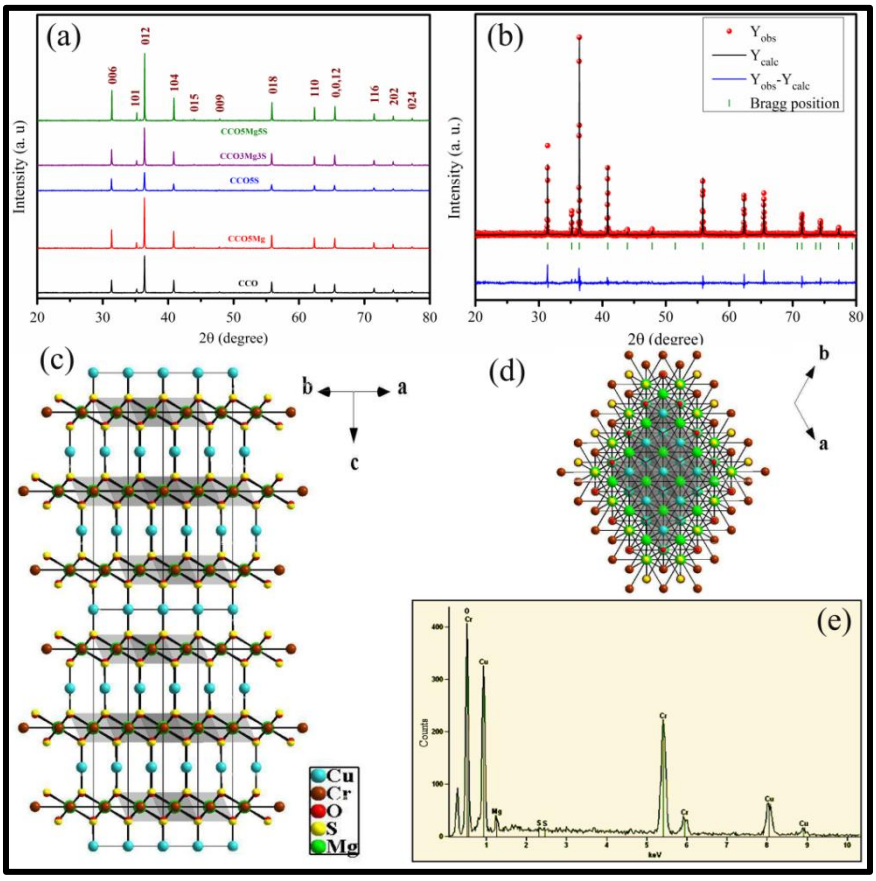

Figure 4.1: (a) X-ray powder diffraction patterns of the synthesized materials, exhibiting rhombohedral symmetry (PDF number 74-0983, space group $R\bar{3}m$, 166). (b) Rietveld refinement of $CuCr_{0.95}Mg_{0.05}O_{1.9}S_{0.1}$ sample considering the chemical formula $CuCr_{0.9701}O_{0.9867}S_{0.0061}Mg_{0.0302}$ in accordance with the result of energy dispersive X-ray spectrum. The black curve is the best fit from the Rietveld refinement using FULLPROF programme. The vertical lines indicate the positions of Bragg peaks and the blue curve represents the difference between the experimental and calculated intensities. (c) and (d) are schematics of side and top view respectively of the refined crystal structure (2x2x2). (e) Elemental distribution as obtained by energy dispersive X-ray analysis for $CuCr_{0.95}Mg_{0.05}O_{1.9}S_{0.1}$.

Table 4.1: Refined unit cell parameters, crystalline size and strain for all the synthesized materials obtained from Rietveld refinement and Williamson-Hall plot respectively.

Materials	Lattice parameter a (Å)	Lattice parameter c (Å)	Cell Volume V ($Å^3$)	Crystalline Size D (nm)	Effective lattice strain η (%)
$CuCrO_2$	2.9729	17.1178	131.02	80.64±4.15	0.011±0.004
$CuCr_{0.95}Mg_{0.05}O_2$	2.9755	17.1071	131.17	89.44±4.52	0.007±0.004
$CuCrO_{1.9}S_{0.1}$	2.9729	17.1008	130.89	73.10±11.36	0.017±0.016
$CuCr_{0.97}Mg_{0.03}O_{1.94}S_{0.06}$	2.9749	17.1071	131.12	88.30±5.77	0.007±0.004
$CuCr_{0.95}Mg_{0.05}O_{1.9}S_{0.1}$	2.9768	17.0970	131.20	129.49±5.71	0.015±0.002

vacancy and interstitial defects due to polycrystallinity. Lattice parameters are refined to $a = b =$ 2.9768 Å and c = 17.0970 Å, associated with the fitted profile. The decrease in the sulphur concentration (0.6 %) from the desired doping level (5 %) can be explained considering high thermal evaporation tendency of sulphur from solid solution at 1150 ºC. Upon realization of the refined crystal structure (2x2x2), it can be observed that Cr atoms are connected to the coordination sphere associated to Mg atoms and S replacing O partially with slightly different Wyckoff symmetry (figure 4.1c); while keeping the overall rhombohedral symmetry of the crystal structure intact (figure 4.1d). Unlike the previous report, here we have demonstrated that near perfect doping of sulphur at O-site do not necessarily lead the crystal to polytypism.

4.3.2. Optical properties

The diffuse reflectance (DR) spectra of the powders are measured against a reference standard $BaSO_4$ compound. The Kubelka-Munk (K-M) theory [20] is then used to obtain the band gap of the prepared samples from the DR spectra. The ratio of the light scattered (R_{inf}) from a thick absorbing layer of sample (R_{sample}) to the ideal non-absorbing reference sample ($R_{reference}$) is measured as a function of wavelength (220-1500 nm) and the K-M function is computed by the relation:

$$F(R_{inf}) = \frac{(1-R_{inf})^2}{2R_{inf}} \quad , \qquad (1)$$

From the plot of $[F(R_{inf})h\nu]^2$ versus $h\nu$ (Figure 4.2), the value of band gap (E_g) is obtained by extrapolating the linear slope to$[F(R_{inf})h\nu]^2 = 0$. The values of band gap obtained for all the synthesized powders are found to be well within the 'transparent' region having wide band gaps (3.52 eV for $CuCrO_2$, 3.45 eV for $CuCr_{0.95}Mg_{0.05}O_2$, 3.50 eV for $CuCrO_{1.9}S_{0.1}$ and 3.48 eV for $CuCr_{0.95}Mg_{0.05}O_{1.9}S_{0.1}$) and are in good agreement with the optical gap calculated by Chen *et al.* for post-annealing derived $CuCrO_2$ thin films (3.55 eV) [21].

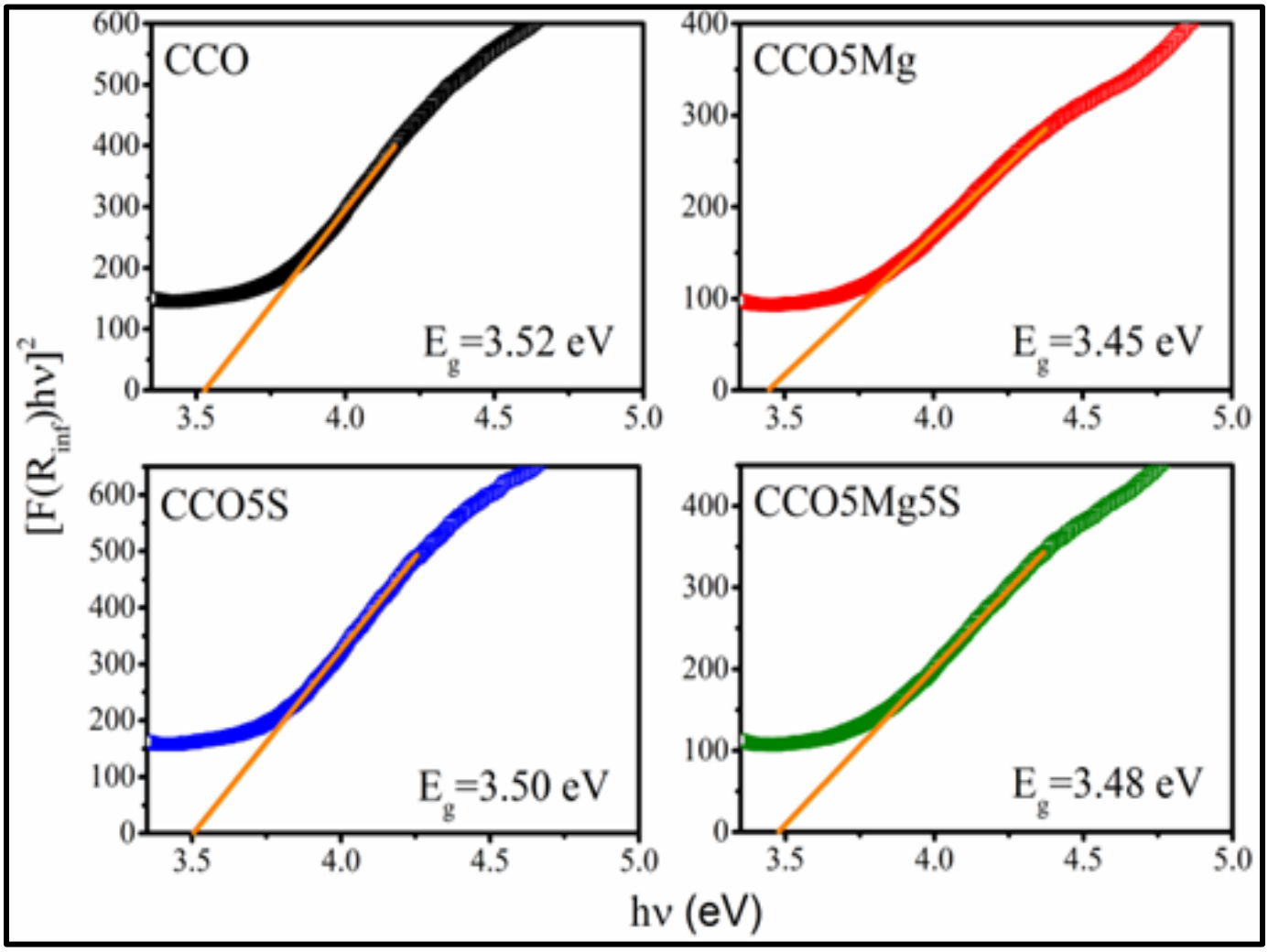

Figure 4.2: Band gap calculations of prepared powders from diffuse reflectance spectra using Kubelka-Munk function.

4.3.3. Electrical properties

We have studied the temperature dependent dc electrical conductivity (σ_{dc}) for $CuCr_{0.95}Mg_{0.05}O_2$ and $CuCr_{0.95}Mg_{0.05}O_{1.9}S_{0.1}$ over a temperature range 80 – 300 K (Figure 4.3a). The results conclude that co-doped $CuCrO_2$ exhibits twice as large conductivity than its Mg doped counterpart at ambient temperature. The value of σ_{dc} is found to be 0.045 S-cm^{-1} and 0.022 S-cm^{-1} at 300 K for $CuCr_{0.95}Mg_{0.05}O_{1.9}S_{0.1}$ and $CuCr_{0.95}Mg_{0.05}O_2$ respectively. The conduction is confirmed to be *p*-type by Van der Pauw method with other relevant parameters shown in table 4.2. The plot of lnσ versus 1/T for Mg doped $CucrO_2$ assumes fairly linear fit across DE region (142 - 300 K); and for co-doped $CuCrO_2$ across AB (145 - 300 K) implying thermally activated conduction with DC conductivity (σ_{dc}) obeying the following relation:

$$\sigma = \sigma_0 \, e^{-E_a/k_B T} \, , \qquad (2)$$

Where σ_0 is a constant, E_a is the activation energy and k_B is the Boltzmann's constant. E_a for DE and AB segments are calculated to be 54.7 meV and 68 meV respectively. Calculated E_a is in close agreement with the result obtained by Han et al. for Mg doped $CuCrO_2$ thin films (55 meV) [22]. Carrier mobility (μ_{dc}) is observed to be greater in $CuCr_{0.95}Mg_{0.05}O_2$ (61.66 cm^{2}V^{-1}S^{-1}) than $CuCr_{0.95}Mg_{0.05}O_{1.9}S_{0.1}$ (16.26 cm^{2}V^{-1}S^{-1}) resulting in higher activation energy for co-doped material in spite of having greater conductivity. However, no linear fit can be found across the low temperature range (80 – 140 K) for BC and EF region as shown in the inset. For that, these segments are fitted assuming variable range hopping (VRH) mechanism for conduction, where the temperature dependence of σ_{dc} can be described by the following relation [23, 24] as:

$$\sigma = \sigma_0 \exp\left[-\left(\frac{T_0}{T}\right)^{1/4}\right], \qquad (3)$$

Where T_0 is the characteristic Mott temperature and σ_0 is the pre-exponential factor. Here, $N(E_F)$ representing the density of localized states at the Fermi level E_F can be calculated by using the following expression:

$$N(E_F) = 2.12 \times 10^9 \sigma_0^3 T_0^{1/2}\ cm^{-3} eV^{-1}, \qquad (4)$$

and are found to be 1.9×10^{25} $cm^{-3}eV^{-1}$ and 4.19×10^{21} $cm^{-3}eV^{-1}$ for $CuCr_{0.95}Mg_{0.05}O_{1.9}S_{0.1}$ and $CuCr_{0.95}Mg_{0.05}O_2$ respectively.

Clearly, we can observe a 'crossover' between BC and EF segments (80 – 140 K) which is inducing an interesting transport profile in terms of low (< 140 K) and high (> 140 K) temperature behaviour of these two materials. It dictates that more conductive $CuCr_{0.95}Mg_{0.05}O_2$ in lower temperature becomes less conductive in comparison to $CuCr_{0.95}Mg_{0.05}O_{1.9}S_{0.1}$ above 140 K. For our materials, this crossover temperature (140 K) from VRH to activated conduction is observed to be much lower than that of reported by Li et al. (206±10 K) for 6% Mg doped $CuCrO_2$ thin films [25]. We attribute this difference to the moderate carrier concentration of 2.23×10^{15} cm^{-3} which also results in high hole mobility (61.66 $cm^2V^{-1}s^{-1}$) due to negligible ionized impurity scattering. It is important to note that calculated $N(E_F)$ is almost 10^4 order higher upon co-doping in comparison to Mg doped $CuCrO_2$. It is expected that much higher density of states due to sulphur induced anti-bonding, [17] is generating a surge of carriers with increase in temperature. Existence of ten times more carrier concentration in co-doped material (1.73×10^{16} cm^{-3}) is also in agreement with Van der Pauw measurement. Now, for polycrystalline powder samples, excess amount of carriers get scattered from various defect centres present in it [17]. That's why the magnitude of σ_{dc} is larger for $CuCr_{0.95}Mg_{0.05}O_{1.9}S_{0.1}$ but with reduced μ_{dc} (16.26 $cm^2V^{-1}s^{-1}$) than $CuCr_{0.95}Mg_{0.05}O_2$ due to the

increase in impurity scattering. Combining the results of DC conductivity along with our previous findings [17], it can be concluded that concentration of delocalized holes are higher in co-doped

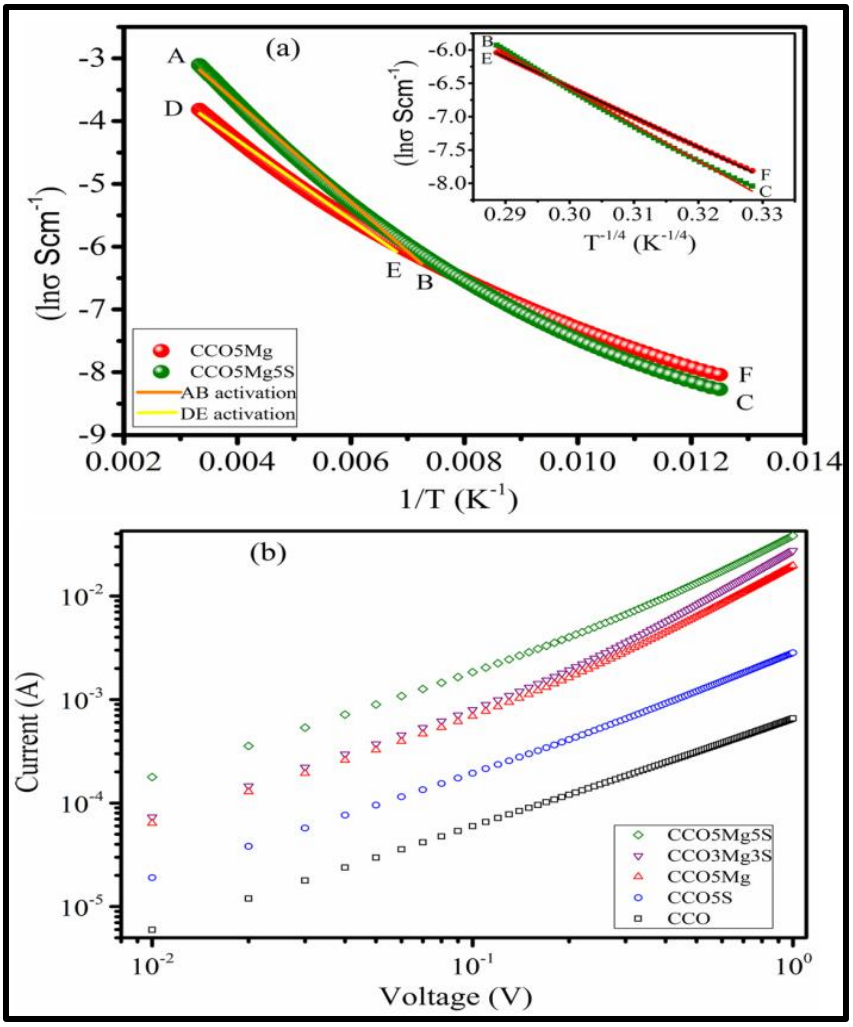

Figure 4.3: (a) Temperature dependent DC conductivity for 80 – 300 K for $CuCr_{0.95}Mg_{0.05}O_2$ and $CuCr_{0.95}Mg_{0.05}O_{1.9}S_{0.1}$. AB, and DE are segments of the experimental data fitted assuming activated conduction and segment BC and EF showing the low temperature conductivity of $CuCr_{0.95}Mg_{0.05}O_2$ fitted considering variable range hopping mechanism (inset). (b) log – log representation of current – voltage for the prepared materials.

Table 4.2: Transport parameters at 300 K as calculated from Arrhenius and Hall measurements.

Sample	σ_{dc} (S/cm)	ρ_{dc} (Ω-cm)	R_H (cm^3C^{-1})	n (cm^{-3})	μ_{dc} ($cm^2V^{-1}s^{-1}$)
$CuCr_{0.95}Mg_{0.05}O_2$	0.022	45.45	2.8×10^3	2.23×10^{15}	61.66
$CuCr_{0.95}Mg_{0.05}O_{1.9}S_{0.1}$	0.045	22.23	360	1.73×10^{16}	16.26

$CuCrO_2$ compared to its Mg doped counterpart with more dispersed valence band. The current – voltage profiles of as prepared materials (Figure 4.3b) is in harmony with that of conductivity as the current increases more than ten times upon co-doping in comparison to the undoped $CuCrO_2$.

It should be mentioned here that high carrier concentration and low mobility is a typical feature of small polaron hopping (SPH) [26] and is rather considered to be a drawback for overcoming transport bottleneck in *p*-type TCO. The contemporary TCO community is striving to identify potential *p*-TCOs with high hole mobility [27] and the most effective way to realize this goal is by dispersion of O 2*p* valence band. Recently, Bhatia et al. have reported hole mobility in excess of 30 cm^2/Vs with a carrier concentration of ~ 10^{14} cm^{-3} for bismuth based transparent *p*-type oxide [28] and Caraveo-Frescas et al. have reported hole mobility of 18.71 cm^2/Vs with a carrier concentration ranging 4.83×10^{16} cm^{-3} to 3.33×10^{17} cm^{-3} for *p*-type tin monoxide films [29].

4.3.4. Admittance spectroscopy

To investigate the admittance spectroscopy of the materials, the as-synthesized powders are cold pressed into pellet by applying a pressure of 1 GPa. Typically, by plotting the negative differential susceptance ($-\Delta B$) as a function of frequency, a characteristic frequency f_r is obtained at which a maximum of $-\Delta B$ occurs. This is correlated with the carrier average transit time ($f_r = 0.56/\tau_{dc}$) [30] and as we can see from Figure 4.4a, no maximum of $-\Delta B$ is present for $CuCrO_2$ and $CuCrO_{1.9}S_{0.1}$ within the observed frequency range. Gradual shift of f_r to the low frequency is observed for $CuCr_{0.95}Mg_{0.05}O_2$ (8.293 MHz), $CuCr_{0.97}Mg_{0.03}O_{1.94}S_{0.06}$ (4.064 MHz) and $CuCr_{0.95}Mg_{0.05}O_{1.9}S_{0.1}$ (3.83 MHz) respectively and can be attributed to the increasing τ_{dc} of 67.5 ns for $CuCr_{0.95}Mg_{0.05}O_2$, 0.14 μs for $CuCr_{0.97}Mg_{0.03}O_{1.94}S_{0.06}$ and 0.15 μs for $CuCr_{0.95}Mg_{0.05}O_{1.9}S_{0.1}$ at 3 volt external applied bias. In Figure 4.4b, clear downshift of the admittance maxima (A_{max}) is observed in the frequency dispersion (8.801 MHz for $CuCr_{0.95}Mg_{0.05}O_2$, 5.155 MHz for $CuCr_{0.97}Mg_{0.03}O_{1.94}S_{0.06}$ and 4.313 MHz for $CuCr_{0.95}Mg_{0.05}O_{1.9}S_{0.1}$) upon co-doping. Again, no maxima are observed in admittance for $CuCrO_2$ and $CuCrO_{1.9}S_{0.1}$ within the observed frequency range. As admittance is defined as inverse of impedance (Y = 1/Z), we stress that hole concentration is increasing upon simultaneous cationic-anionic doping and reaches the value of 0.8 S at A_{max} for $CuCr_{0.95}Mg_{0.05}O_{1.9}S_{0.1}$. In this case, A_{max} at lower frequency is indicating a shorter screening length; thereby cementing the supposition that reduced hole mobility is caused by increased carrier scattering with polycrystallinity induced defects.

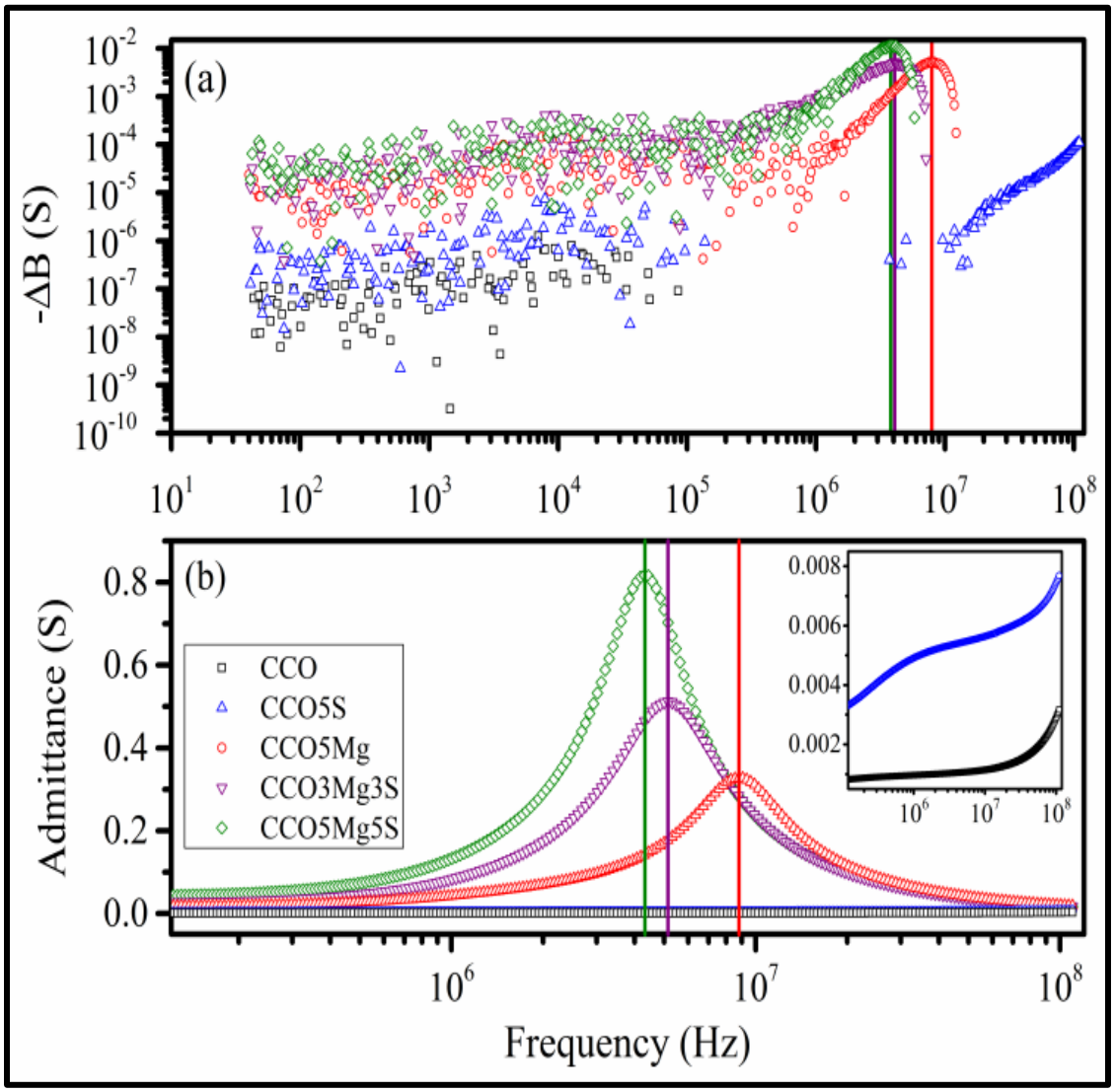

Figure 4.4: (a) Frequency dispersion of negative differential susceptance (3 V) and (b) admittance (0 V) of the pallets prepared with parallel capacitor geometry. Vertical lines in a and b are indicating the positions of f_r and A_{max} respectively of the corresponding materials. Inset of b is showing the dispersion of admittance of $CuCrO_2$ and $CuCrO_{1.9}S_{0.1}$ across same frequency range.

4.4. Conclusions:

We have extended our materials design strategy by simultaneous cationic-anionic doping in a prototype delafossite $CuCrO_2$ aiming to overcome the conduction bottleneck observed in contemporary *p*-TCOs. Mg and S are used as cationic and anionic dopants at Cr and O-site respectively with varying concentrations and their successful substitution is indicated by Rietveld refinement. By measuring the diffuse reflectance spectra, it is evident that all the doped materials have wide band gap in 'transparent' optical region. DC conductivity carried out across 80 – 300 K has revealed a 'crossover' near 140 K below which the transport is governed by VRH and above by thermal activation. σ_{dc} is twice as large for $CuCr_{0.95}Mg_{0.05}O_{1.9}S_{0.1}$ at 300K than $CuCr_{0.95}Mg_{0.05}O_2$ with increased E_a and decreased μ_{dc}. Evidence of gradual increase in 'metallicity' upon co-doping are exhibited by lower frequency shift of $-\Delta B$ and A_{max}. The decrease in μ_{dc} upon co-doping can be thought to arise from polycrystallinity induced defects and material in thin film form can be expected to overcome this problem. Although preparation of thin films of this complicated co-doped ternary oxide is technologically an uphill task but it is underway.

4.5. References:

1. C G Granqvist 2007 *Sol. Energy Mater. Sol. Cells* **91** 1529.

2. K Ellmer 2012 *Nat. Photonics* **6** 809.

3. D S Ginley, H Hosono and D C Paine 2011 Handbook of transparent conductors *Springer.*

4. E Fortunato, P Barquinha, and R Martins 2012 *Adv. Mater.* **24** 2945.

5. D S Ginley and C Bright 2000 *MRS. Bull.* **25** 15.

6. A N Banerjee and K K Chattopadhyay 2005 *Prog. Cryst. Growth Charact. Mater*. **50** 52.

7. H Ohta and H Hosono 2004 *Mater. Today* **3** 42.

8. J F Wager, D A Keszler and R E Presley 2007 Transparent electronics *Springer.*

9. S Sheng, G Fang, C Li, S Xu and X Zhao 2006 *Phys. Stat. Sol*. **203** 1891.

10. H Kawazoe, M Yasakuwa, H Hyodo, M Kurita, H Yanagi and H Hosono 1997 *Nature* **389** 939.

11. R Nagarajan, A D Draeseke, A W Sleight, and J Tate 2008 *J. Appl. Phys*. **9** 8022.

12. A Kudo, H Yanagi, H Hosono and H Kawazoe 1998 *Appl. Phys. Lett.* **73** 220.

13. K Ueda, S Inoue, S Hirose, H Kawazoe and H Hosono 2000 *Appl. Phys. Lett.* **77** 2701.

14. E Arca, K Fleischer and I V Shvets 2011 Appl. Phys. Lett. **99** 111910.

15. Arnold T, Payne D J, Bourlange A, Hu J P, Egdell R G, Piper L F J, Colakerol L, De Masi A, Glans P A, Learmonth T, Smith K E, Guo J, Scanlon D O, Walsh A, Morgan B J and Watson G. W. 2009 Phys. Rev. B **79** 075102.

16. D O Scanlon and G W Watson 2011 J. Mat. Chem. **21** 3655.

17. N Mazumder, D Sen, U K Ghorai, R Roy, S Saha, N S Das and K K Chattopadhyay 2013 *J. Phys. Chem. Lett.* **4** 3539.

18. A B Garg, A K Mishra, K K Pandey and S M Sharma 2014 *J. Appl. Phys*. **116** 133514.

19. Q J Liu, F S Liu and Z T Liu 2015 *Chem. Phys. Lett*. **633** 181.

20. S Som and S K Sharma 2012 *J. Phys. D: Appl. Phys*. **45** 415102.

21. H Y Chen, W J Yang and K P Chang 2012 Appl. Surf. Sci. **258** 8775.

22. M J Han, Z H Duan, J Z Zhang, S Zhang, W Li Y, Z G Hu and J H Chu 2013 J. Appl. Phys. **114** 163526.

23. Li D, Fang X, Deng Z, Dong W, Tao R, Zhou S, Wang J, Wang T, Zhao Y and Zhu X 2009 *J. Alloy Compd*. **486** 462.

24. R Kumar and N Khare 2008 *Thin Solid Films* **516** 1302.

25. Li X R, Han M J, Chang P, Hu Z G, Li Y W, Zhu Z Q and Chu J H 2014 Appl. Phys. Lett. **104** 012103.

26. B J Ingram, T O Mason, R Asahi, K T Park and A J Freeman 2001 Phys. Rev. B **64** 155114.

27. G Hautier, A Miglio, G Ceder, G M Rignanese and X Gonze 2013 Nat. Comm. **4** 2292.

28. Bhatia A, Hautier G, Nilgianskul T, Miglio A, Sun J, Kim H J, Kim K H, Chen S, Rignanese G M, Gonze X and Suntivich J 2016 Chem Mater **28(1)** 30.

29. J A Caraveo-Frescas, P K Nayak, H A Al-Jawhari, D B Granato, U Schwingenschlögl, H N Alshareef 2013 ACS Nano **7(6)** 5160.

30. Y Wang, J Chen, L Dong and D Ma 2013 J. Appl. Phys. **114** 113703.

5. Experimental observation of valence band dispersion and increased hole conductivity in $CuCr_{1-x}Li_xO_{2-y}S_y$

Chapter 5

5.1. Introduction:

The evolution of promising *p*-type transparent conductive oxides (*p*-TCOs) is of great interest since the thin films of $CuAlO_2$ with delafossite structure was first reported in 1997 [1]. Due to the influence of their functional incorporation of promising carrier mobility along with visible transparency, these delafossites could play important roles in numerous photo-electrochemical and photo-electronic applications [2-4]. Most TCOs are widely explored with devices exploiting enormous area in materials chemistry. One of the hardest contemporary global material challenges is to develop *p*-TCOs having comparable conductivity with many popular *n*-TCOs like ZnO, SnO_2 and also In_2O_3 [1, 5-8]. It is extremely difficult to achieve significant *p*-type conduction via acceptor doping. The common reason is strongly localized $O\ 2p$ character of the top of valence band, leading to difficulty in harvesting shallow acceptors by imparting greater effective mass to the majority carriers [8]. The deficiency of high-achievement *p*-TCOs impedes the realization of advanced applications including transparent transistors, electronic devices and diodes [9, 10]. To date, promising *p*-TCOs investigated both in bulk and thin films exhibit delafossite structure with a general composition AMO_2 ($A = Cu, Ag$; and $M = Cr, Al, B, Fe, Ga, In$ etc.) [11-16]. Among them, Mg-doped $CuCrO_2$ has the highest electrical conductivity of 220 Scm^{-1} as well as transparency in the visible regime [17]. Recently, Han *et al.* have demonstrated that $CuCrO_2$ films [18] produced by sol-gel technique has the conductivity about 3.85 Scm^{-1}. Many other Cr related *p*-TCOs reported in recent literature are $LaCrO_3: Sr, MnCr_2O_4: Li$, $Cr_2O_3: Mg$ with some spinel oxides including

$ZnCO_2O_4$ and $ZnRh_2O_4$ [19-21]. Hosono *et al.* have demonstrated the idea to substitute oxygen with chalcogen (S, Se) elements in the layered *p*-type oxides $LaCuOCh$, resulting more delocalization *p*-holes [22, 23]. Arca *et al.* have carried out co-doping in Cr_2O_3 for improving conductivity and extracting the optical transparency [24]. Recently, Rattanathrum *et al.* [25] have investigated the effects of Ge composition on the structural and physical properties of $CuCrO_2$. Besides, Majee *et al.* [26] have reported enhancement of its electrical and optical properties in Ti-doped $CuCrO_2$. Previously, our group have developed the scheme of chalcogen doping at O-site in prototype delafossite $CuAlO_2$ alongside simultaneous cationic-anionic substitution in $CuCrO_2$ aiming band dispersion and delocalization of holes [27, 28]. Additionally, Hagel reported that Li- doping in Cr_2O_3 enhances its electrical conductivity [29]. The effect of Li-doping on the optical and electrical characteristics of NiO films [30] are studied in details by Dutta *et al.* According to Qiu *et al.*, Li-doped ZnO films deposited over glass substrates also exhibit significant hole conductivity [31]. Furthermore, doping with Li can raise the optical transparency and promote the crystallinity in general [32]. As a group I element, substitutional Li is expected to generate sufficient number of shallow acceptor states, leading to free holes. Throughout this article, we have used Kröger–Vink notation to explain the dopant ions and their lattice position in the crystal. For the Li^{1+} ion situated at Cr^{3+} site with an associated hole, we have used the notation $Li_{Cr}^{\bullet\bullet}$ and for the S^{2-} ion situated at O^{2-} site with an associated acceptor state, we have used the notation $S_O^{\times}$. From here on, the samples will simply be labelled as CCO, $CCO/Li_{Cr}^{\bullet\bullet}$, $CCO/S_O^{\times}$, and $CCO/(Li_{Cr}^{\bullet\bullet} + S_O^{\times})$ according to their cationic and anionic doping. Thus, the purpose of this investigation is to examine the correlated changes in the structural, optical and transport properties upon site dependent hole doping ($Li_{Cr}^{\bullet\bullet}$, $S_O^{\times}$ and $Li_{Cr}^{\bullet\bullet} + S_O^{\times}$) in prototype *p*-TCO $CuCrO_2$ and to experimentally validate the consequent band dispersion.

5.2. Experimental details:

5.2.1. Materials and methods

Single phase of bulk $CuCr_{1-x}Li_xO_{2-y}S_y$ powder is prepared by the solid state heating [28]. The stoichiometric composition of CuO (Merck), Cr_2O_3 (Sigma-Aldrich), Li_2O (Sigma-Aldrich) and CH_4N_2S (Merck) are used to keeping x and y, 0 or 5 atomic %.

5.2.2. Characterizations

The crystalline phase quality of the powder is assessed by XRD (Bruker D8 Advance) using a Cu K_α radiation (λ = 1.5418 Å) at 300 K. The continual scanning mode ($\theta - 2\theta$) across 20−80° with step interim of 0.02° and scan rate 2s/step is selected for all the samples. The structural analysis using XRD pattern are borne out by Rietveld refinement with FULLPROF programme and using the refined parameters, the schematic of the supercells are generated by DIAMOND. Compositional analysis and valence band dispersion are investigated by X-ray photoelectron spectroscopy (XPS) with a monochromatic Al K_α X-ray source (hν = 1486.6 eV) and hemispherical analyzer (SPECS, HAS 3500). Measurements are performed at ~ 2×10^{-8} mbar. Analysis is carried out by CASA XPS software and C 1s at 284.6 eV is considered as internal reference. The diffuse spectral reflectance of all powders is carried out across the wavelength region of 220-2200 nm using Shimadzu UV-Vis 3600 spectrophotometer. Admittance responses are studied across the frequency range of 40 Hz to 110 MHz with a 2 V external dc-biased using an Agilent (4294A) precision impedance analyzer at 300 K. The electrical conductivity measurements are achieved by a source meter (KEITHLEY 4200) with the conventional two-probe method under helium atmosphere over the temperature range of 4 – 300 K. The current–voltage (I-V) profiles are acquired by using HIOKI (3522–50) LCR Hi-TESTER at 300 K. *p*-type conduction behaviour is established by the

Hall measurement system using the four- probe Van der Pauw configuration with constant magnetic field 0.15 Tesla at 300 K. A high-performance electrically conductive silver paste (Alfa Aesar™ 4407518) was used to make point contacts with a sample at the corner site and they were connected to thin copper wires.

5.3. Results and discussions:

5.3.1. Structural properties

The crystalline single phase (Figure 5.1) of the synthesized undoped and co-doped (JCPDS: 74-0983) materials are concluded from as obtained powder diffraction patterns. Thus, there is no evidence for any secondary phase formation due to site selective hole doping in the host lattice. The diffraction peaks are found to be consistent with layered 3R-type group-III delafossite structure having the rhombohedral group $R\bar{3}m$ (#166). The lattice parameter (a and c), unit cell volume (V_0) are calculated using Rietveld refinement and average crystalline size (D) of the materials are obtained by the Williamson – Hall (W–H) formalism and are enlisted in Table 5.1. It is noted that the parameters a, V_0 and D increased with $Li_{Cr}^{\bullet\bullet}$ incorporation whereas $S_O^{\times}$ decreased it. However, the parameter c decreased almost linearly from 17.0999 Å to 17.0859 Å, respectively for the doped co-doped materials compared with undoped $CuCrO_2$. This is reasonable as the ionic radii of Li^{1+} (0.900 Å) being greater than that of Cr^{3+} (0.755 Å). The experimental atomic site occupancy of $Li_{Cr}^{\bullet\bullet}$ and $S_O^{\times}$ are determined to be 1.24% and 1.67% in contrast to the calculated 5% (Table 5.2). This reduction in the concentration of $Li_{Cr}^{\bullet\bullet}$ and $S_O^{\times}$ is acceptable due to their strong thermal evaporation tendency from the solid matrix. For the structural refinement, the Wyckoff position of Li and S are considered as equivalent with that of Cr and O respectively; while the pseudo –Voigt peak function

is utilized to simulate the Brag peaks profile. The goodness of fit (GOF) ($\chi^2 = R^2_{wp}/R^2_{exp}$) varies from 1.3 to 1.4 and can be ascribed to the ionic vacancies as well as interstitial defects which are inevitable in the polycrystalline materials.

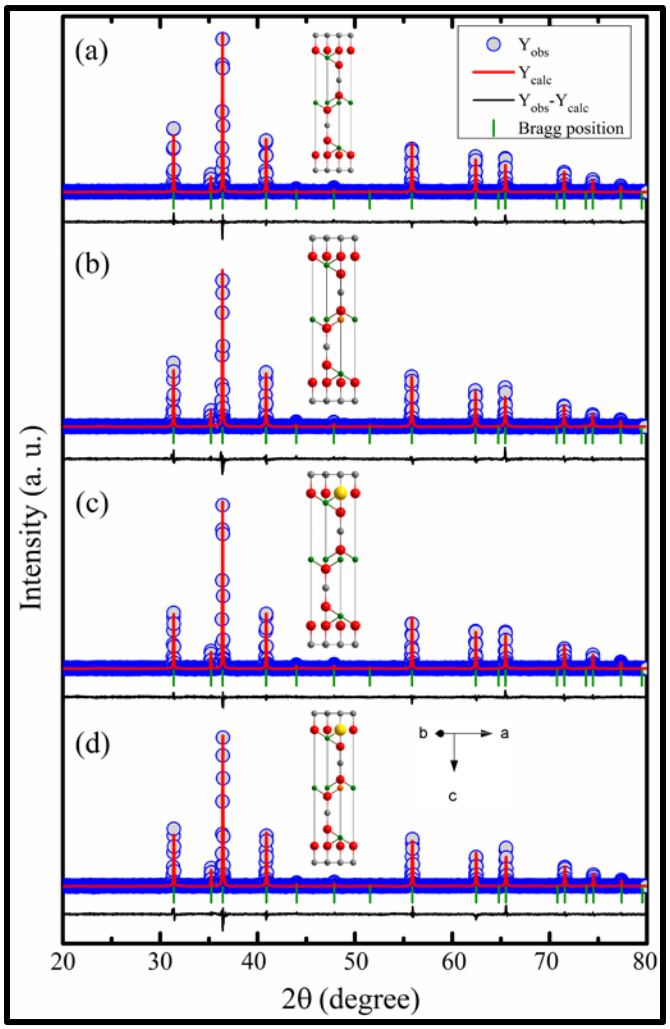

Figure 5.1: X-ray diffraction $(\theta - 2\theta)$ profile of (a) CCO, (b) $CCO/Li^{\bullet\bullet}_{Cr}$, (c) $CCO/S^{\times}_{O}$ and (d) $CCO/(Li^{\bullet\bullet}_{Cr} + S^{\times}_{O})$. The solid red lines express the best fit obtained for the experimental data (blue circles) from the Rietveld analysis using the FULLPROF programme. The short vertical green lines indicate the position of associated the Bragg peaks. The black curve represents the difference between the experimental and calculated profile intensities, which is displayed at the bottom of the

graph. The schematics of side view of the refined supercells are obtained from DIAMOND. Gray, orange, red, yellow and green balls are representing copper (Cu), Lithium (Li) oxygen (O), sulfur (S) and chromium (Cr), respectively.

Table 5.1: Unit cell parameters, cell volume and crystalline size obtain by Rietveld refinement and Williamson-Hall plots for all materials.

Materials	Lattice parameter a=b (Å)	Lattice parameter c (Å)	Cell Volume V_0 (Å^3)	Crystalline Size D (nm)
CCO	2.9741	17.0999	130.98	81.76±3.39
$CCO/Li_{Cr}^{\bullet\bullet}$	2.9748	17.0983	131.07	87.79±3.47
$CCO/S_O^{\times}$	2.9736	17.0961	130.92	74.55±4.00
$CCO/(Li_{Cr}^{\bullet\bullet} + S_O^{\times})$	2.9754	17.0859	131.12	88.71±4.07

5.3.2. Chemical properties

The XPS measurements (Figure 5.2) are carried out to determine the valence states of ions and to observe the effect of Li, S co-doping on the width of the valence band. Typical survey spectra of CCO and $CCO/(Li_{Cr}^{\bullet\bullet} + S_O^{\times})$ are portrayed in Figure 5.2a exhibiting major elemental presence in as prepared powders. The dashed vertical lines in the Cu 2*p* XPS spectra (Figure 5.2b) indicate binding energy positions commonly found for Cu^{+} and Cu^{2+} in CuO_2 (932.2 eV) and CuO (934 eV).

Table 5.2: Element composition of the dopant concentration for doped and co- doped materials.

Materials	Element	Dopant concentration, (at%)
$CCO/Li_{Cr}^{\bullet\bullet}$	Li	1.15
$CCO/S_O^{\times}$	S	1.67
$CCO/(Li_{Cr}^{\bullet\bullet} + S_O^{\times})$	Li S	1.24 1.79

Upon deconvolution of Cu 2*p* doublets for both the samples, one can clearly observe the relative increase of characteristic shake-up satellite Cu^{2+} contribution for $CCO/(Li_{Cr}^{\bullet\bullet} + S_O^{\times})$. In case of $CCO/(Li_{Cr}^{\bullet\bullet} + S_O^{\times})$, Cu 2p core level peak shifts towards lower binding energy side which can be attributed to Fermi level shifting towards valence band edge due to co-doping [33]. For the Li^{+} substitution at Cr^{3+} site, higher valence states of Cu ions are expected to appear in order to maintain charge balance. As the amount of doping is weak for both $Li_{Cr}^{\bullet\bullet}$ and $S_O^{\times}$ in $CCO/(Li_{Cr}^{\bullet\bullet} + S_O^{\times})$ (atomic site occupancy of $Li_{Cr}^{\bullet\bullet}$ and $S_O^{\times}$ are determined to be 1.24% and 1.67%), Li 1*s* and S 2*p* signals are rather weak (Figure 5.2c) as a guide to eye a solid black line is superimposed with the experimental data to indicate the presence of corresponding elements. For CCO, the near-Fermi-level leading structure primarily consists of the Cr 3*d* nature with a small contribution from the Cu 3*d* due to Cu

3*d* – O 2*p* – Cr 3*d* hybridization. This result shows that a doped hole will principally have the Cr 3*d* nature. Because of large photoionization cross section, significant contribution from O 2*p* states is obvious within the width of valence band. The overall experimental valence band width of CCO is observed to be almost 9 eV, which is consistent with previous literature [34]. Upon the incorporation of shallow acceptor S 3*p* states, the width of valence band increases to 11 eV for $CCO/(Li_{Cr}^{\bullet\bullet} + S_O^{\times})$ (Figure 5.2d). This observation is fairly consistent with our previous report of valence band dispersion in S doped $CuAlO_2$ [27].

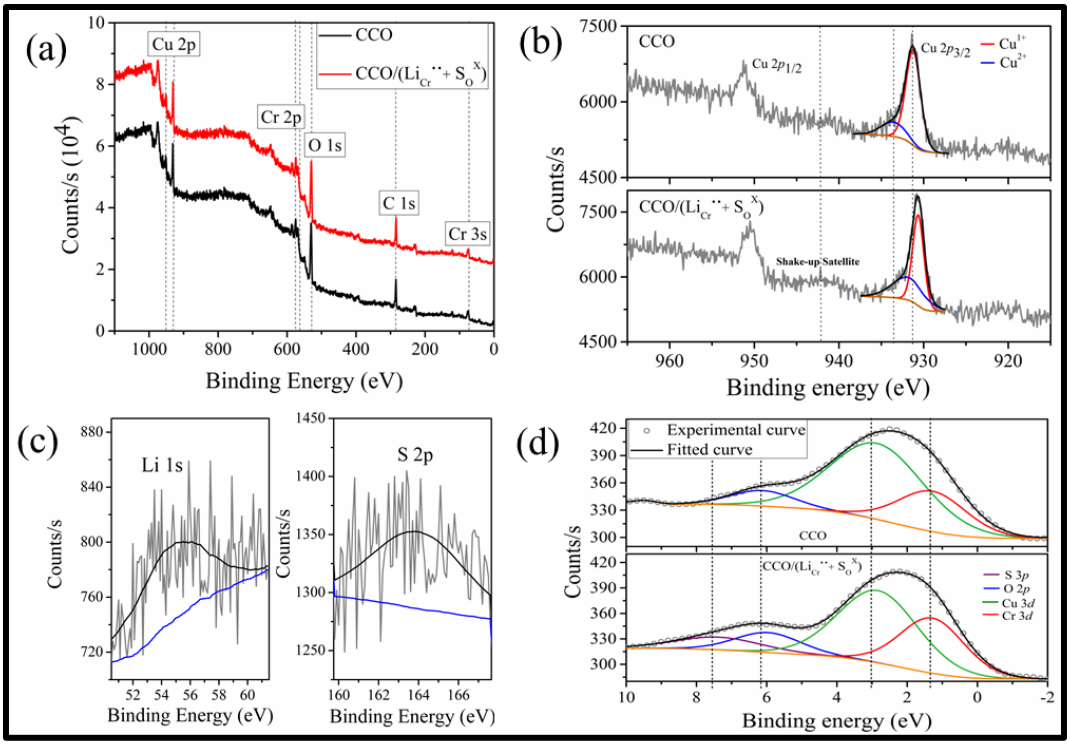

Figure 5.2: (a) XPS survey spectra of CCO and $CCO/(Li_{Cr}^{\bullet\bullet} + S_O^{\times})$. (b) Relative increase in Cu^{2+} content in $CCO/(Li_{Cr}^{\bullet\bullet} + S_O^{\times})$ compared to CCO is delineated along with minor energy red shift of Cu 2*p* doublet upon co-doping. (c) HR spectra of Li 1s and S 2p. (d) XPS spectra of the VB region of CCO and $CCO/(Li_{Cr}^{\bullet\bullet} + S_O^{\times})$, which is deconvoluted considering major orbital contributions for elucidating VB dispersion.

5.3.3. Optical properties

The Kubelka-Munk (K-M) formalism [35] is applied to determine the optical band gap of respective materials from the diffuse spectral reflectance across the wavelength range 220-2200 nm where spectra are calibrated with a white reference $BaSO_4$. The K-M model is expressed in the following form:

$$F(R_\infty) = \frac{(1-R_\infty)^2}{2R_\infty} = \frac{K}{S} \quad , \qquad (1)$$

Here $F(R_\infty)$ is the so-called K-M function, where $R_\infty = R_{Sample}/R_{BaSO_4}$ is the relative diffuse reflectance of light scattering from an infinitely thick of sample layer to the absolute non-absorbing matrix ($BaSO_4$), K is the molar absorption coefficient ($K = 2\alpha$) and S is the scattering coefficient. The direct energy gap E_g and absorption coefficient (α) of a material is relevant to the usual Tauc relation [36] and could be expressed as,

$$\alpha h\nu = A_1(h\nu - E_g)^{1/2} \, , \qquad (2)$$

Where, A_1 is proportionality constant and $h\nu$ is the photon energy. Appling Eq. (1) and (2), the following relation is obtained $[F(R_\infty)h\nu]^2 = A_2(h\nu - E_g)$. The energy band gap ($E_g$) is achieved by the extrapolating of linear fitted portion at $[F(R_\infty)h\nu]^2 = 0$ with a plot between $[F(R_\infty)h\nu]^2$ versus $h\nu$ which are shown in Figure 5.3. The values of band gap reveal a minute decrease in band gap with doping/co-doping. While pristine CCO exhibits a band gap of 3.54 eV,

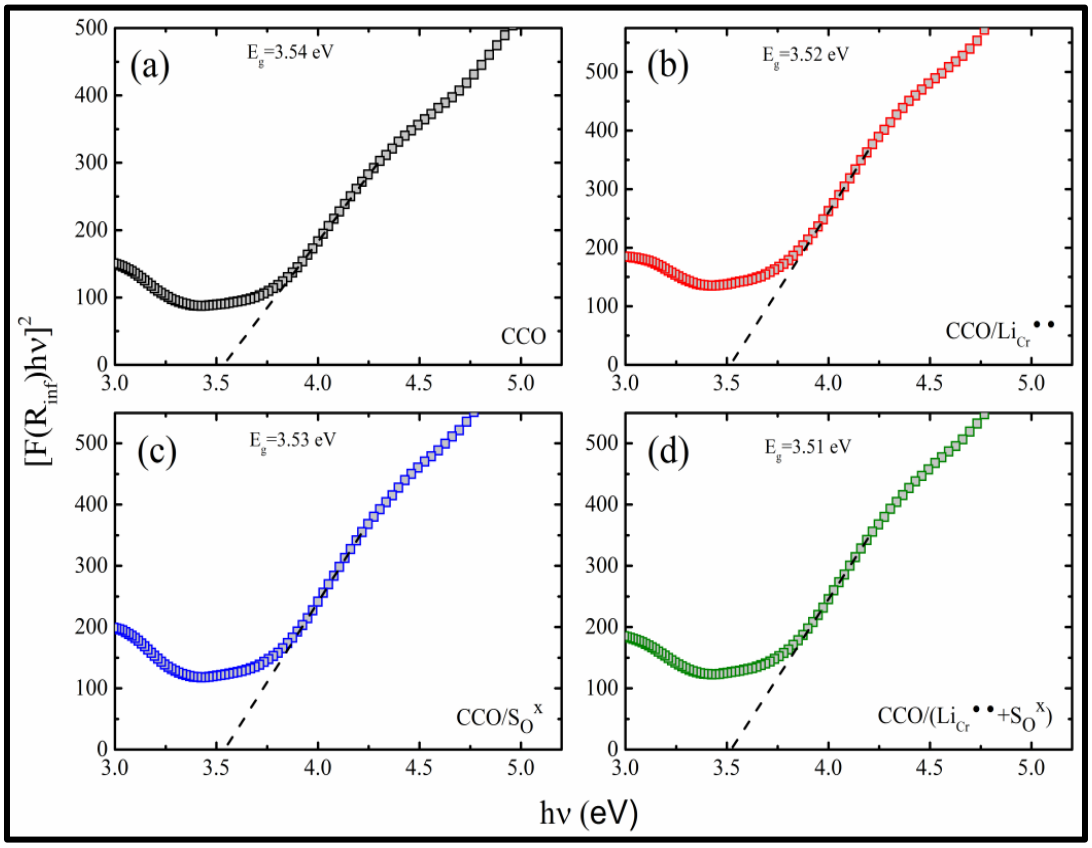

Figure 5.3: The plot of $[F(R_{inf})h\nu]^2$ versus $h\nu$ for obtaining optical band gap from diffuse reflectance spectra of all the materials. The x-intercept of extrapolated black dotted lines is signifying the associated optical energy gap.

$CCO/(Li_{Cr}^{\bullet\bullet} + S_O^{\times})$ shows a reduced band gap of 3.51 eV. It is to be noted that as the amount of doping is weak for both doped and co-doped samples, unit cell parameters (a and c) exhibit negligible changes which is evident from the Rietveld refinement. Infects, reduction of the optical energy gap by the addition of Li is due to its lesser atomic volume in comparison with Cr, which generates various defects in the delafossite structure [37].The values of direct energy gap of the materials are larger than 3.1 eV in visible range. Therefore, all the prepared materials can transmit the photons energy in region of visible light spectrum as a transparent material in the visible light

region. Thus, it is evident that the wide band gap feature within the transparent optical region is maintained for the doped materials and the calculated E_g of $CuCrO_2$ agrees well with previous publication [38].

5.3.4. Admittance analysis

To investigate the admittance characteristics, the powders are cold pressed into pellets by applying a pressure of 1 GPa. By plotting the negative differential susceptance $-\Delta B$ as a function of frequency, a characteristic frequency $f_r = {\tau_r}^{-1}$ is calculated (Figure 5.4a) associated with the maximum in $-\Delta B$. Now, the characteristic time τ_r and the average hole transit time τ_{dc} are related by $\tau_{dc} = 0.56\tau_r$ [39]. From Figure 5.4a, it is observed that upon co-doping, f_r shifts gradually to the lower frequency [for CCO (62.547 MHz), $CCO/S_O^{\times}$ (8.292 MHz), $CCO/Li_{Cr}^{\bullet\bullet}$ (6.538 MHz) and $CCO/(Li_{Cr}^{\bullet\bullet} + S_O^{\times})$ (5.310 MHz)] with increasing τ_{dc} [for CCO (8.95 ns), $CCO/S_O^{\times}$ (67.4 ns), $CCO/Li_{Cr}^{\bullet\bullet}$ (85.65 ns) and $CCO/(Li_{Cr}^{\bullet\bullet} + S_O^{\times})$ (0.11μs)] at 2 V of external applied bias. In Figure 5.4b, a downshift is detectable in the frequency response of the admittance maxima (A_{max}) for co-doping [for CCO (74.754MHz), $CCO/S_O^{\times}$ (7.363 MHz), $CCO/Li_{Cr}^{\bullet\bullet}$ (6.347 MHz) and $CCO/(Li_{Cr}^{\bullet\bullet} + S_O^{\times})$ (5.470 MHz)]. Due to increase in the hole concentration upon co-doping, A_{max} reaches to 0.049 S for $CCO/(Li_{Cr}^{\bullet\bullet} + S_O^{\times})$. Accordingly, collision frequency among charge carriers also increases resulting in the downshift of the A_{max}. At lower frequency, A_{max} denotes a smaller screening length and hence indicating decreased hole mobility due to amplified carrier scattering due to polycrystallinity induced defects.

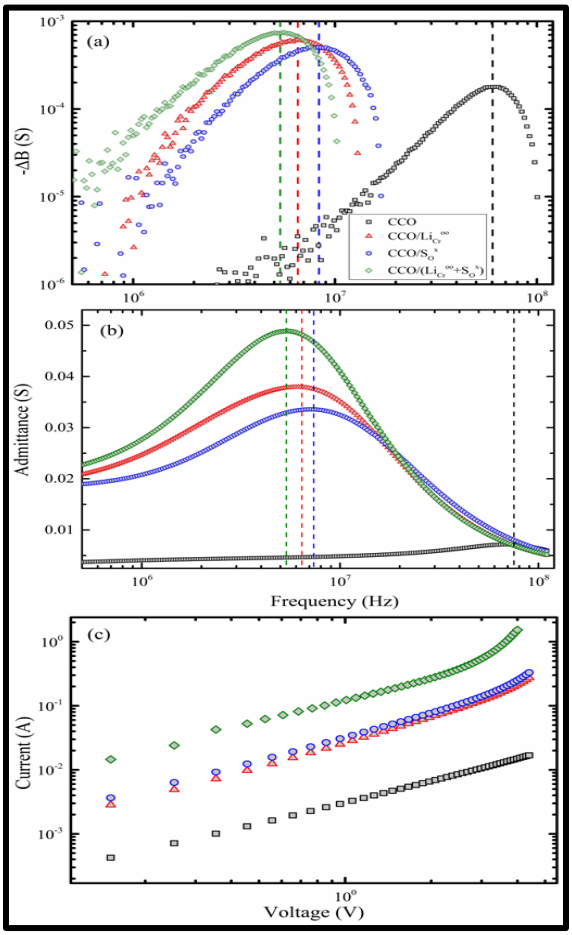

Figure 5.4: (a) Frequency dependent of negative differential susceptance spectra with 2V external bias and (b) admittance spectra of $CuCr_{1-x}Li_xO_{2-y}S_y$.Vertical lines of (a) and (b) are implying the positions of f_r and A_{max} respectively and (c) Log – log representation of current–voltage profile of the corresponding materials.

In Figure 5.4c, the log – log representation of current – voltage for all pallets where current is observed to increases more than ten times for $CCO/(Li_{Cr}^{\bullet\bullet} + S_O^{\times})$ compared to the undoped CCO. Furthermore, a steeper increase in the current can be distinguished upon co-doping evidencing a decrease in the resistivity of the codoped material.

5.3.5. Electrical properties

Figure 5.5 illustrates the temperature variation of the electrical conductivity (σ_{dc}) for $CCO/Li_{Cr}^{\bullet\bullet}$ and $CCO/(Li_{Cr}^{\bullet\bullet} + S_O^{\times})$ across the temperature range (4 – 300 K). Four fold increase in the conductivity of $CCO/(Li_{Cr}^{\bullet\bullet} + S_O^{\times})$ is observed compared to $CCO/Li_{Cr}^{\bullet\bullet}$ at room temperature with the magnitude of σ_{dc} determine to be 0.020 S-cm^{-1} and 0.005 S-cm^{-1} for $CCO/(Li_{Cr}^{\bullet\bullet} + S_O^{\times})$ and $CCO/Li_{Cr}^{\bullet\bullet}$, respectively. The Hall coefficient with a positive sign is obtained for doped and co-doped materials, suggesting *p*-type conductivity with other related parameters are presented into Table 5.3. Figure 5.5a shows the linear relationship between $\ln(\sigma)$ versus T^{-1} for the temperature range of 185 - 300K for $CCO/Li_{Cr}^{\bullet\bullet}$ and 190 - 300K for $CCO/(Li_{Cr}^{\bullet\bullet} + S_O^{\times})$ respectively, indicating thermally activated electrical conduction and the conductivity (σ_{dc}) follows the relation as:

$$\sigma_{dc} = \sigma_0 \exp(-E_a/K_B T)\,, \qquad (3)$$

Here σ_0 is a constant, E_a, k_B and T are the thermal activation energy, Boltzmann's constant and absolute temperature, respectively. The E_a values are calculated to be 219.4 meV and 226.6 meV from the slope of best line fits for $CCO/Li_{Cr}^{\bullet\bullet}$ and $CCO/(Li_{Cr}^{\bullet\bullet} + S_O^{\times})$, respectively. For the polycrystalline $CuCr_{0.96}Mg_{0.04}O_2$ compound, Okuda *et al.* have found E_a to be 278 meV [40]. The magnitude of E_a values conveys that the carrier transport inside the valence band is thermally activated from the acceptor.

Table 5.3: Electrical transport parameters obtained from Arrhenius plots and Hall (Van der Pauw) measurements for $CCO/Li_{Cr}^{\bullet\bullet}$ and $CCO/(Li_{Cr}^{\bullet\bullet} + S_O^{\times})$ at 300 K. Here, E_a, σ_{dc}, R_H, n and μ_{dc} are the activation energy, dc electrical conductivity, Hall coefficient, carrier concentration and hole mobility, respectively.

Materials	E_a meV	σ_{dc} (S/cm)	R_H (cm^3C^{-1})	n (cm^{-3})	μ_{dc} ($cm^2V^{-1}s^{-1}$)
$CCO/Li_{Cr}^{\bullet\bullet}$	219.4	0.005	13.11×10^3	4.77×10^{14}	65.51
$CCO/(Li_{Cr}^{\bullet\bullet} + S_O^{\times})$	226.6	0.020	1.17×10^3	5.32×10^{15}	23.50

The estimated hole mobility of $CCO/Li_{Cr}^{\bullet\bullet}$ (65.51 $cm^2V^{-1}s^{-1}$) is larger than that of $CCO/(Li_{Cr}^{\bullet\bullet} + S_O^{\times})$ (23.50 $cm^2V^{-1}s^{-1}$) at room temperature. However, no linear relationship is observed between $\ln(\sigma)$ versus T^{-1} when the temperature is less than 30 K for $CCO/(Li_{Cr}^{\bullet\bullet} + S_O^{\times})$ and $CCO/Li_{Cr}^{\bullet\bullet}$ as shown in Figure 5.5c and 5.5d. Rather, the σ_{dc} of both materials across 4 – 30 K regime are identified to be consistent with three- dimensional (3D) Mott's variable-range hopping (VRH) conduction model. For this regime, the conductivity (σ_{dc}) is well described by using the equation [41, 42]:

$$\sigma_{dc} = \sigma_0' \exp\left[-\left(\frac{T_{Mott}}{T}\right)^{1/4}\right], \qquad (4)$$

Here σ_0' and T_{Mott} are the pre-factor and the Mott characteristic temperature. The linear fits of $\ln(\sigma T^{1/2})$ versus $T^{-1/4}$ plot for $CCO/Li_{Cr}^{\bullet\bullet}$ and $CCO/(Li_{Cr}^{\bullet\bullet} + S_O^{\times})$ are shown in Figure 5.5b.With temperature (< 30 K) below thermal activation energy, the occurrence of hole hopping to the

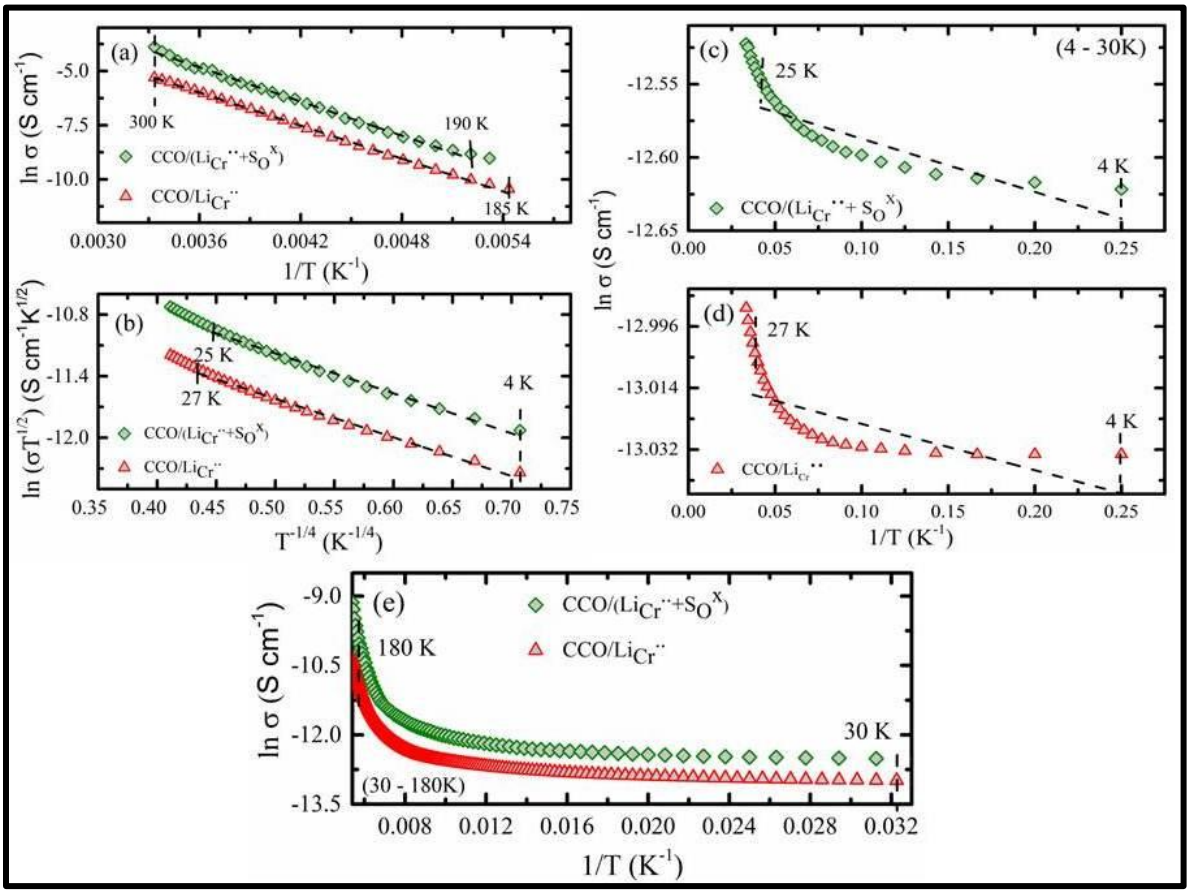

Figure 5.5: (a) Temperature dependence DC Arrhenius plots of ln(σ) vs. T^{-1} for $CCO/Li_{Cr}^{\bullet\bullet}$ and $CCO/(Li_{Cr}^{\bullet\bullet} + S_O^{\times})$ with the temperature between 185- 300 K. (b) The low temperature (4 - 30 K) conductivity plots of ln($\sigma T^{1/2}$) vs. $T^{-1/4}$ for $CCO/Li_{Cr}^{\bullet\bullet}$ and $CCO/(Li_{Cr}^{\bullet\bullet} + S_O^{\times})$, considering three-dimensional (3D) Mott's VRH mechanism.(c) and (d) DC Arrhenius plots of ln(σ) vs. T^{-1} for $CCO/(Li_{Cr}^{\bullet\bullet} + S_O^{\times})$ and $CCO/Li_{Cr}^{\bullet\bullet}$ with the temperature between 4 - 30 K (e) The crossover region with the temperature between 30 –180 K.

Li site due to compression between the neighbouring Cu sites indicates the 3D carrier transport, dominating the charge conduction mechanism. Here, $N(E_F)$ is the density of states (DOS) at E_F, which can be expressed as:

$$N(E_F) = 2.12 \times 10^9 \sigma_0'^3 T_{Mott}^{1/2}\ cm^{-3}eV^{-1}, \qquad (5)$$

and comes out to be 3.21×10^{22} $cm^{-3}eV^{-1}$ and 1.53×10^{23} $cm^{-3}eV^{-1}$ for $CCO/Li_{Cr}^{\bullet\bullet}$ and $CCO/(Li_{Cr}^{\bullet\bullet}+S_O^{\times})$ respectively. It should be mentioned here that this difference to the moderate carrier concentration of 4.77×10^{14} cm^{-3} which also results in large carrier mobility (65.51 $cm^2V^{-1}s^{-1}$) for $CCO/Li_{Cr}^{\bullet\bullet}$ due to negligible ionized impurity scattering. It is important that calculated $N(E_F)$ (1.53×10^{23} $cm^{-3}eV^{-1}$) for $CCO/(Li_{Cr}^{\bullet\bullet}+S_O^{\times})$, which is of higher order in comparison to $CCO/Li_{Cr}^{\bullet\bullet}$ (3.21×10^{22} $cm^{-3}eV^{-1}$). Existence of carrier density (5.32×10^{15} cm^{-3}) increases one order of magnitude in $CCO/(Li_{Cr}^{\bullet\bullet}+S_O^{\times})$. Now, for polycrystalline materials, excess amount of charge carriers get scattered from various defect centres [27]. Because of that the magnitude of σ_{dc} is higher for $CCO/(Li_{Cr}^{\bullet\bullet}+S_O^{\times})$ but with decreased μ_{dc} (23.50 $cm^2V^{-1}s^{-1}$) than $CCO/Li_{Cr}^{\bullet\bullet}$. In Figure 5.5e, we observe a regime from 30 – 180 K which cannot be fitted using any known conduction mechanism. We believe that in the specified temperature region, both activated and hopping conduction are at play.

5.4. Conclusions:

In summary, a proposition for preparing group IIIA *p*-TCO delafossite with light hole states is presented by doping prototype $CuCrO_2$ with $Li_{Cr}^{\bullet\bullet}$ and $S_O^{\times}$ induced holes. The structural, electrical, admittance and optical properties of doped and co-doped materials are analyzed. Valence band dispersion is experimentally demonstrated by x-ray photoelectron spectroscopy upon the incorporation of shallow S 3*p* acceptors, increasing the width of the valence band by 2 eV for $CCO/(Li_{Cr}^{\bullet\bullet}+S_O^{\times})$ compared to undoped $CuCrO_2$. The doped materials exhibit wide optical energy gap of about 3.5 eV, which is implying transparency in the visible region. Upon the incorporation of $Li_{Cr}^{\bullet\bullet}$ and $S_O^{\times}$, all the compounds exhibit p-type conduction and is demonstrated by positive Hall

coefficients. The shift of the maxima of negative differential susceptance toward lower frequency for $CCO/(Li_{Cr}^{\bullet\bullet} + S_O^{\times})$ signifies greater 'metallicity'. Temperature dependence (4-300 K) of dc electrical conductivity concludes that the holes are thermally activated above 190 K and variable range hopping mechanism is dominant below 30 K. DC conductivity of $CCO/(Li_{Cr}^{\bullet\bullet} + S_O^{\times})$ is estimated to be 0.020 S/cm, which is four times larger than $CCO/Li_{Cr}^{\bullet\bullet}$ at room temperature. The hole mobility of 23.50 $cm^2V^{-1}s^{-1}$ is obtained for $CCO/(Li_{Cr}^{\bullet\bullet} + S_O^{\times})$. These results reflect good opportunities to realize transparent opto-electronic utilization in similarly designed *P*-TCOs. In general, a proposition for generating light hole states in group IIIA p-TCO delafossite is presented upon valence band engineering of $CuCrO_2$ by doping with $Li_{Cr}^{\bullet\bullet}$ and $S_O^{\times}$ induced holes. Delocalization of lighter holes is evidenced from temperature dependence of DC electrical conductivity, which maintains the optical transparency as well. The introduction of $Li_{Cr}^{\bullet\bullet}$ is generating lighter holes compared to $Mg_{Cr}^{\bullet}$ and thus is a step ahead in overcoming the long standing conductivity bottleneck in the field of transparent semiconductor electronics. Achieving greater solubility of $Li_{Cr}^{\bullet\bullet}$ and $S_O^{\times}$ in the host matrix, aiming to conquer the hole conductivity bottleneck can be a promising direction of research.

5.5. References:

1. H. Kawazoe, M. Yasukawa, H. Hyodo, M. Kurita, H. Yanagi, H. Hosono, P-type electrical conduction in transparent thin films of $CuAlO_2$, Nature 389 (1997) 939.

2. J.W. Lekse, M.K. Underwood, J.P. Lewis, C. Matranga, Synthesis, Characterization, Electronic Structure, and Photocatalytic Behavior of $CuGaO_2$ and $CuGa_{1-x}Fe_xO_2$ (x= 0.05, 0.10, 0.15, 0.20) Delafossites, J. Phys.Chem. C 116 (2012) 1865-1872.

3. A. Nattestad, X. Zhang, U. Bach, Y. Cheng, Dye-sensitized $CuAlO_2$ photocathodes for tandem solar cell applications, J. Photonics Eng. 1 (2011) 011103.

4. D. Xiong, Z. Xu, X. Zeng, W. Zhang, W. Chen, X. Xu, M. Wang, Y.-B. Cheng, Hydrothermal synthesis of ultrasmall $CuCrO_2$ nanocrystal alternatives to NiO nanoparticles in efficient p-type dye-sensitized solar cells, J. Mater. Chem. 22 (2012) 24760-24768.

5. A. Kohan, G. Ceder, D. Morgan, C.G. Van de Walle, First-principles study of native point defects in ZnO, Phys. Rev. B 61 (2000) 15019.

6. K.G. Godinho, A. Walsh, G.W. Watson, Energetic and electronic structure analysis of intrinsic defects in SnO_2, J. Phys. Chem. C 113 (2008) 439-448.

7. A. Walsh, J.L. Da Silva, S.-H. Wei, C. Körber, A. Klein, L. Piper, A. DeMasi, K.E. Smith, G. Panaccione, P. Torelli, Nature of the band gap of In_2O_3 revealed by first-principles calculations and x-ray spectroscopy, Phys. Rev. Lett. 100 (2008) 167402.

8. H. Kawazoe, H. Yanagi, K. Ueda, H. Hosono, Transparent p-type conducting oxides: design and fabrication of pn heterojunctions, MRS Bull. 25 (2000) 28-36.

9. A. Banerjee, K. Chattopadhyay, Recent developments in the emerging field of crystalline p-type transparent conducting oxide thin films, Prog. Cryst. Growth Charact. Mater. 50 (2005) 52-105.

10. E. Fortunato, P. Barquinha, R. Martins, Oxide semiconductor thin-film transistors: a review of recent advances, Adv. Mater. 24 (2012) 2945-2986.

11. R.D. Shannon, D.B. Rogers, C.T. Prewitt, Chemistry of noble metal oxides. I. Syntheses and properties of ABO_2 delafossite compounds, Inorganic Chem. 10 (1971) 713-718.

12. S. Gao, Y. Zhao, P. Gou, N. Chen, Y. Xie, Preparation of $CuAlO_2$ nanocrystalline transparent thin films with high conductivity, Nanotechnology 14 (2003) 538.

13. J.W. Lekse, M.K. Underwood, J.P. Lewis, C. Matranga, Synthesis, Characterization, Electronic Structure, and Photocatalytic Behavior of $CuGaO_2$ and $CuGa_{1-x}Fe_xO_2$ (x= 0.05, 0.10, 0.15, 0.20) Delafossites, J. Phys. Chem. C 116 (2012) 1865-1872.

14. M. Yu, G. Natu, Z. Ji, Y. Wu, p-type dye-sensitized solar cells based on delafossite CuGaO2 nanoplates with saturation photovoltages exceeding 460 mV, J. Phys. Chem. Lett. 3 (2012) 1074-1078.

15. C.W. Teplin, T. Kaydanova, D.L. Young, J.D. Perkins, D.S. Ginley, A. Ode, D.W. Readey, A simple method for the preparation of transparent p-type Ca-doped $CuInO_2$ films: Pulsed-laser deposition from air-sintered Ca-doped $Cu_2In_2O_5$ targets, Appl. Phys. Lett. 85 (2004) 3789-3791.

16. W.C. Sheets, E.S. Stampler, M.I. Bertoni, M. Sasaki, T.J. Marks, T.O. Mason, K.R. Poeppelmeier, Silver delafossite oxides, Inorg. Chem. 47 (2008) 2696-2705.

17. R. Nagarajan, A. Draeseke, A. Sleight, J. Tate, p-type conductivity in $CuCr_{1-x}Mg_xO_2$ films and powders, J. Appl. Phys. 89 (2001) 8022-8025.

18. M. Han, Z. Duan, J. Zhang, S. Zhang, Y. Li, Z. Hu, J. Chu, Electronic transition and electrical transport properties of delafossite $CuCr_{1-x}Mg_xO_2$ ($0 \leq x \leq 12\%$) films prepared by the sol-gel method: A composition dependence study, J. Appl. Phys.114 (2013) 163526.

19. A.R. Nagaraja, K.H. Stone, M.F. Toney, H. Peng, S. Lany, T.O. Mason, Experimental characterization of a theoretically designed candidate p-type transparent conducting oxide: Li-doped Cr_2MnO_4, Chem. Mater. 26 (2014) 4598-4604.

20. L. Farrell, K. Fleischer, D. Caffrey, D. Mullarkey, E. Norton, I. Shvets, Conducting mechanism in the epitaxial p-type transparent conducting oxide Cr_2O_3: Mg, Phys. Rev. B 91 (2015) 125202.

21. M. Amini, H. Dixit, R. Saniz, D. Lamoen, B. Partoens, The origin of p-type conductivity in ZnM_2O_4 (M= Co, Rh, Ir) spinels, Phys. Chem. Chem. Phys.16 (2014) 2588-2596.

22. K. Ueda, S. Inoue, S. Hirose, H. Kawazoe, H. Hosono, Transparent p-type semiconductor: LaCuOS layered oxysulfide, Appl. Phys. Lett. 77 (2000) 2701-2703.

23. H. Hiramatsu, K. Ueda, H. Ohta, M. Hirano, T. Kamiya, H. Hosono, Degenerate p-type conductivity in wide-gap $LaCuOS_{1-x}Se_x$ (x= 0–1) epitaxial films, Appl. Phys. Lett. 82 (2003) 1048-1050.

24. E. Arca, K. Fleischer, I. Shvets, Magnesium, nitrogen codoped Cr_2O_3: A p-type transparent conducting oxide, Appl. Phys. Lett. 99 (2011) 111910.

25. P. Rattanathrum, C. Taddee, N. Chanlek, P. Thongbai, T. Kamwanna, Structural and physical properties of Ge-doped $CuCrO_2$ delafossite oxide, Ceramics International 43 (2017) S417-S422.

26. M. Majee, P. Bhobe, U. Deshpande, A. Nigam, Local crystal structure and physical properties change of p-type transparent conducting oxide: $CuCrO_2$ upon Ti-substitution, J. Appl. Phys. 122 (2017) 225111.

27. N. Mazumder, D. Sen, U.K. Ghorai, R. Roy, S. Saha, N.S. Das, K.K. Chattopadhyay, Realizing direct gap, polytype, group IIIA delafossite: Ab initio forecast and experimental validation considering prototype $CuAlO_2$, J. Phys. Chem. Lett. 4 (2013) 3539-3543.

28. P. Mandal, N. Mazumder, S. Saha, U.K. Ghorai, R. Roy, G.C. Das, K.K. Chattopadhyay, A scheme of simultaneous cationic–anionic substitution in $CuCrO_2$ for transparent and superior p-type transport, J. Phys. D: Appl. Phys. 49 (2016) 275109.

29. W. Hagel, Electrical Conductivity of Li-Substituted Cr_2O_3, J. Appl. Phys. 36 (1965) 2586-2587.

30. T. Dutta, P. Gupta, A. Gupta, J. Narayan, Effect of Li doping in NiO thin films on its transparent and conducting properties and its application in heteroepitaxial pn junctions, J. Appl. Phys. 108 (2010) 083715.

31. M. Qiu, Y. Zhang, Z. Ye, H. He, H. Tang, X. Gu, L. Zhu, B. Zhao, Effect of oxygen pressure on structural and electrical properties of pulsed laser deposition-derived $Zn_{0.95}Mg_{0.05}O$: Li thin films, J. Phys. D: Appl. Phys. 40 (2007) 3229.

32. K. Meziane, A. El Hichou, A. El Hamidi, M. Chhiba, A. Bourial, A. Almaggoussi, Li concentration dependence of structural properties and optical band gap of Li-doped ZnO films, Appl. Phys. A 123 (2017) 430.

33. T. Arnold, D. Payne, A. Bourlange, J. Hu, R. Egdell, L. Piper, L. Colakerol, A. De Masi, P.-A. Glans, T. Learmonth, X-ray spectroscopic study of the electronic structure of $CuCrO_2$, Phys. Rev. B 79 (2009) 075102.

34. T. Yokobori, M. Okawa, K. Konishi, R. Takei, K. Katayama, S. Oozono, T. Shinmura, T. Okuda, H. Wadati, E. Sakai, Electronic structure of the hole-doped delafossite oxides $CuCr_{1-x}Mg_xO_2$, Phys. Rev. B 87 (2013) 195124.

35. A.E. Morales, E.S. Mora, U. Pal, Use of diffuse reflectance spectroscopy for optical characterization of un-supported nanostructures, Rev. Mex. Fis. 53 (2007) 18-22.

36. S. Som, S. Sharma, S. Lochab, Ion induced modification of bandgap and CIE parameters in Y_2O_3: Dy^{3+} phosphor, Ceramics International 39 (2013) 7693-7701.

37. K. Keerthi, B.G. Nair, M.D. Benoy, R. Raphael, R.R. Philip, Properties of transparent conducting quaternary silver indium tin oxide thin films crystallized with delafossite structure, Mater. Chem.phys. 199 (2017) 591-596.

38. C.Taddee, T. Kamwanna, V. Amornkitbamrung, Characterizationof transparent superconductivity Fe-doped $CuCrO_2$ delafossite oxide, Appl. Surf. Sci. 380 (2016) 237-242.

39. S. Tsang, S. So, J. Xu, Application of admittance spectroscopy to evaluate carrier mobility in organic charge transport materials, J. Appl. Phys. 99 (2006) 013706.

40. T. Okuda, N. Jufuku, S. Hidaka, N. Terada, Magnetic, transport, and thermoelectric properties of the delafossite oxides $CuCr_{1-x}Mg_xO_2$ ($0 \leqslant x \leqslant 0.04$), Phys. Rev. B 72 (2005) 144403.

41. D. Li, X. Fang, Z. Deng, W. Dong, R. Tao, S. Zhou, J. Wang, T. Wang, Y. Zhao, X. Zhu, Characteristics of $CuCr_{1-x}Mg_xO_2$ films prepared by pulsed laser deposition, J. Alloy Compd. 486 (2009) 462-467.

42. R. Kumar, N. Khare, Temperature dependence of conduction mechanism of ZnO and Co-doped ZnO thin films, Thin Solid Films 516 (2008) 1302-1307.

6. En route to the Conductivity Bottleneck in *p*-type $CuCr_{1-x}M_xO_{2-y}S_y$ (M = Li, Mg)

Chapter 6

6.1. Introduction:

TCOs are a technologically unique class of compounds endowed with high electrical conductivity and transparency in visible region. This culmination suits the remarkable applications in transparent electronics namely displays, photovoltaics, low emissivity windows etc. [1-3]. Till date, *n*-TCOs have superior carrier mobility and widely used in contemporary electronics in contrast with their *p*-type counterparts. The majority of the transparent semiconducting based materials are n-TCOs. Examples of these *n*-type materials are Al-ZnO, F-SnO_2, and Sn-In_2O_3 [4-6]. The lack of reliable processing methods for p-TCOs has prevented transparent technologies, which practically demanded p-n junctions from progressing. Physically, the major difficulty in achieving effective hole mobility in *p*-TCOs is the localized hole plasma near valence band maxima due to highly electronegative O 2*p* states. The pioneering work by Kawazoe *et al*. [7] on Cu^{1+} based wide gap oxide ($CuAlO_2$) first demonstrated the *p*-type conductivity with optical transparency in visible light. Development took place like transparent transistors, electrical items, including semiconductor diodes cannot be realised because to the inefficiency of relatively high achievement of *p*-TCOs [8, 9]. A series of transparent Cu-based delafossites *p*-TCOs, including $CuMO_2$ (M = Cr, A1, Ga, ln) and $SrCu_2O_2$, were discovered as a consequence of that kind of manifestation [10-13]. Metal-oxide covalently coupling is used to minimise the significant Electrostatic forces generated from oxygen ions within the Cu-delafossite unit. The *p*-type performance of cubic Cu_2O was likewise caused by such a decrease in carrier localized [14]. Cu_2O is still not transparent,

nevertheless inside the visual wavelengths of the spectrum. Cu^{+} atoms can be more densely placed in Cu delafossites compared to those found in Cu_2O, resulting in greater optical energy gap and therefore better transparency. Merely three of something like the $CuMO_2$ delafossite such as $CuGaO_2$, $CuAlO_2$ and $CuInO_2$ has been reported so far. Each of these compounds, the visible spectrum transmits are also still lower than that for their *n*-type equivalents, who typically exhibit highest order transmissions throughout the broad visible range. The multi-layered *p*-type compounds LaCuOCh exhibit greater delocalized *p*-holes when oxygen is replaced by chalcogen (S, Se) ions, as established by Hosono et al. [15, 16]. Additionally, co-doped in Cr_2O_3 was done to increase carrier conductivity with improve optical transparency [17]. The impacts of Ge content upon these physical and also structural characteristics of $CuCrO_2$ have recently been explored [18]. Additionally, Ti-$CuCrO_2$ availability of goods among its optical with electrical characteristics [19].

Consequently, our group have developed [20-22] the scheme of chalcogen (*Ch= S, Se*) doping at O-site and codoping for the generation of delocalized and lighter holes in valence and conduction bands. Subsequent theoretical and experimental follow-ups of other research groups [23] motivate us to overcome the much strived conductivity bottleneck by introducing even lighter holes in a prototype hole exclusive system. In order to describe their doped ions or lattice configuration inside the crystals, we have employed the Kröger–Vink notation throughout the whole article. The Li^{1+} ions positioned now at Cr^{3+} sites with such an associated hole is denoted by the notation $Li_{Cr}^{\bullet\bullet}$, Mg^{2+} ions positioned at Cr^{3+}, denoted by the notation $Mg_{Cr}^{\bullet}$ while the S^{2-} ion located at the O^{2-} site with an associated acceptor state is denoted by the notation $S_O^{\times}$. The materials will now just be labelled as CCO, $CCO/Mg_{Cr}^{\bullet}$, $CCO/Li_{Cr}^{\bullet\bullet}$, $CCO/(Mg_{Cr}^{\bullet} + S_O^{\times})$ and $CCO/(Li_{Cr}^{\bullet\bullet} + S_O^{\times})$ with their cationic and anionic doping.

6.2. Experimental details:

6.2.1. Materials and methods

Single phase $CuCr_{1-x}M_xO_{2-y}S_y$ (M=Mg, Li) is prepared by conventional solid state method [22]. The stoichiometric composition of CuO (Merck), Cr_2O_3 (Sigma-Aldrich), Li_2O (Sigma-Aldrich), MgO (Sigma-Aldrich) and CH_4N_2S (Merck) are used to keeping x and y, 0 or 5 atomic %.

6.2.2. Characterizations

The crystalline phase quality of the powder is assessed by XRD (Bruker D8 Advance) using a Cu K_α radiation (λ = 1.5418 Å) at 300 K. The continual scanning mode ($\theta - 2\theta$) across 20−80° with step interim of 0.02° and scan rate 2s/step is selected for all the samples. The structural analysis using XRD pattern is borne out by Rietveld refinement with FULLPROF programme and using the refined parameters. The diffuse spectral reflectance of all powders is carried out across the wavelength region of 220-2200 nm using Shimadzu UV-Vis 3600 spectrophotometer. The electrical conductivity measurements are achieved by a source meter (KEITHLEY 4200) with the conventional two-probe method under helium atmosphere over the temperature range of 4 – 300 K. The current–voltage (I-V) profiles are acquired by using HIOKI (3522–50) LCR Hi-TESTER at 300 K. *p*-type conduction behaviour is established by the Hall measurement system using the four-probe Van der Pauw configuration with constant magnetic field 0.15 Tesla at 300 K. A high-performance electrically conductive silver paste (Alfa Aesar™ 4407518) was used to make point contacts with a sample at the corner site and they were connected to thin copper wires.

6.3. Results and discussions:

6.3.1. Structural analysis

According to x-ray diffraction technique (Figure 6.1), the prototype delafossite crystalline phase exhibiting rhombohedral lattice symmetry [point group 3m (C_{3v}), space group $R\bar{3}m$ (C_{3v}^{6})] represents the only delafossite phases present in the crystalline phases of the both pure, doped and co-doped samples, confirming their identically. Neither any spectrum is found to contain any further peaks caused by doping. Table 6.1 shows the generated lattice parameters characteristics (a and c), cell volume (V), and crystalline size (D) using Rietveld analysis and Williamson-Hall approach for all prepared materials. It is clear that $S_O^{\times}$ causes to diminish whereas a increase with $Li_{Cr}^{\bullet\bullet}$ doping. In contrast to the pure $CuCrO_2$, although c reduce approximately linearly for doped and co-doped samples. In our earlier work, we provide a detailed explanation of the reduction inside the c –axis [21, 22]. The normalized atomic occupancy of $Mg_{Cr}^{\bullet}$, $Li_{Cr}^{\bullet\bullet}$ and $S_O^{\times}$ are estimated to be 3.13%, 1.28% and 0.615% respectively, in comparison to the estimated 5%. The reduced concentration of $Mg_{Cr}^{\bullet}$, $Li_{Cr}^{\bullet\bullet}$ and $S_O^{\times}$ is attributed to their high evaporation tendency from solid solution. The superposition of observed measurements is displayed alongside the improved XRD spectra (figure 6.1). As a function of peak fitting, the pseudo-Voigt operation is used. Goodness of fit ($\chi^2 = R_{wp}^2/R_{exp}^2$) converges to 1.6 to 1.7, which is reasonable considering the presence of v_{Cu}' and (or) Cr_{Cu}''.

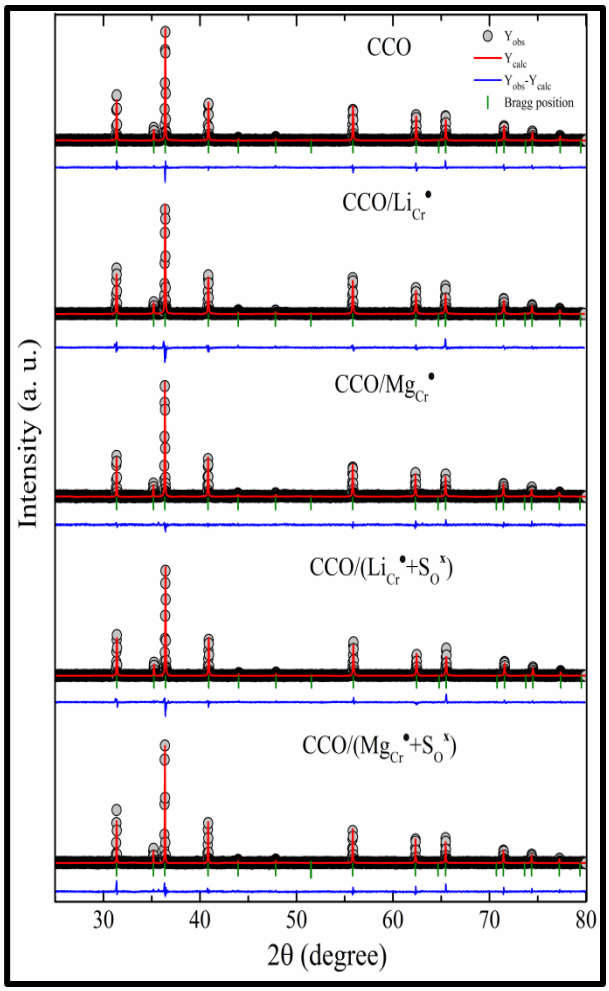

Figure 6.1: x-ray diffraction pattern (black circle) of $CuCr_{1-x}M_xO_{2-y}S_y$. The solid red line corresponds to the best fit profile obtained by Rietveld refinement and the blue line ($Y_{obs} - Y_{calc}$) is the intensity difference between calculations and experimental data. Vertical green lines indicate the position of associated Bragg lines.

Table 6.1: Refined unit cell parameters, cell volume and crystalline size from Rietveld refinement and Williamson-Hall plots for all prepared materials.

Materials	Lattice parameter a=b (Å)	Lattice parameter c (Å)	Cell Volume V (Å^3)	Crystalline Size D (nm)
CCO	2.9741	17.0999	130.98	81.76±3.39
$CCO/Mg_{Cr}^{\bullet}$	2.9755	17.1071	131.17	89.44±4.52
$CCO/Li_{Cr}^{\bullet\bullet}$	2.9748	17.0983	131.07	87.79±3.47
$CCO/S_O^{\times}$	2.9736	17.0961	130.92	74.55±4.00
$CCO/(Li_{Cr}^{\bullet\bullet} + S_O^{\times})$	2.9754	17.0859	131.12	88.71±4.07
$CCO/(Mg_{Cr}^{\bullet} + S_O^{\times})$	2.9768	17.0970	131.20	129.49±5.71

6.3.2. Optical properties

Whenever spectrum are standardized with such a white background sample, such as $BaSO_4$, the Kubelka-Munk (K-M) methodology [24] is used to derive the optical energy gap of the relevant samples using diffuse spectrum reflectance around across the range of wavelength 220–2200 nm. As in the following way, the K-M model can be represented:

$$F(R_\infty) = \frac{(1-R_\infty)^2}{2R_\infty} \ , \qquad (1)$$

Here $F(R_\infty)$ is the so-called K-M function, where $R_\infty = R_{Sample}/R_{BaSO_4}$ the ultimate non-absorbing matrix absolute diffused reflectance of is scattered light from such an indefinitely thin sample surface. By extrapolating the linearly fitting region at $[F(R_\infty)h\nu]^2 = 0$ and plotting $[F(R_\infty)h\nu]^2$ versus $h\nu$, as illustrated in Figure 6.2, the energy gap (E_g) is obtained.

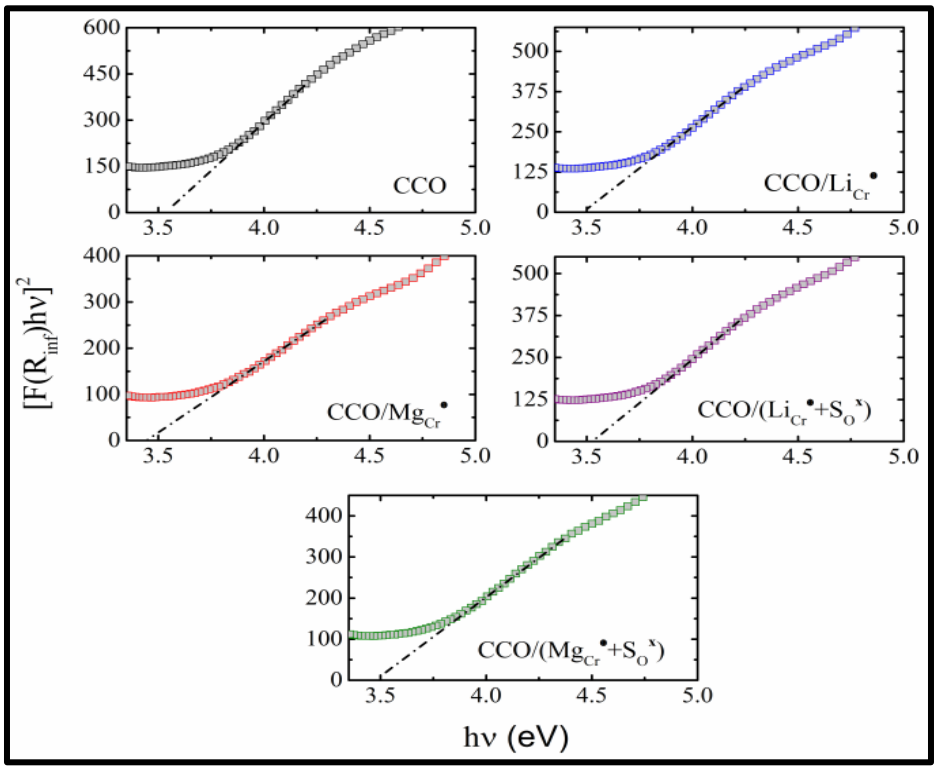

Figure 6.2: DR spectra of $CuCr_{1-x}M_xO_{2-y}S_y$ calculated by Kubelka-Munk function. The x-intercept of extrapolated dotted lines is indicating the associated optical gap.

All synthesis materials band gap values are determined to be well inside the transparent area with broad band gaps [3.52 eV for CCO, 3.50 eV for $CCO/Li_{Cr}^{\bullet\bullet}$, 3.45 eV for $CCO/Mg_{Cr}^{\bullet}$, 3.51 eV for $CCO/(Li_{Cr}^{\bullet\bullet} + S_O^{\times})$ and 3.48 eV for $CCO/(Mg_{Cr}^{\bullet} + S_O^{\times})$]. These are in good accordance well with optical gap computed for $CuCrO_2$ thin films produced from post-annealing [25].

6.3.3. Electrical properties

The electrical conductivity (σ_{dc}) for $CCO/Mg_{Cr}^{\bullet}$, $CCO/Li_{Cr}^{\bullet\bullet}$, $CCO/(Mg_{Cr}^{\bullet} + S_O^{\times})$ and $CCO/(Li_{Cr}^{\bullet\bullet} + S_O^{\times})$ throughout the range of temperature (80 – 300 K) appears in Figure 6.3. Upon codoping, the associated material exhibits almost two times higher conductivity than its cationic doped counterpart. The magnitudes of σ_{dc} at 300K are found to be 0.045, 0.019, 0.022 and 0.005 S/cm for $CCO/(Mg_{Cr}^{\bullet} + S_O^{\times})$, $CCO/(Li_{Cr}^{\bullet\bullet} + S_O^{\times})$, $CCO/Mg_{Cr}^{\bullet}$ and $CCO/Li_{Cr}^{\bullet\bullet}$ respectively.

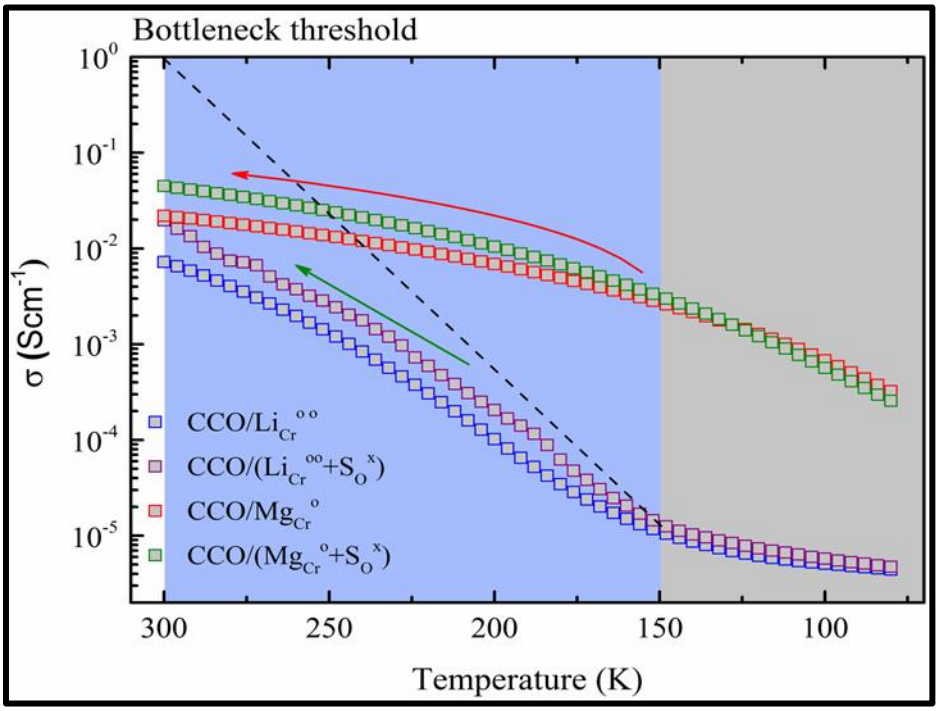

Figure 6.3: σ_{dc} vs. T for $CuCr_{1-x}M_xO_{2-y}S_y$

The Hall coefficient of both doped and also co-doped samples seems to have a positive sign, indicating p-type conduction, and some other associated variables are displayed in Table 6.2. Carefully observation of Figure 6.3 (σ_{dc} versus T) reveals a trend of conductivity saturation (red arrow) in $CuCr_{1-x}M_xO_{2-y}S_y$, limited by impurity scattering. This is in accordance with the decrease

in Hall mobility upon ($Mg_{Cr}^{\bullet} + S_O^{\times}$) doping. But the steady increase in σ_{dc} above 150 K for CCO/ ($Li_{Cr}^{\bullet\bullet} + S_O^{\times}$) (green arrow) is associated with smaller activation. The E_a and hole mobility values are tabulated in Table 6.2 for all doped and co-doped materials.

Table 6.2: Transport parameters are obtained from Arrhenius and Hall measurements at 300K.

Materials	E_a meV	σ_{dc} (S/cm)	R_H (cm^3C^{-1})	n (cm^{-3})	μ_{dc} ($cm^2V^{-1}s^{-1}$)
$CCO/Mg_{Cr}^{\bullet}$	54.7	0.022	2.8×10^3	2.23×10^{15}	61.66
$CCO/Li_{Cr}^{\bullet\bullet}$	219.4	0.005	13.11×10^3	4.77×10^{14}	65.51
$CCO/(Li_{Cr}^{\bullet\bullet} + S_O^{\times})$	226.6	0.020	1.17×10^3	5.32×10^{15}	23.50
$CCO/(Mg_{Cr}^{\bullet} + S_O^{\times})$	68	0.045	360	1.73×10^{16}	16.26

6.3.4. Admittance analysis

Following co-doping, the significant downshift of such admittance peaks with in the dispersion of frequency CCO (74.754MHz), $CCO/Mg_{Cr}^{\bullet}$ (8.801), $CCO/S_O^{\times}$ (7.363 MHz), $CCO/Li_{Cr}^{\bullet\bullet}$ (6.347 MHz) and $CCO/(Li_{Cr}^{\bullet\bullet} + S_O^{\times})$ (5.470 MHz), $CCO/(Mg_{Cr}^{\bullet} + S_O^{\times})$ (4.312 MHz) is appears in Figure 6.4a. As a consequence, the occurrence of collisions between charge carriers similarly rises, which leads to the peaks shift downward. The maximized admittance peaks value approaches 0.8 S for $CCO/(Mg_{Cr}^{\bullet} + S_O^{\times})$ due to increased carrier concentration, which compared to other samples.

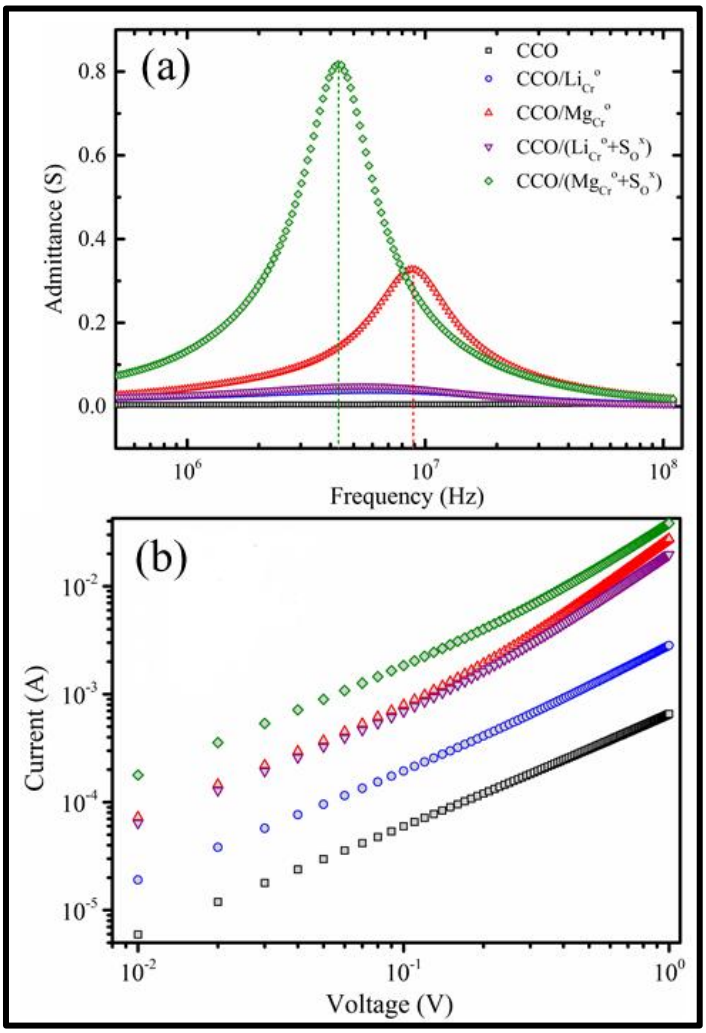

Figure 6.4: (a) Admittance spectra of $CuCr_{1-x}M_xO_{2-y}S_y$ (b) Log – log representation of current–voltage characteristics of the corresponding materials.

Because of increased carrier scattered brought on by defects caused around by polycrystallinity, a shorter screening length for smaller frequencies indicates reduced hole mobility. Figure 6.4b demonstrates the (I− V) relationships across all materials that exhibits for $CCO/(Mg_{Cr}^{\bullet} + S_O^{\times})$ comparing to pure CCO, the current is noticed to be increased by ten times or more. Additionally, co-doped can be seen to cause a steeper rise in current, which indicates a reduction inside the materials resistivity.

6.4. Conclusions:

In general, a proposition for generating light hole states in group IIIA *p*-TCO delafossite is presented upon valence band engineering of $CuCrO_2$ by doping with $Mg_{Cr}^{\bullet}$, $Li_{Cr}^{\bullet\bullet}$ and $S_O^{\times}$ induced holes. The diffuse reflectance (DR) spectra are acquired to determine the dominant optical gap (~ 3.5 eV) and found to be affected little upon site selective hole doping. From temperature dependence (80 – 300 K) of DC conductivity (σ_{dc}), ($Li_{Cr}^{\bullet\bullet} + S_O^{\times}$) doping can be identified to be the more plausible alternative to reach the bottleneck threshold compared to ($Mg_{Cr}^{\bullet} + S_O^{\times}$) albeit of smaller σ_{dc} at 300 K. Delocalization of lighter holes is evidenced from temperature dependence of DC electrical conductivity. Upon achieving the desired solubility of $Li_{Cr}^{\bullet\bullet}$ and $S_O^{\times}$, we are soon expecting to realize, if not overcome, the conduction bottleneck.

6.5. References:

1. Y. Yang, L. Wang, H. Yan, S. Jin, T.J. Marks, S.Y. Li, Appl. Phys. Lett. 89 (2006) 051116.

2. M. Emziane, K. Durose, D.P. Halliday, A. Bosio, N. Romeo, Appl. Phys. Lett. 87 (2005) 251913.

3. D. Ginley, T. Coutts, J. Perkins, D. Young, X. Li, P. Parilla, MRS Proc. (2001) 668.

4. C.G. Granqvist, A. Hultaker, Thin Solid Films 411 (2002) 1.

5. K.L. Chopra, S. Major, D.K. Pandya, Thin Solid Films 102 (1983) 1.

6. T.V. Thu, S. Maenosono, J. Appl. Phys. 107 (2010) 014308.

7. H. Kawazoe, H. Yasakuwa, H. Hyodo, M. Kurita, H. Yanagi and H. Hosono, Nature 389, 939 (1997).

8. A. Banerjee, K. Chattopadhyay, Prog. Cryst. Growth Char. Mater. 50 (2005) 52 – 105.

9. E. Fortunato, P. Barquinha, R. Martins, Adv. Mater. 24 (2012) 2945 – 2986.

10. H. Kawazoe, M. Yasukawa, H. Hyodo, M. Kurita, H. Yanagi, and H. Hosono, Nature (London) 389, 939 (1997).

11. S.K. Ueda, T. Hase, H. Yanagi, H. Kawazoe, H. Hosono, H. Ohta, M. Orita, and M. Hirano, J. Appl. Phys. 89, 1790 (2001).

12. H. Yangi, T. Hase, S. Ibuki, K. Ueda, and H. Hosono, Appl. Phys. Lett. 78, 1583 (2001).

13. A. Kudo, H. Yanagi, K. Ueda, H. Hosono, and H. Kawazoe, Appl. Phys. Lett. 73, 220 (1998).

14. Kleinman and K. Mednick, Phys. Rev. B 21, 1549 (1980).

15. K. Ueda, S. Inoue, S. Hirose, H. Kawazoe, H. Hosono, Appl. Phys. Lett. 77 (2000) 2701 – 2703.

16. H. Hiramatsu, K. Ueda, H. Ohta, M. Hirano, T. Kamiya, H. Hosono,Appl. Phys. Lett. 82 (2003) 1048 – 1050.

17. E. Arca, K. Fleischer, I. Shvets, Appl. Phys. Lett. 99 (2011), 111910.

18. P. Rattanathrum, C. Taddee, N. Chanlek, P. Thongbai, T. Kamwanna, Ceram. Int. 43 (2017) S417 – S422.

19. M. Majee, P. Bhobe, U. Deshpande, A. Nigam, J. Appl. Phys. 122 (2017), 225111.

20. N. Mazumder, D. Sen and K. K. Chattopadhyay, AIP Conf. Proc. 1512, 1060 (2013).

21. N. Mazumder, D. Sen, U. K. Ghorai, R. Roy, S. Saha, N. S. Das and K. K. Chattopadhyay, J. Phys. Chem. Lett. 4, 3539 (2013).

22. P. Mandal, N. Mazumder, S. Saha, U. K. Ghorai, R. Roy, G. C. Das, and K. K. Chattopadhyay, J. Phys. D: Appl. Phys. 49, 275109 (2016).

23. Q. J. Liu, Z. Jiao, F. S. Liu and Z. T. Liu, Phys. Chem. Chem. Phys. 18, 14317, (2016).

24. A.E. Morales, E.S. Mora, U. Pal, Rev. Mex. Fis. 53 (2007) 18-22.

25. H Y Chen, W J Yang and K P Chang 2012 Appl. Surf. Sci. **258** 8775.

7. Investigation of the transport and structural properties of nanocrystalline delafossite *p*-$CuAlO_2$

Chapter 7

7.1. Introduction:

Transparent semiconductors are particularly significant for numerous types of technologies and are frequently utilised on transparent electronics. TCOs are remarkable in many application areas, such as touch screens, LCD, photovoltaic devices, LED etc. due to their combination of minimal electrical resistivity with strong transparency within the visible regime [1-4]. Nearly each of the materials made with transparent semiconductors are *n*-TCOs. These *n*-type compounds include, for instance, F-SnO_2 (FTO), Al-ZnO (AZO) and Sn-In_2O_3 (ITO) [5-7]. Transparent devices, which effectively required *p-n* junctions, have been unable to advance due to the lack of credible preparation techniques for *p*-TCOs. Since Hosono and others first discovered $CuAlO_2$ in 1997, it has become considered like a *p*- semiconductors as well as prospective *p*-TCO [8, 9]. $CuAlO_2$ can be employed to create *p*-TCOs films, which can then be utilised to create transparent optoelectronics components including *p-n* diodes along with transistors. $CuAlO_2$ films have been thoroughly investigated recently, including its manufacture, structure, or characteristics [10, 11]. Specifically, the studies also on characteristics for $CuAlO_2$ films like field emission, photovoltaic effects and gas-sensitive of ozone indicating as $CuAlO_2$ is evolving into a key component of the multipurpose *p*-semiconductors [12-15]. $CuAlO_2$ films can now be made using a variety of techniques, including PLD, PECVD, sol-gel, spray pyrolysis and sputtering [16-18]. The huge application and fabrication of microelectronics could be performed through RF-sputtering.$CuAlO_2$ film performances are regulated with deposited factors like substrate temperature, gas pressure etc. [19, 20]. The developments of $CuAlO_2$ films may be limited

moreover, due to some less impacts of thickness about their characteristics. That's because of optical transparency along with electric transport characteristics of TCO films might be significantly impacted by changes inside the micro-structural and morphologies of the films [21].

$CuAlO_2$ has recently gained interest in the areas of thermoelectric applications and catalysts that produce H_2 when exposed to visible range [22]. Traditionally, $CuAlO_2$ was created by performing a solid state heating at 1050 ^{0}C of $Al(OH)_3$ and Cu_2O in a vacuum [23]. Al_2O_3 and CuO powder were heated at 1100 ^{0}C during 40 hours in open atmosphere with multiple re-grinding steps, and then a chemical interactions from the composition discovered as well [24]. Using a combination (Cu_2O: Al_2O_3) inside a NaOH solution around 500 ^{0}C seems to be a traditional hydrothermal procedure [25]. The chemical processes temps decrease to 400 ^{0}C, whenever a comparable process begins with (CuCl: $NaAlO_2$) mixture [26]. This was also observed that CuO_x melted was penetrated at such the temperature of 1200 ^{0}C with compacts of α-Al_2O_3 [27]. A convincing reduction with in temperature range below at 360 ^{0}C was shown in the presence of melted NaOH, in comparison to the standard solid state approach, starting point for the development reactivity of $NaAlO_2$ [28]. $CuAlO_2$ bulk and also Cu_2O or CuO were synthesised as single crystals at temperatures range (1050-1200 °C) [23]. $CuAlO_2$-Cu_2O has such a comparatively small eutectic temperature at around 1130 ^{0}C, which makes it challenging to synthesise phase purity of $CuAlO_2$. An extreme propensity for oxidizing conversion of (Cu^+-Cu^{2+}) ions as another challenging process, because it decomposes rather than produces only single phases of bulk $CuAlO_2$. Additionally, Cu^+ ions are frequently volatilized during highly temperature production of $CuAlO_2$, which results in the creation spinel phase of $CuAl_2O_4$ [29].

High-energy (ball)-milling (HEBM) offers a significant advantage over many other traditional techniques when looking for activating chemical methods at low temperature. This basic technique

may also be utilised to create nanocrystalline functional compounds with predefined size of particles [30]. In addition to creating numerous structural defects with derangement, a strong pulse emerged at the forefront of an impacts waveform under those strong pressure gradients also induces heat flux development as well as a mechanical alloying response [31]. Mechanical alloying procedures and also mechanical excitation are indeed the generic terms used to describe these solids mechanically induced chemical and also physical effects. Numerous technologically significant complicated oxide materials, such as $BaTiO_3$, Zn_2SnO_4, $NiFe_2O_4$, $ZnFe_2O_4$ and others have been synthesised using the mechano-chemical technique [32, 33]. The convenient one-steps low temps synthesized of $CuAlO_2$ originating from such a mechano-chemical stimulated mixtures (Cu_2O-Al_2O_3) has not yet been described, despite the fact that numerous significant studies have also been performed to generate or analyse phase purity $CuAlO_2$ [34, 35].

There is an alternate viewpoint for the current study that is method-oriented. Because of $CuAlO_2$ wide variety of applications, a numerous of studies have already been generated about its optoelectronic character. Additionally, it is widely acknowledged that these characteristics closely connect to its magnetic characteristics, in particular in terms of a small departure from the ideal stoichiometric ratio or partially cation substitute. Prior to this, our group created a strategy for chalcogen doped at O-site in *p*-$CuAlO_2$ and simultaneously cationic-anionic doping due to more delocalized holes in $CuCrO_2$ with the goal of improving optical along with transport properties [36-38]. In this article, we have examined how changing the effects of grain size in the structural and transport characteristics of nanocrystalline *p*-$CuAlO_2$ via conventional ball-milling approach.

7.2. Experimental details:

7.2.1. Materials and methods

The $CuAlO_2$ microcrystalline or nanocrystalline materials utilized in this study were produced to use the traditional solid-state sintering process with stoichiometric mixture of Cu_2O and Al_2O_3 (Sigma-Aldrich); which involves numerous milling and heating processes using a stoichiometric ratio of both the precursor powders Al_2O_3 and Cu_2O at 1200 ^{0}C for 15h and heated in air. The powders synthesized via the solid-state process were mechanically milled for 4h, 8h 12h and 20 h respectively in way to minimize the particle size. The milling operation was conducted in a planetary ball-mill (Fristch pulverisette 7) employing Tungsten Carbide (WC) balls with a speed of 300 rpm. The volume ratio was (1:20) for both powder and ball. These WC balls had respective weights of 8 g and 0.99 g.

7.2.2. Characterization

By employing the XRD (Bruker D8 Advance) and a CuK_α (λ= 1.5418 Å) at 300 K, the crystallinity purity of the material is evaluated. All the materials are run in continuous scanning mode ($\theta - 2\theta$) over ($20-80^0$) with such a step interval of 0.02^0 or a scanning speed of 2 s/steps. The Rietveld refinements only with the programme (FULLPROF) and utilising the modified parameters verify the structural design by employing the XRD results. The milling operation was conducted in a planetary ball-mill (Fristch pulverisette 7) employing Tungsten Carbide (WC) balls at the speed of 300 rpm. With the assistance of a spectrophotometer (Shimadzu UV-Vis 3600), all sample having their DR spectrum measured over the wavelength regime (220–2200 nm). Using transmission electron microscope (TEM: JEOL JEM-2100), the size or nano crystalline crystal structures were

examined. The FESEM (S-4800 Hitachi) was utilized to examine materials morphology. The Agilent (4294A) highly precise impedance analyser operating (300 K) is employed to study admittance characteristics over the frequencies ranging from 40 Hz to 110 MHz with an applied dc-biased 2 V. A source tester (KEITHLEY - 4200) is used to determine electrical properties over through the range of temperature (80 - 300 K) while using the standard two-probe techniques in a helium environment. The Hi-TESTER (3522 - 50) HIOKI LCR meter is used to obtain the (I - V) characteristics (300 K). The Hall measuring method, which employs the four points probe (Van-der- Pauw) designing with a steady magnetic field of 0.15 T (300 K), confirms the nature of *p*-type conductivity. Making pointed connections with such a materials and joining them to thin Cu-wires required the utilization of highly conductive silver Alfa (4407518- Aesar^{TM}) paste.

7.3. Results and discussions:

7.3.1. Structural properties

The prepared *MICRO* and *NANO* samples (JCPDS: 76-2398) of the single crystalline phase (Figure 7.1a) is deduced from the acquired powder diffraction peaks. However, there is currently no indication that any secondary phases generation occurs in all materials. The diffraction patterns are created to be compatible with delafossite structure (group-III) having rhombohedral space group [$R\bar{3}m$ (166)]. The lattice parameters, lattice strain and cell volume obtained from XRD patterns and are illustrated in Table 7.1. The material was sintering at temperature (1200 ^{0}C), as indicated by the prominent peaks with in XRD spectra, which indicate a microcrystalline material. Consequently, longer milling durations resulted in a reduction in crystallinity. According to the anticipated reduced

grain size during in the milling operation, the XRD spectra reliance on milling time [see inset in Figure 7.1a] reveals a continual peak broadening. Afterwards 12 h of milling, the XRD peaks widened, proving that nano-sized $CuAlO_2$ is formed as a result of the process. It was found that while milling duration is extended, intensity of XRD peaks is significantly reduced.

.

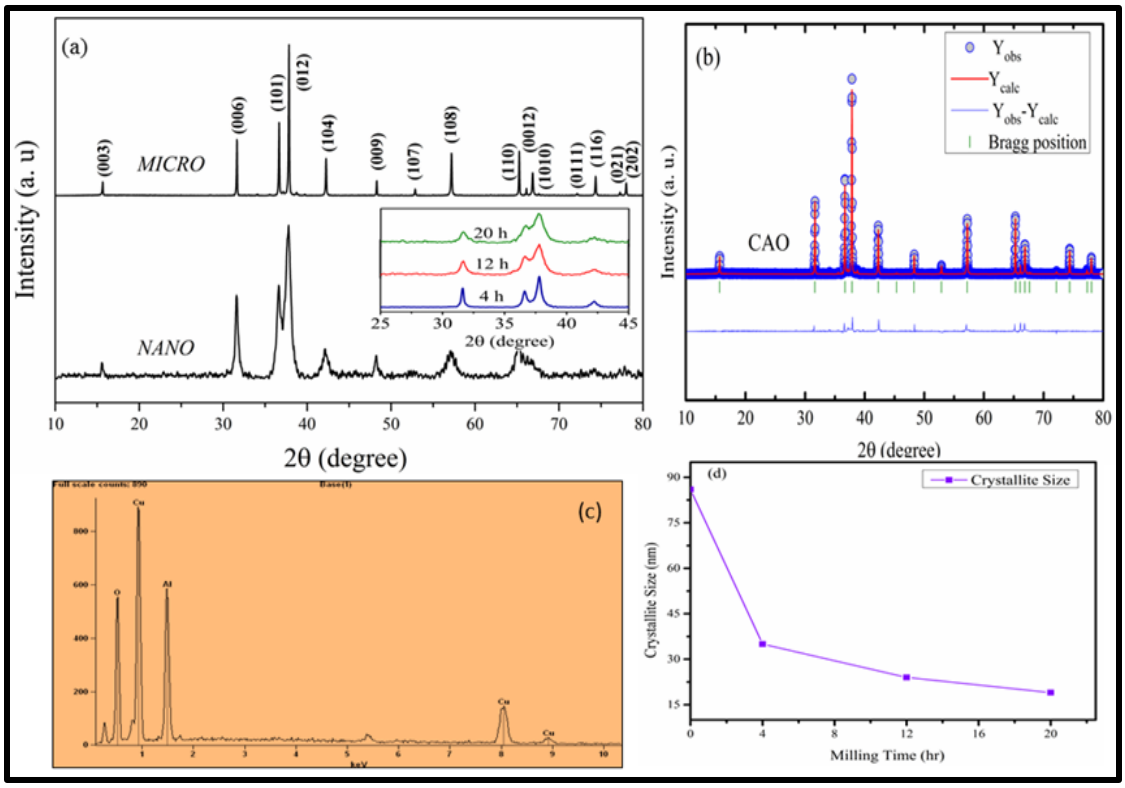

Figure 7.1: (a) Evaluating the differences between the XRD patterns of microcrystalline and also nanocrystalline materials. The inset displays the advancement of milling methods for 4, 12, and 20 h. (b) The XRD pattern for the *MICRO* material. The intensity differences among experimental results with Rietveld analysis is shown by Y_{obs} - Y_{calc}, and also the solid red line refers to the pattern generated from of the Rietveld analysis. (c) Using EDX measurements, the elemental composition was determined for nanocrystalline $CuAlO_2$ (d) crystalline size variation with milling time for *NANO* samples.

Table 7.1: Unit cell parameters, cell volume and strain for all the synthesized materials obtained from XRD analysis.

Materials	Lattice parameter a=b (Å)	Lattice parameter c (Å)	Cell Volume V_0 (Å^3)	Effective lattice strain η (%)
CAO	2.857	16.941	79.885	0.082±0.002
CAO:4 h	2.862	16.952	79.890	0.312±0.020
CAO:12 h	2.865	16.957	79.892	0.297±0.062
CAO: 20 h	2.868	16.959	79.897	0.048±0.036

Therefore, for up to 20 hours of milling, no extra peaks signifying any significant phases have been seen, implying the actual products were highly pure. The (0 1 2) peak intensity of the $CuAlO_2$ phase is significantly widened during ball milling, according to the XRD spectra of such 4-20 h of milling, indicating the nano-crystalline phasing forms as a response of milling process. It is observed that milling time causes crystalline size of the materials to diminish. After 4 h of milling, the $CuAlO_2$ lattice strain firstly increase to 0.31% then reduces to 0.048% after 20 h. In accordance with Debye-Scherrer's formula, the average crystalline sizes listed in Table 7.2 are figured out as follows [39]:

$$D = \frac{0.9\lambda}{\beta cos\theta}, \qquad (1)$$

Here D is the average crystalline size, θ is the Bragg angle, λ is the wavelength of X-ray, and β is the FWHM of diffraction peak connected to the (0 1 2) plane. It is obvious from this list (Table 7.2) that such CuAlO2 crystallite size initially reduces more quickly during initially milling periods, and

afterwards decreases relatively slowly until it finally reaches a size of 20 nm throughout milling process, which illustrated in Figure 7.1d.

Table 7.2: Calculated particle size for prepared samples

Materials	Miller Plane(hkl)	Particle Size (in nm)
CAO	012	86
CAO:4 h	012	35
CAO:12 h	012	28
CAO: 20 h	012	20

It's important to notice that throughout milling, the lattice parameters are also shown (Table 7.1) to increases. This suggests that because a rise inside the lattice parameter is caused by a relaxation of the crystalline structure to nanoscale morphologies. In order to replicate the Brag peak configuration, the pseudo-Voigt peaks mechanism is used in association with the quantitatively Rietveld method (Figure 7.1b) related to the *MICRO* compound. The goodness of fitting ($\chi^2 = R_{wp}^2/R_{exp}^2$) corresponds to 1.42. Using energy dispersive x-ray spectra (EDX), the bulk compositional % of nanocrystalline $CuAlO_2$ is examined. According to Figure 7.1c, Cu and Al have globally atomic percentages are (23.77 ± 3.05) and (23.56 ± 1.01)%, respectively for 20 h. According to Table 7.3, the Cu/Al ratio of 1.51 indicates that *MICRO* $CuAlO_2$ could be slightly out

of stoichiometry due to an excessive amount of Cu^{+} [40]. Compared to the *MICRO* sample, the *NANO* samples exhibit enhanced stoichiometry with a Cu/Al ratio of 0.92 to 1.01.

Table 7.3: Cu/Al ratio of size variant $CuAlO_2$

Materials	Cu/Al ratio
CAO	1.512
CAO:4 h	0.995
CAO:12 h	0.923
CAO: 20 h	1.008

The milling effects and generation of nano-phases were also verified by HR-transmission electron microscopy (HRTEM). Figure 7.2a displays a typical HRTEM Figure of 20-hour BM $CuAlO_2$ powders. This from, it can be determined that the as-milled materials typical particle size is around 23 nm. The $CuAlO_2$ delafossite phase is recognized by the corresponding selected area electron diffraction (SAED) pattern, which is displayed in Figure 7.2b&c. Although the bright circular spot not exactly single-crystalline, the materials have excellent crystalline nature, which is advantageous for examining crystals rearrangement. The HRTEM image displays a distinct lattice fringes region having interplanar spacings of around 0.257 nm, which are consistent with delafossite $CuAlO_2$ accepted value [41]. In accordance with the XRD spectra, the above described lattice spacings are in alignment with the (0 1 2) plane of a $CuAlO_2$ crystal inside the rhombohedral phases. An obvious nanometric grainy microstructure along with resolution of lattice could be observed on the HRTEM. Average grain sizes range from 20 to 28 nm with no appreciable through thickness variances are seen. The grains are clearly incredibly disoriented from one another, as

could be shown by viewing over their lattice graphics. The HREM analysis throughout these studies suggests that $CuAlO_2$ generated mostly by high intensity BM technique is composed of small crystal lattice with various crystalline alignments that are divided by the grain boundaries. Average region as in HRTEM photograph, with numerous grain boundaries and also grain. Lattice edges close to such grain boundary appear to be slightly deformed, which suggests that the localized strain there.

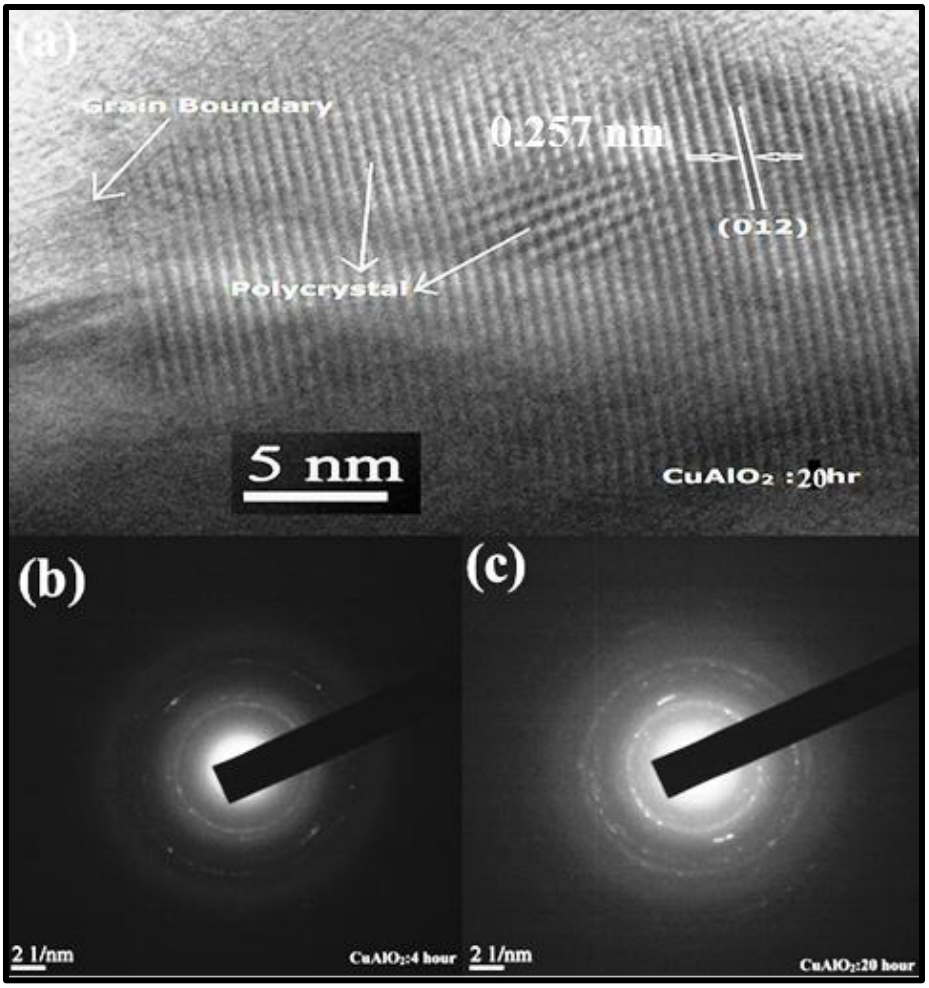

Figure 7.2: (a) HRTEM image of nanocrystalline $CuAlO_2$ for 20 h BM, (b) SAED pattern for 4 h BM, and (c) SAED pattern for 20 h BM.

A typical surface morphology (SEM) image of delafossite $CuAlO_2$ samples prepared by the solid state heating method is shown in Figure 7.3. The SEM photograph of solid $CuAlO_2$ demonstrates the existence on microsized particle with arbitrary shape in such a simple manner. The SEM pictures reveal a steady rise there in existence of nanocrystalline $CuAlO_2$, which means that even milling time is increased, size of the particles decreases in accordance. According to Figure 7.3a, elongated grains were generated during in the heating process.

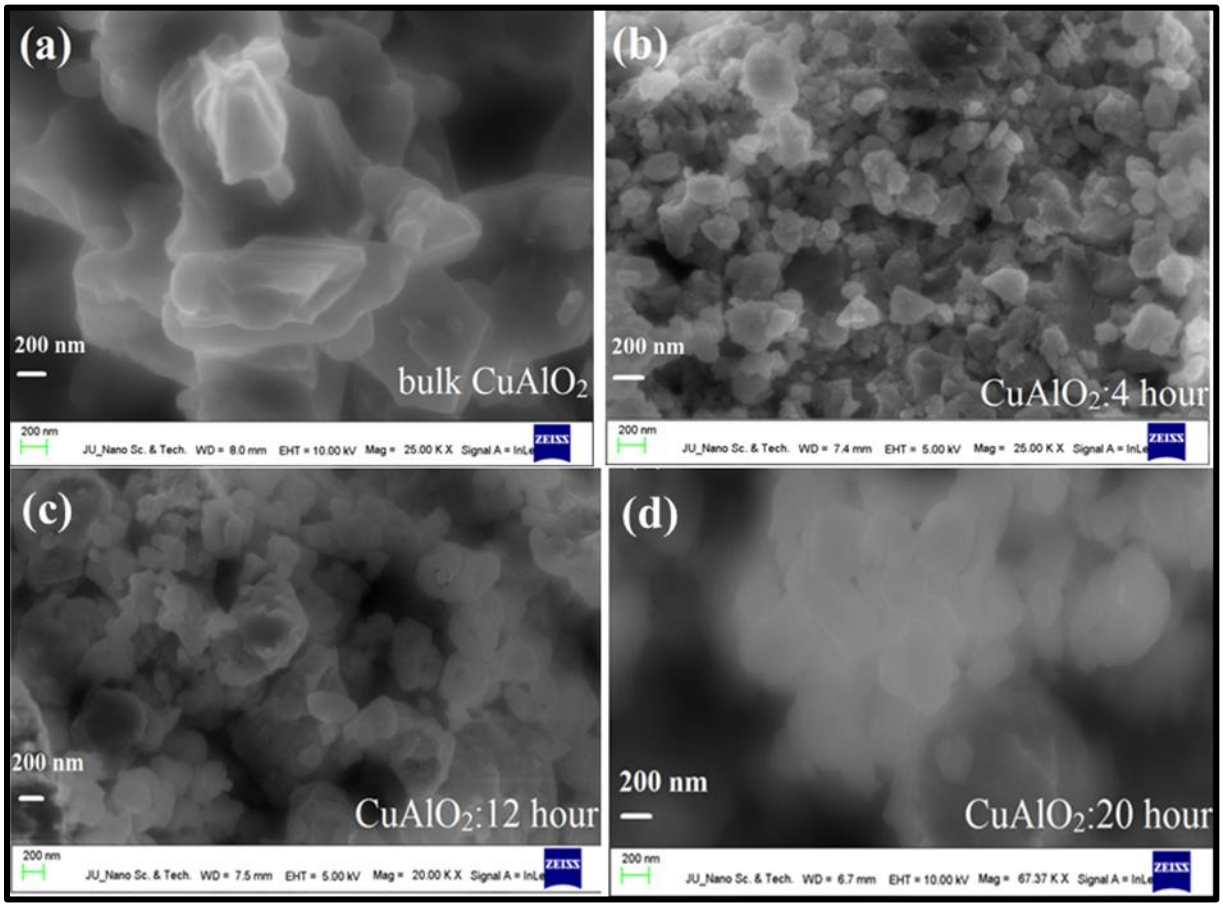

Figure 7.3: Morphology of (a) *MICRO*- $CuAlO_2$ (b) *NANO*-$CuAlO_2$:4 hour (c) $CuAlO_2$:12 hours (d) $CuAlO_2$:20 hour obtained from Scanning electron microscope.

Therefore, the grain arrangement is arbitrary. Because of the anisotropy nature of $CuAlO_2$, this exerts a detrimental effect in electrical conductivity [42, 43]. Because when density at grain boundaries rises due to an increase in the amount of nanostructured particles, numerous trapping but rather recombination centres are introduced [Figure 7.3(b-d)]. It was observed that the agglomerated morphology of the $CuAlO_2$ powder after 20 hours of ball milling seemed to have a consistent microstructure. As-made nanosized polycrystals are shown to have lower electrical conductivity than *MICRO* $CuAlO_2$.

7.3.2. Optical properties

Using diffuse spectrum reflectance over the range of wavelength (220–2200 nm) and matched spectrum with just a white primary source, $BaSO_4$, the Kubelka-Munk (K-M) approach [44] is used to establish the optical spectrum gap of such relevant samples. As in following way, the K-M equation can be represented:

$$(R_\infty) = \frac{(1-R_\infty)^2}{2R_\infty}, \qquad (2)$$

The named K-M function is represented here by $F(R_\infty)$,wherein $R_\infty = R_{Sample}/R_{BaSO_4}$seems to be the diffuse absolute reflectance that light scattered from such an infinitely thin layered sample towards the pristine non-absorbing matrices. The band energy gap (E_g) form all doped and co-doped materials are calculated by extrapolation from the linearly fitting section at $[F(R_\infty)h\nu]^2 = 0$ with such a curve along $[F(R_\infty)h\nu]^2$ versus$h\nu$, as illustrated in Figure 7.4. It was found that the *MICRO*- $CuAlO_2$ direct optical spectrum gap would be around 3.75 eV.

Thereafter milling method *NANO*-$CuAlO_2$, optical gaps are found around 3.77 to 3.79 eV at (4−20 h), which also is consistent previous publication [45]. Whenever the grain size of $CuAlO_2$ is lessened, the band gap throughout the reflectance spectrum measurement continually rises.

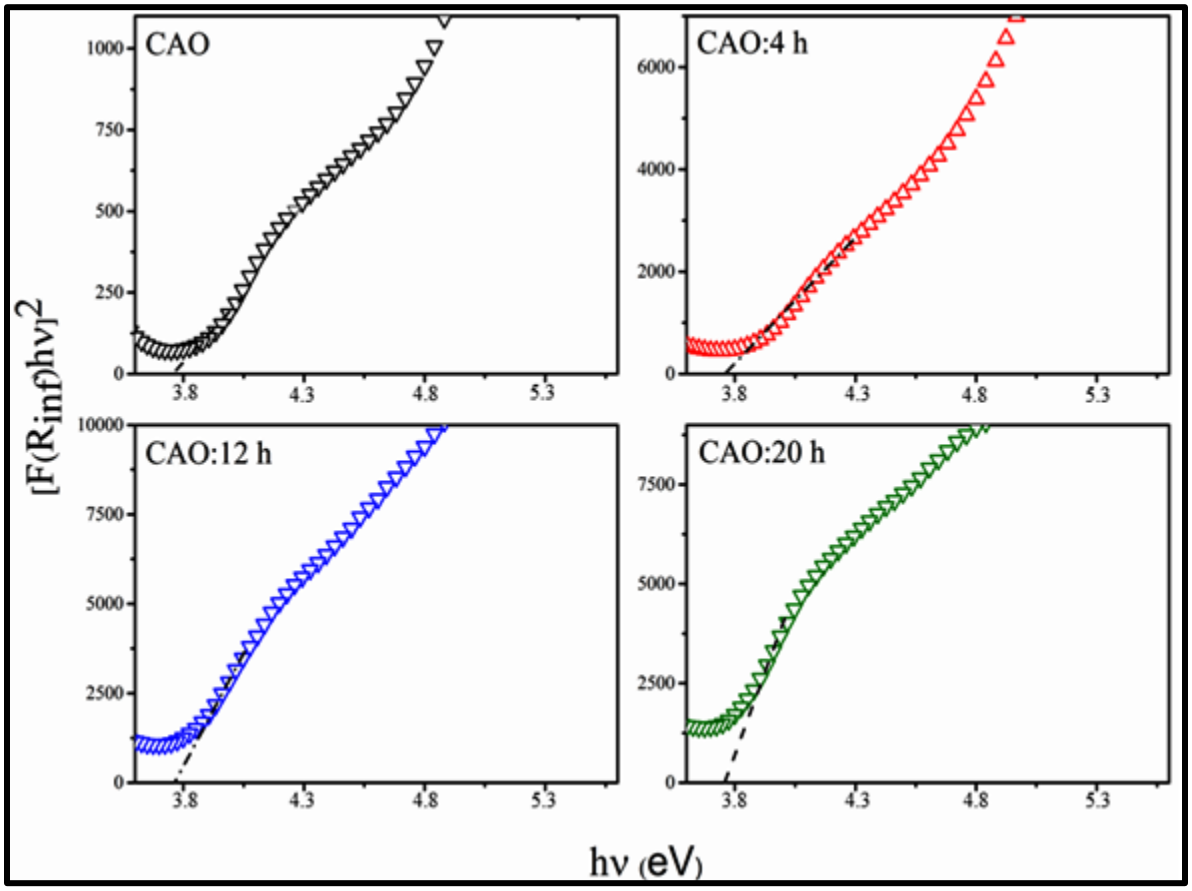

Figure 7.4: Diffuse-reflectance spectrum for all synthesized materials

7.3.3. Electrical properties

Figure 7.5a shows how the electrical conductivity (σ_{dc}) of *MICRO*-$CuAlO_2$ and *NANO*-$CuAlO_2$ (20 h) varies with temperature throughout a range (80 – 300 K). These findings indicate that *MICRO*-$CuAlO_2$ seems to have a conductivity that is five times larger than its *NANO* counterpart at room temperature. It is observed that σ_{dc} exhibits values of 0.41 S-cm^{-1} and 0.076 S-cm^{-1} at 300 K for *MICRO* and *NANO* $CuAlO_2$, respectively. For all synthesised materials, its Hall coefficient with such a positive sign is achieved, indicating *p*-type conduction, and other associated data are shown in Table 7.4.

Table 7.4: Transport parameters for micro and nano-scale materials determined via Arrhenius curves and Hall observations

Materials	σ_{dc} (S/cm)	E_a (meV) (150K-300K)	R_H (cm^{3}C^{-1})	n (cm^{-3})	μ_{dc} (cm^{2}V^{-1}S^{-1})
MICRO	0.41	285	+55.5	1.23×10^{17}	20.84
NANO	0.076	255	+ 75.3	1.89×10^{16}	25.13

The clear relation among $T\sigma$ and 1000/T for such range of temperature (150 - 300K) for *MICRO* and *NANO*-scale materials appears in Figure 7.5a. However, since polaronic charge carriers dominating electrical conduction, the measured temperature relationship is consistent with the predicted one [46]. Indeed the conduction that is thermally activated and conductivity (σ_{dc}) have the following relationships:

$$T\sigma_{dc}(T) = \sigma_0 \exp(-E_a/K_B T), \qquad (3)$$

Hence, E_a, T and k_B are now the activation energies, absolute temperature, and Boltzmann's constant, respectively. In accordance with the slope of both best line fittings for *MICRO* and *NANO* sample, the E_a values are determined to be 285 meV and 255 meV. Furthermore, E_a values agree well with other researcher [47]. The amount of E_a values indicates that such acceptor thermally activates the charge transport within the valence band.

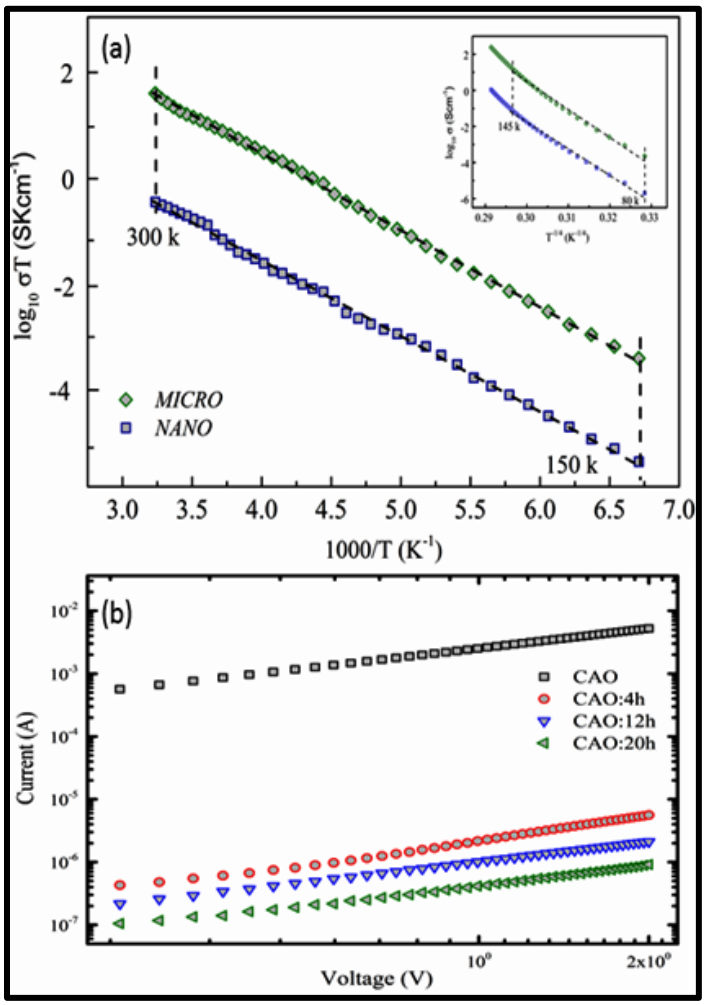

Figure 7.5: (a) Temperature dependent (150-300 K) DC Arrhenius plots for *MICRO* and *NANO*-$CuAlO_2$ (20 h). The lower temperature region (80-145 K) plot fitted with Mott's VRH conduction mechanism (inset). (b) log – log Characteristics of I-V plot for all prepared materials.

Moreover, as demonstrated in Figure 7.5a inset, there is not a linear relation among $T\sigma$ and 1000/T, whenever the temperature becomes less than 145 K for *MICRO* and *NANO* samples. Instead, the 3D-Mott's variable-range hopping (VRH) conduction system is found to be in agreement with the σ_{dc} between both samples over 80–145 K range. Through using model, one can adequately describe electrical conductivity with this range [48, 49].

$$\sigma_{dc}(T) = \sigma_0 \exp\left[-\left(\frac{T_0}{T}\right)^{1/4}\right], \qquad (4)$$

Where T_0 and σ_0 are the characteristic Mott's temperature and pre-factor. Figure 7.5a inset displays the linear fittings for both $\sigma_{dc}(T)$ versus $T^{-1/4}$ plot for *MICRO* and *NANO* samples. The prevalence of holes hopping at temperatures (<145 K) lower thermally activated energy suggests that 3D carriers transport dominates the charge conduction approach. The presence of carrier concentration (1.23×10^{17} cm^{-3}) raises the value of *MICRO* samples by an order of magnitude compared with *NANO* samples. The charge carriers can scatter across numerous defects regions in polycrystalline materials. Due to this, *MICRO* samples have a larger conductivity value than *NANO* samples, but a lesser mobility (20.84 $cm^2V^{-1}S^{-1}$). Figure 7.5b exhibits the (I− V) characteristics for all the synthesized materials are consistent with those of conductivity, as the current increases much more for *MICRO* samples compared to other *NANO* materials (4−20 h).

7.3.4. Dielectric properties

The advantages both capacitance and current methods are combined in admittance spectroscopy. When compared to *MICRO* $CuAlO_2$, nanocrystalline samples admittance like a frequency-dependent function is significantly lesser appears in Figure 7.6. Throughout the measured frequency

spectrum, there aren't any admittance maxima for the sized variant nanocrystalline $CuAlO_2$. Since admittance seems to be the inverse of impedance (Y = 1/Z), we emphasize also that development of defects near grain boundaries, which serve like a trapping and recombination sites, is the reason of the reduction in hole concentrations. Because there are more trapping centres due to the larger concentration of grain boundaries in nanocrystalline polycrystalline materials, admittance throughout this instance reduces as the grain size reduces. As varied bias voltage between 0 V and 2 V is supplied, the admittance does not change considerably.

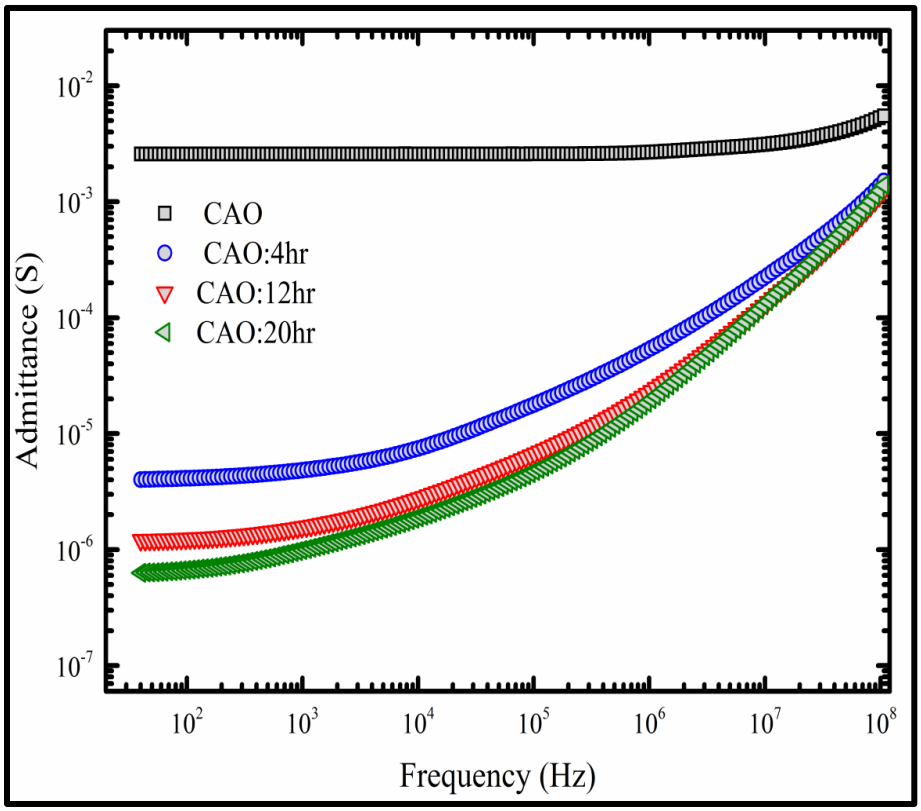

Figure 7.6: Frequency dependence admittance plot for *MICRO* and size variant (4 − 20 h) nanocrystalline $CuAlO_2$ at 2 V external biased.

The following expression $\varepsilon' = Cd / \varepsilon_o A$ was employed to calculate the dielectric constant (ε') throughout the range of frequencies from 40 Hz to 110 MHz with 2 V external bias at room temperature. Here C is the pellet's capacitance, d is its thickness, A is its cross-section area, and ε_o is the free spaces permittivity for all synthesized materials. Figures 7.7(a&b) demonstrate the frequency dependence dielectric constant (ε') and also dielectric loss tangent tan δ across 2 V external bias for *MICRO* and nanocrystalline $CuAlO_2$ (4−20 h). Due to the fact that both ε' or tan δ with in observed operating frequency range diminish as frequency rises, while 2 V constant bias voltage, which exhibiting the semiconducting nature of polycrystalline delafossite $CuAlO_2$.

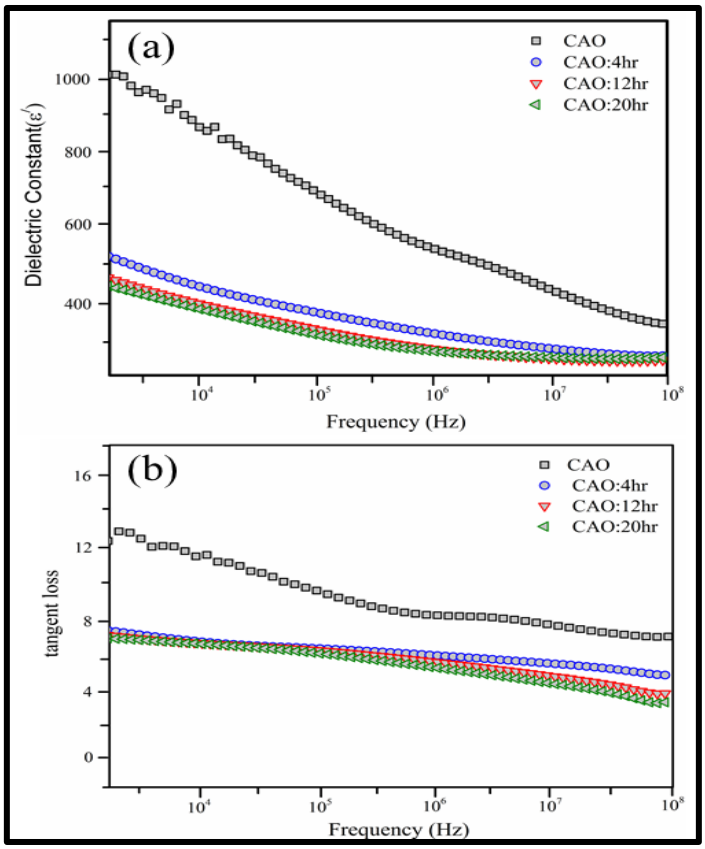

Figure 7.7: (a) Frequency dependence dielectric constant (ε') and (b) dielectric loss plot for *MICRO* and size variant (4−20 h) nanocrystalline $CuAlO_2$ at 2 V external biased.

Furthermore, at lower frequency region, where there are considerably high values of ε' or tan δ, the impact of grains interfaces becomes much more apparent. This gives insight into the actions of localised charge carriers, thereby improving overall explanation of dielectric polarisation process. The current observed pattern clearly demonstrates that, whereas dipolar and also interfacial polarisations have become the major sources of polarisation for low frequency range, ionic and also electronic polarisations are major contributors for high frequency range. The grain boundary density in nanocrystalline materials is larger than the *MICRO* $CuAlO_2$. The overall ε' or tan δ of the nanocrystalline samples is reduced because the growing amount of defect states serving as recombination centres.

Typically the real part of ac conductivity σ′ (ω), which is measured using the formula $\sigma(\omega) = \sigma'(\omega) - i\sigma''(\omega)$, typically exhibits significant frequency dispersion. The profile (4-20 h) for nanocrystalline $CuAlO_2$ could include a lower frequencies region that represents the materials are dc conductivity nature but dispersive region in such a higher frequency that represent the materials are ac conductivity nature. The frequency dependence ac conductivity for *MICRO* (inset) and nanocrystalline $CuAlO_2$ at 2 V external biased, presenting in Figure 7.8. It is obvious that whereas ac conductivity predominates at higher frequency region, the conductivity of real part is frequency independent at lower frequency region, resulting in dc conductivity. Indicating the ionic motion rather than arbitrary mobile ions hopping is taking place, the presence of this kind of dispersive region with in conductivity at high frequency limits of such possibilities [50]. The fact that nanocrystalline $CuAlO_2$ samples exhibit high ac conductivities at higher frequencies for 2 V external biases clearly indicates that now the trapped bound carriers inside the materials, which cause small polaron hopping (SPH) between these trapped centres, are responsible for such ac

conductivities which are recognized. Consequently, in contrast to the *MICRO* $CuAlO_2$, the conductivity reduces consistently at lower frequency while particle size reduces.

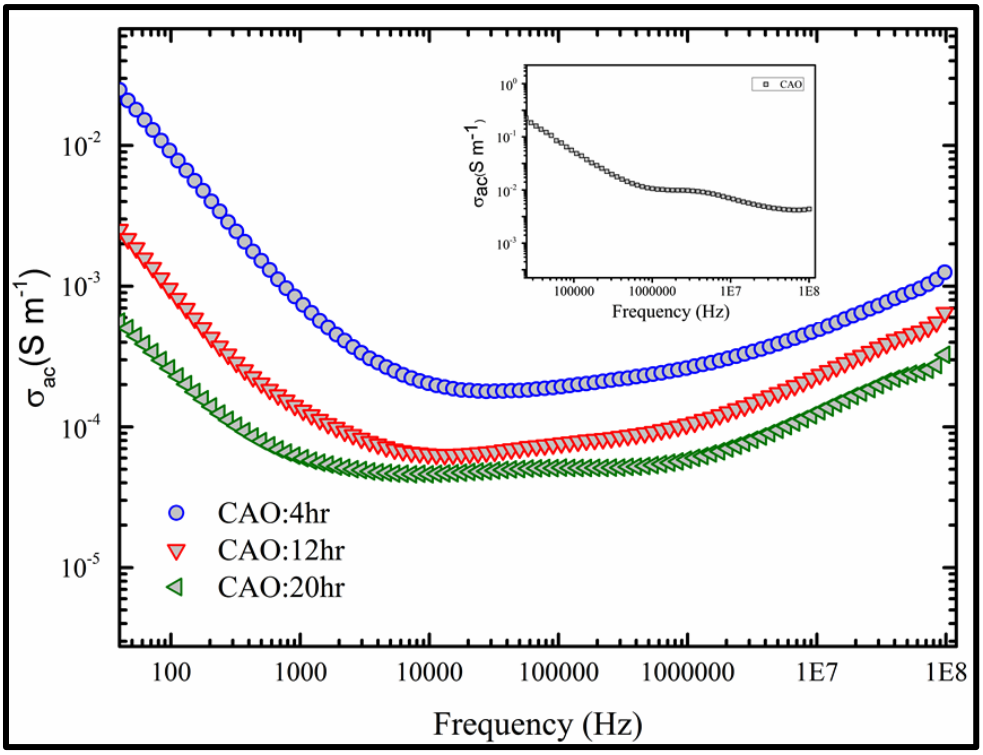

Figure 7.8: Frequency dependence ac conductivity plot for *MICRO* and size variant (4− 20 h) nanocrystalline $CuAlO_2$ at 2 V external biased.

7.4. Conclusions:

By using mechanical ball-milling top down approach, we are able to successfully produce *p*-TCOs delafossite $CuAlO_2$ powder that is nanoscale in size. The development of *MICRO* and nanocrystalline $CuAlO_2$ (4−20 h) with a grain size of about 20 nm is demonstrated by the structural,

microstructural, optical and transport characterization without any secondary phase generation only delafossite phases with rhombohedral symmetry. It is clear from evaluating the DR spectra that all the doped materials get a wider band gaps in the so-called transparent optical range. The optical gaps are found around 3.77 to 3.79 eV at (4−20 h) with compared to *MICRO* sample (3.75 eV). The holes become thermally activated around 150 K, and also the VRH method is dominant around 80 to 145 K, according to the temperature dependent electrical conductivity profile (80 - 300 K). The *MICRO*- $CuAlO_2$ (0.41 S-cm^{-1}) seems to have a conductivity that is five times larger than its *NANO* (0.076 S-cm^{-1}) counterpart at room temperature. Due to the fact that ε' and tan δ with in measurement frequency range reduces as frequency rises with constant bias voltage, which exhibiting the semiconducting nature of polycrystalline delafossite $CuAlO_2$. Consequently, in contrast to the *MICRO* $CuAlO_2$, the conductivity reduces consistently at lower frequency while particle size reduces. The cause could be due to an increase mostly in grain density boundaries, which contribute as a centre of holes trapping/recombination. That's because the grain size has a significant impact on electrical conductivity, thermoelectric applications advantage from its characteristics.

7.5. References:

1. B.G. Lewis, D.C. Paine, MRS Bull. (2000) 22.

2. Y. Yang, L. Wang, H. Yan, S. Jin, T.J. Marks, S.Y. Li, Appl. Phys. Lett. 89 (2006) 051116.

3. M. Emziane, K. Durose, D.P. Halliday, A. Bosio, N. Romeo, Appl. Phys. Lett. 87 (2005) 251913.

4. D. Ginley, T. Coutts, J. Perkins, D. Young, X. Li, P. Parilla, MRS Proc. (2001) 668.

5. C.G. Granqvist, A. Hultaker, Thin Solid Films 411 (2002) 1.

6. K.L. Chopra, S. Major, D.K. Pandya, Thin Solid Films 102 (1983) 1.

7. T.V. Thu, S. Maenosono, J. Appl. Phys. 107 (2010) 014308.

8. F.A. Benko, F.P. Koffyberg, J. Phys. Chem. Solids 45 (1984) 57.

9. H. Kawazoe, M. Yasukawa, H. Hyodo, M. Kurita, H. Yanagi, H. Hosono, Nature 389 (1997) 939.

10. R. Laskowski, N.E. Christensen, P. Blaha, B. Palanivel, Phys. Rev. B 79 (2009) 165209.

11. I.Y.Y. Bu, Superlattices Microstruct. 60 (2013) 160.

12. T. Dittrich, L. Dloczik, T. Guminskaya, M.C. Lux-Steiner, N. Grigorieva, I. Urban, Appl. Phys. Lett. 85 (2004) 742.

13. B. Mahrov, G. Boschloo, A. Hagfeldt, L. Dloczik, T. Dittrich, Appl. Phys. Lett. 84 (2004) 5455.

14. X.G. Zheng, K. Taniguchi, A. Takahashi, Y. Liu, C.N. Xu, Appl. Phys. Lett. 85 (2004) 1728.

15. A.N. Banerjee, R. Maity, P.K. Ghosh, K.K. Chattopadhyay, Thin Solid Films 474 (2005) 261.

16. H. Gong, Y. Wang, Y. Luo, Appl. Phys. Lett. 76 (2000) 3959.

17. K. Tonooka, K. Shimokawa, O. Nishimura, Thin Solid Films 411 (2002) 129.

18. C. Bouzidi, H. Bouzouita, A. Timoumi, B. Rezig, Mater. Sci. Eng. B 118 (2005) 259.

19. G.B. Dong, M. Zhang, X.P. Zhao, Y.C. Li, H. Yan, J. Cryst. Growth 311 (2009) 1256.

20. W. Lan, G.B. Dong, M. Zhang, B. Wang, H. Yan, Y.Y. Wang, Rare Metal. Mater. Eng. 36 (2007) 921.

21. A.H. Zhong, J. Tan, H.L. Huang, S.C. Chen, M. Wang, S. Xu, Appl. Surf. Sci. 257 (2011) 4051.

22. N. Koriche, A. Bouguelia, A. Aider, M. Trari, Int. J. Hydro. Ener. 30 (2005) 693– 699.

23. V. H. Hahn, C. D. Loreht, Zeitschrift fur anorganische und allgemeine Chemie, 279 (1955) 281–288.

24. F.A. Benko, F. P. Koff- Yberg, J. Phys. Chem. Solids 45 (1984) 57–59.

25. R. D. Shannon, D. B. Roregrs, C. T. Prewitt, Inorg. Chem., 10 (1971) 713–718.

26. D. Xiong, X. Zeng,W. Zhang, H. Wang, X. Zhao, W. Chen, Yi-B. Cheby, Inorg. Chem.

53 (2014) 4106−4116.

27. E.J. Gonzales, K.V. Trumble, J. Amer. Ceram. Soc. 79 (1996) 114–120.

28. B. Saha, R. Thapa, K.K. Chattopadhyay, Mater. Lett. 63 (2009) 394–396.

29. A.M.M. Gadala, J. White J. Trans. Brit. Ceram. Soc. 63 (1964) 39–62.

30. P.G. McCormick, T. Tsuzuki, J.S. Robinson, J. Ding, Adv. Mater. 13 (2001) 1008-1010.

31. E. Avvakumov, M. Senna, N. Kosova, Kluwer Academic Publischers: Dordrecht, 2001; 1-207.

32. T. Rojac and M. Kosec, M. Sopicka-Lizer, Woodhead Publishing, Boston, 2010, pp.

113–148.

33. V. Šepelák, A. Düvel, M. Wilkening, K-D. Becker, P Heitjans, Chem. Soc. Rev. 42 (2013) 7507–7520.

34. D. Y. Shahriari, A. Barmane, T.O. Mason, K. R. Poeppelmeier, Inorg. Chem. 40 (2001) 5734–5735

35. K. Vojisavljević, B. Malič, M. Senna, S. Drnovšek, M. Kose, J. Eur. Ceram. Soc. 33 (2013) 3231–3241.

36. N. Mazumder, D. Sen, U.K. Ghorai, R. Roy, S. Saha, N.S. Das, K.K. Chattopadhyay, J. Phys. Chem. Lett. 4 (2013) 3539 – 3543.

37. P. Mandal, N. Mazumder, S. Saha, U.K. Ghorai, R. Roy, G.C. Das, K. K.Chattopadhyay, J. Phys. D Appl. Phys. 49 (2016), 275109.

38. P. Mandal, N. Mazumder, S. Saha, U.K. Ghorai, R. Roy, G.C. Das, K. K.Chattopadhyay, Current Applied Physics 25 (2021) 90–96.

39. A. Das, S. Saha, K. Panigrahi, A. Mitra, R. Chatterjee, U. K. Ghorai, B. Das, and K. K. Chattopadhyay, Cryst Eng Comm., 2018, 20, 2540- 2552.

40. Steven Mudenda, Girish M. Kale and Yotamu R. S. Hara, J. Mater. Chem. C,2014, 2,9233.

41. H. Alhummiany, Journal of Nanomaterials, 2018,4076960.

42. M. S. Lee, T. Y. Kim and D. Kim, Appl. Phys. Lett., 2001, 79,2028–2030.

43. F. A. Benko and F. P. Koffyberg, J. Phys. Chem. Solids, 1984,45,57–59.

44. A.E. Morales, E.S. Mora, U. Pal, Rev. Mex. Fis. 53 (2007) 18-22.

45. B.Das, A. Renaud, A.M. Volosin, L.Yu, N. Newman, D. Seo, Inorg. Chem., 2015, 54 (3), pp 1100–1108.

46. N. F. Mott and E. A. Davis, Clarendon Press, Oxford, 1971.

47. O. J. Dur´a, R. Boada, A. Rivera-Calzada, C. Le´on, E. Bauer, M. A. L´opez de la Torre, and J. Chaboy, Physical Review B 83, 045202 2011.

48. D. Li, X. Fang, Z. Deng, W. Dong, R. Tao, S. Zhou, J. Wang, T. Wang, Y. Zhao, X. Zhu, J. Alloy Compd. 486 (2009) 462-467.

49. R. Kumar, N. Khare, Thin Solid Films 516 (2008) 1302-1307.

50. Steven Mudenda, Girish M. Kale and Yotamu R. S. Hara, J. Mater. Chem. C,2014, 2,9233.

8. Grand conclusions and future scope

Chapter 8

8.1. Summary of thesis:

All of the major conclusions from the works contained in this thesis are presented throughout this chapter. The production of *p*-TCOs is required for the manufacturing include all junctions in *p*-*n* systems which are transparent. The optimum conductivity of *p*-TCOs documented up to this point is still several numbers of magnitude lower than *n*-TCOs that are widely accessible. Therefore, this hinders growth of efficient devices in significant volume production. Nowadays, *p*-TCOs are being presented the supreme trade-off in between electrical as well as optical analysis. Co-doping of *p*-TCOs is thus a crucial research field for such creation of photonics and spintronics technologies of greater quality. The *p*-TCOs have the potential to create a broad range of novel devices, despite the verity that their conductivity remains lesser compared to *n*-type counterparts.

This thesis is well-documented chapters that are focused on the research ideas with applications. Chapter 1 starts with a general introduction of TCOs and includes the historical content with their detailed discussion of practical implications in contemporary life. Chapter 2 represents review of correlated literature on copper based delafossite also their classifications are considered along with some ground-breaking reports. The detailed documentation of the experimental characterization utilized in the thesis is provided in chapter 3. By doping cationic and anionic simultaneously are performed in prototype *p*-$CuCrO_2$ to maintain the transparency while improving electrical conductivity explains in chapter 4. Mg and S are applied as dopant elements at Cr and O-sites respectively with varying concentrations and it's confirmed by Rietveld analysis. It is obvious that

all doped materials are in transparent region. In the range of 80 to 300 K, DC conductivity clearly shows around 140 K lowers, where transport is dominated by VRH or above by thermal activation approach. In electrical measurements twice time enhance conductivity for co-doped materials (0.045 S-cm^{-1}) than Mg-doped $CuCrO_2$ (0.022 S-cm^{-1}) with higher hole mobility (61.66 cm^{2}V^{-1}s^{-1}). With considering co-doped materials to certain other doped materials, there is indication of a steady rise in metallicity.

Chapter 5 introduce Li ion doping at Cr site and S ion doping at O site in the host *p*-$CuCrO_2$ to validate the resulting band dispersion experimentally over the contribution from shallow *S 3p* acceptors with maintaining transparency. To investigate how site dependent hole inducing affects the corresponding changes in physical and transport properties. By using Rietveld method, the sites substitutional occupancy of $Li_{Cr}^{\bullet\bullet}$ and also $S_O^{\times}$ is verified and measured. The confirmation of a significant energy gap (about 3.5 eV) is assessed following co-doping *p*-TCOs with in the transparent optical range. Four fold increasing in electrical conductivity (0.020 S/cm) upon the cationic-anionic doping $CCO/(Li_{Cr}^{\bullet\bullet} + S_O^{\times})$ in comprise with $CCO/Li_{Cr}^{\bullet\bullet}$. These findings show promising prospects for transparent semiconducting device application in comparably developed *P*-TCOs.

Chapter 6 carries out and is compared to temperature dependence hole conductivity and identified for Li and S doping more likely way to cross the bottleneck threshold than Mg and S doping in *P*-$CuCrO_2$ and also enhance metallicity. Temperature-dependent hole conductivity, which preserves optically transparent as well, provides evidence for delocalization in lighter holes.

Chapter 7 investigated to the effect of reducing grain size impact of the transport and structural analysis of *p*-$CuAlO_2$ and is acquired via ball milling process with good transparency. To obtain size-variant nanocrystalline *p*-$CuAlO_2$, micro - structured $CuAlO_2$ be treated in such a planetary mill during 4, 12, and 20 hours, respectively. As when the energy gap widens with decreasing grain size, optical properties for nanocrystalline $CuAlO_2$ enhance. Electrical analysis of micro and nano samples reveals that the hole conductivity for the nanocrystalline materials reduces by several orders due to increased grain boundary density serves as the center for trapping or recombination of charged carriers. With an improving electrical conductivity profiles for such nanocrystalline materials, the dielectric constant and tangent loss factor across the whole frequency spectrum are both reduced considerably. That's because the grain size have a significant impact on electrical conductivity, thermoelectric applications advantage from its characteristics.

8.2. Future scope:

There are many potential to enhance the properties of the *p*-TCOs materials because a significant amount of work has been placed into the production of this materials. Throughout the section that follows, the potential for *p*-TCOs materials is further explained.

- Comparing co-doped materials to undoped *p*-$CuCrO_2$, the electrical and also optical characteristics have greatly improved. The electrical conductivity increase in several orders of magnitude upon co-doping with decrease carrier mobility. The reduction of hole mobility could be attributed to defects caused upon with polycrystallinity, which is

expected that the thin film production material could resolved this arising issue.

- The carrier density in *p*-$CuCrO_2$ must also be optimized for application in the developing field of transparent devices. Such factors are also crucial for controlling conductivity in oxide nanostructured thin-film, which is estimated to become more and more prominent in prospective transparent electronic applications.
- Another very promising area of research can generate significant junction devices seems to be the fabrication of thin films delafossite $CuCrO_2$ with both forms of conductivity. Due to the more recent approaches to material synthesis, thin film technology is rapidly progressing.
- The thermoelectric capabilities of $CuCrO_2$ films are also another field of study that has still not been fully investigated but contains a significant amount of potential.
- The electronic characteristics with DFT analysis of co-doped $CuCrO_2$ have not yet been fully investigated, which an uphill task that is now in progress.
- A totally different study area with a huge amount of potential is the field emission feature of co-doped $CuCrO_2$. Investigating the emission process is required to improve the field emission features because the optimal emission strategy in such compounds is not yet entirely clear.

PhD Thesis

ORIGINALITY REPORT

0%
SIMILARITY INDEX

PRIMARY SOURCES

1	A. J. DYSON, P. V. SMITH. "Improved empirical interatomic potential for C-Si-H systems", Molecular Physics, 5/20/1999 Crossref	9 words — < 1%

EXCLUDE QUOTES	OFF	EXCLUDE SOURCES	OFF
EXCLUDE BIBLIOGRAPHY	OFF	EXCLUDE MATCHES	OFF

Prasanta Mandal
10/01/2023

Exclusion list for plagiarism check:

1. http://dx.doi.org/10.1088/0022-3727/49/27/275109 (Chapter 4)
2. https://doi.org/10.1016/j.cap.2021.01.001 (Chapter 5)
3. http://dx.doi.org/10.1063/1.4980678 (Chapter 6)
4. All the references
5. All equations
6. All Certificates, list of table, list of figure, Acknowledgement, list of publication

Terminology:

Transparent conductive oxides (TCOs)

Cu based delafossite oxides

Cationic-anionic doping

Linearly coordinated cations

Edge-shared BO_6

Optical band gap or energy gap

Trivalent ions (B^{+3})

Electrical conductivity/properties

As well as

$ZnRh_2O_4$, $ZnIr_2O_4$

Carrier mobility/density/concentration

Antibonding state

Cu Kα (λ=1.54Å), 40 mA and 40 kV

Ch p and *Cu 3d*

Allowed transition

Valence orbit

P63/mmc space group

Cu-3d VB edge

Magnetron sputtering

O 2p levels

High vapours pressure

Optical, electrical, structural and microstructural

Absorbs, reflects

Transparency/transmittance

Lattice defects

Polycrystalline

Structural properties

Temperatures, range

Grain size

Oxygen octahedral

Optical transparency

Chemical modulation of the valence band (CMVB)

DS-solar cells (DSSC)

Solid-state electrolytes (SSEs)

Planetary ball- milling (Fristch pulverisette 7)

X-ray diffraction (XRD)

XRD (Bruker D8 Advance)

UV-visible spectroscopy (Shimadzu UV-Vis 3600)

X-ray photoelectron spectroscopy (XPS)

Field Emission Scanning Electron Microscope (FESEM)

SPECS HSA-3500 hemispherical analyser

FESEM S-4800, Hitachi

Visible light

Energy dispersive x-ray (EDX)

Pulsed laser deposition (PLD)

Transmission electron microscope (TEM: JEOL, JEM-2100)

Selected area electron diffraction (SAED)

HIOKI (3522 – 50) LCR Hi-TESTER

Van- der- Pauw

S cm^{-1}

Agilent (4294A) precision impedance analyzer

Kinetic energy (K.E)

Thin film

Opto-electronics devices

Delafossite Oxides

Characteristics films

FTO, ITO, AZO

LEDs

Solar cells

Wavelength X-ray, diffraction peak, Rietveld analysis

Experimental and growth

Molecular beam epistaxy (MBE)

Department of Science and Technology (DST)

School of Materials Science and Nanotechnology

University Grants Commission (UGC)

Jadavpur University

Kolkata –700032

Prasanta Mandal

Gopes Chandra Das 10/01/2023

(Prof. Gopes Chandra Das)

Professor
Metallurgical & Material Engg. Dept.
Jadavpur University
Kolkata - 700032

10.1.23

(Prof. Kalyan Kumar Chattopadhyay)

Dr. K. K. Chattopadhyay
Professor
Head, Department of Physics
Jadavpur University
Kolkata-700 032

Exclusion list for plagiarism check:

1. http://dx.doi.org/10.1088/0022-3727/49/27/275109 (Chapter 4)
2. https://doi.org/10.1016/j.cap.2021.01.001 (Chapter 5)
3. http://dx.doi.org/10.1063/1.4980678 (Chapter 6)
4. All the references
5. All equations
6. All Certificates, list of table, list of figure, Acknowledgement, list of publication

Terminology:

Transparent conductive oxides (TCOs)

Cu based delafossite oxides

Cationic-anionic doping

Linearly coordinated cations

Edge-shared BO_6

Optical band gap or energy gap

Trivalent ions (B^{+3})

Electrical conductivity/properties

As well as

$ZnRh_2O_4$, $ZnIr_2O_4$

Carrier mobility/density/concentration

Antibonding state

Cu Kα (λ=1.54Å), 40 mA and 40 kV

Ch p and *Cu 3d*

Allowed transition

Valence orbit

P63/mmc space group

Cu-3d VB edge

Magnetron sputtering

O 2p levels

High vapours pressure

Optical, electrical, structural and microstructural

Absorbs, reflects

Transparency/transmittance

Lattice defects

Polycrystalline

Structural properties

Temperatures, range

Grain size

Oxygen octahedral

Optical transparency

Chemical modulation of the valence band (CMVB)

DS-solar cells (DSSC)

Solid-state electrolytes (SSEs)

Planetary ball- milling (Fristch pulverisette 7)

X-ray diffraction (XRD)

XRD (Bruker D8 Advance)

UV-visible spectroscopy (Shimadzu UV-Vis 3600)

X-ray photoelectron spectroscopy (XPS)

Field Emission Scanning Electron Microscope (FESEM)

SPECS HSA-3500 hemispherical analyser

FESEM S-4800, Hitachi

Visible light

Energy dispersive x-ray (EDX)

Pulsed laser deposition (PLD)

Transmission electron microscope (TEM: JEOL, JEM-2100)

Selected area electron diffraction (SAED)

HIOKI (3522 – 50) LCR Hi-TESTER

Van- der- Pauw

S cm^{-1}

Agilent (4294A) precision impedance analyzer

Kinetic energy (K.E)

Thin film

Opto-electronics devices

Delafossite Oxides

Characteristics films

FTO, ITO, AZO

LEDs

Solar cells

Wavelength X-ray, diffraction peak, Rietveld analysis

Experimental and growth

Molecular beam epistaxy (MBE)

Department of Science and Technology (DST)

School of Materials Science and Nanotechnology

University Grants Commission (UGC)

Jadavpur University

Kolkata –700032

Prasanta Mandal

Gopes Chandra Das 10/01/2023

(Prof. Gopes Chandra Das)

Professor
Metallurgical & Material Engg. Dept.
Jadavpur University
Kolkata - 700032

10.1.23

(Prof. Kalyan Kumar Chattopadhyay)

Dr. K. K. Chattopadhyay
Professor
Head, Department of Physics
Jadavpur University
Kolkata-700 032